Electrohydrodynamic and Thermocapillary Effects on Thin-Film Flows

A THESIS
SUBMITTED TO THE FACULTY OF THE GRADUATE SCHOOL
OF THE UNIVERSITY OF MINNESOTA
BY

Andrew Joseph Corbett

IN PARTIAL FULFILLMENT OF THE REQUIREMENTS
FOR THE DEGREE OF
DOCTOR OF PHILOSOPHY IN MATERIALS SCIENCE AND ENGINEERING

Satish Kumar

January 2016

Acknowledgements

There are many people that have earned my gratitude for their contributions to my time in graduate school. I would first like to thank my adviser, Professor Satish Kumar, for his guidance and instruction throughout my career as a graduate student. Professor Kumar took a chance on me when he accepted into his group a student with a B.A. in chemistry and no formal coursework in engineering or applied mathematics. However, he assured me that the most important quality in a researcher was the desire to learn. I am extremely grateful that he saw potential in me and helped shape me into the engineer that I am today.

I was also fortunate to work with exceptional colleagues in my research group. Dr. Shawn Dodds, Dr. Eric Vandre, Dr. Aruna Ramkrishnan, Dr. Sarit Dutta, Dr. Changkwon Chung, Dr. Akhilesh Sahu, Dr. Jeongyong Lee, Dr. Bo Kyung Ryu, Dr. Si Hyung Lee, Dr. Leonardo Espín, Weihua Li, Chen-Yu Liu, Chung-Hsuan Huang, and Truong Pham have at different times been much-appreciated sources of insight as well as enjoyable distraction. I am particularly indebted to Leo for his patience with me as our conversations frequently drifted off-topic when he endeavored to teach me various numerical techniques.

My family and friends have also played an essential role during my journey toward and throughout graduate school. I wouldn't be where I am today without my mother, Cindy Leonard, fostering my interest in science as a child by buying me dinosaur books and bringing me to the Science Museum. I couldn't be an engineer without my father, Ken Corbett, having taught me how to get the most out of myself both on the baseball field and in my work. I need to thank my siblings, Bryan and Natalie, for tolerating me as the youngest child. I also owe Cheryl, David, and Ryan Moertel a debt of gratitude for taking me into their family and offering great support during my time in Rochester.

Finally I must thank my wife, Dr. Jessica Moertel, most of all. Without her motivating me in college, I never would have pursued graduate school in the first place. Despite her own demanding years of medical school and residency, Jessica was always there to encourage me when I needed it and celebrate with me when the occasion called for it. My time in graduate school was infinitely better because of Jessica, and I am very excited for our times ahead.

Abstract

Controlling thin liquid film flows is a problem that has implications for technologies such as microelectronics and microfluidics. As these types of devices continue to become both smaller and more complex, our ability to manipulate liquids at small length scales will become increasingly critical. In this thesis we study several problems which advance our understanding of how electric and temperature fields can be harnessed to manipulate thin liquid film flows. First, we study how the combined application of normal electric and temperature fields can be used for the patterning of thin polymeric liquid films using a linear stability analysis and nonlinear simulations. For perfect dielectric liquids we find that thermocapillary forces arising from the temperature gradient dominate the patterning process, rendering the electrohydrodynamic forces nearly negligible. For leaky dielectric liquids, charge which accumulates at the liquid-air interface generates shear stresses which contribute significantly to the patterning process by reducing feature size and patterning time. Inclusion of viscoelasticity in our model shows that rheology affects the rate of patterning but not the length scale of the pattern. Second, we use nonlinear simulations to examine electrohydrodynamic and thermocapillary effects on gravity-driven droplet spreading. We find that in perfect dielectric liquids, the electric field modifies the liquid-air interface but will not alter the long-time spreading rate. However in leaky dielectric liquids, the buildup of surface charge can greatly alter the long-time spreading dynamics by causing separation of the droplet into a series of smaller droplets. In both cases, thermocapillary forces imposed by cooling the film from below can negate the effects of the electric field. We also find that partially wetting liquids are more susceptible to droplet separation in both perfect and leaky dielectric liquids. Finally, we conduct a linear stability analysis to study electrohydrodynamic and thermocapillary effects on the gravity-driven spreading of thin liquid films. We find that both electric and temperature fields can be used to stabilize the advancing contact line of the liquid film to transverse perturbations. We perform an energy analysis and find complex interactions between the traveling wave solution and the perturbations which shed light on the mechanism behind this stabilization.

Contents

List of Tables

List of Figures

Chapter 1

Introduction

Thin solid and liquid films play important roles in countless aspects of our everyday lives. The ability of a vehicle's windshield to repel water, the response of the screen of a cellular phone to a finger, or the stain-resistant qualities of clothing all depend heavily on thin films to be functional and/or fashionable. Just as the quality of a product may depend on a thin film for its functionality, the quality of the thin film itself often depends on the dynamics of a patterning or liquid coating process. Ensuring that a single device or product is coated in a satisfactory way could be as simple as immersing the item in a liquid and visually inspecting the piece after the coating has dried. However, visually inspecting every item that undergoes a coating process would obviously be inefficient and cost-prohibitive for products that have large production runs. Instead, it is preferable to design versatile coating processes that are repeatable over long times, reliable in the quality of coatings they generate, and insensitive to disturbances that occasionally occur on a production floor.

As the complexity of devices tends to increase and the size of devices tends to decrease, we will require more versatile patterning and coating processes which allow engineers to exert greater control over liquid films. This can be accomplished in part by choosing from a number of available coating geometries (e.g. spray coating, curtain coating, spin coating, etc.), but it is possible that more precise control over the liquid may be required for certain applications. Two tools that we can use to manipulate thin films are electric fields and temperature fields. Electric and temperature fields interact with liquids in very different ways, yet they can be simultaneously imposed in a liquid

film and both forces affect the dynamics of liquid flow. It is the goal of this thesis to examine how electric and temperature fields may influence thin film flows which are relevant to surface patterning and liquid coating processes.

In this thesis, I study two problems which are related to how electric and temperature fields can influence thin film flows. The first problem investigated involves how electric fields and temperature gradients can destabilize the surface of thin polymer films in order to generate patterns for new surface topographies. In Chapter 2, I examine how electric and temperature fields can be used simultaneously in order to pattern a variety of liquids, including both perfect dielectric and leaky dielectric liquids and both Newtonian and non-Newtonian liquids. The second problem that is investigated is how electric and temperature fields affect gravity-driven drainage flows which contain contact lines. In Chapter 3, I study how the interface of a two-dimensional liquid droplet undergoing gravity-driven spreading responds to imposed electric and temperature fields. Both perfect dielectric and leaky dielectric liquids are considered, as well as both perfectly and partially wetting liquids. In Chapter 4, I study the effects of electric and temperature fields on the stability of the contact line to transverse perturbations in gravity-driven thin film flows. Conclusions, suggestions for future work, and some final remarks are given in Chapter 5.

1.1 Patterning processes

Surface topography can have drastic effects on how a material interacts with its surroundings. Topography influences how a material reflects light, its electrical conductivity, and the ability of cells to grow on a surface [4]. Due to its importance in how materials interact with each other, control over surface topography (or surface patterning) can be a powerful means of modifying the functionality of a material or object. In some cases, it will not be feasible to directly modify the surface of a bulk material. Instead, it may be more convenient to deposit a thin liquid film on the bulk material, and pattern the surface of the liquid film. Electric and temperature fields offer two tools which may be used to induce pattern formation by destabilizing the surface of such a liquid film.

There are a variety of methods for surface patterning of thin films. Photolithography remains popular for its relative simplicity and versatility. In photolithography, a thin

film is uniformly coated with photoresist, then is patterned by passing ultraviolet light through a pre-fabricated mask, followed by chemical etching of the thin film and then removal of the remaining photoresist. The achievable feature size using photolithography is theoretically limited by the wavelength of light that is used to react the photoresist (typically on the order of 100 nanometers), although recent developments in excimer laser lithography have patterned at length scales on the order of 10 nm [5]. An additional step and potential challenge in photolithography is the design and fabrication of the patterned mask, not to mention the use of hazardous chemicals in the etching process. As new applications in microelectronics and microfluidics increasingly demand smaller feature size, it is of interest to pursue methods of surface patterning which do not suffer from the limitations and challenges of photolithography. Resistless techniques which do not require ultraviolet light, pre-patterned masks, and photoresists could be of great utility.

A different avenue for patterning surfaces is to deposit a liquid film on a surface, create a pattern by inducing a liquid flow (often rendering a pre-patterned mask unnecessary), then locking in the new features by solidifying or drying the liquid film. Two such methods are electrohydrodynamic (EHD) patterning and thermocapillary (TC) patterning. These both have the advantages of involving relatively few steps (i.e. deposit liquid film, pattern liquid film, solidify liquid film), often not requiring harsh chemicals, and not requiring the fabrication of a pre-patterned mask.

In electrohydrodynamic patterning, a polymer solution (or a polymer heated above its glass transition temperature) is first spin-coated onto a solid substrate, often with an initial indium-tin-oxide coating present on top. A conductive mask is suspended a small distance above the surface of the coating and an electric field is applied perpendicular to the film surface. The electric field destabilizes the initially flat surface causing a hexagonal array of pillars to form, an example of which is shown in Figure 1.1(a). The new topography is locked in by either drying the polymer solution or cooling the polymer below its glass transition temperature, both resulting in a solid polymer film with a surface of hexagonally arranged micropillars. This process has proven effective for generating wavelengths of pillars to be on the order of microns [1, 6] with theoretical analysis suggesting submicron patterns are possible [7]. The rate of EHD patterning as well as the wavelengths observed can be further tuned by use of an AC field [8, 9] or

(a) 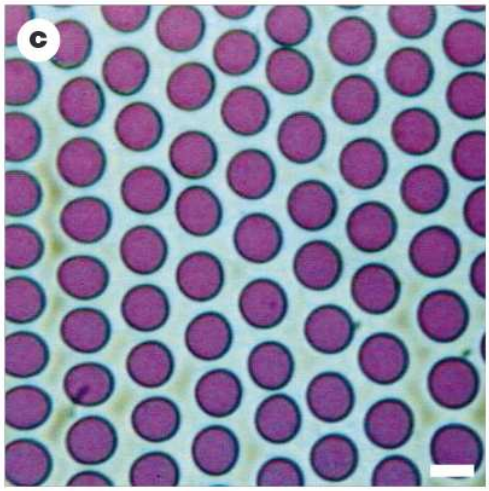

(b) 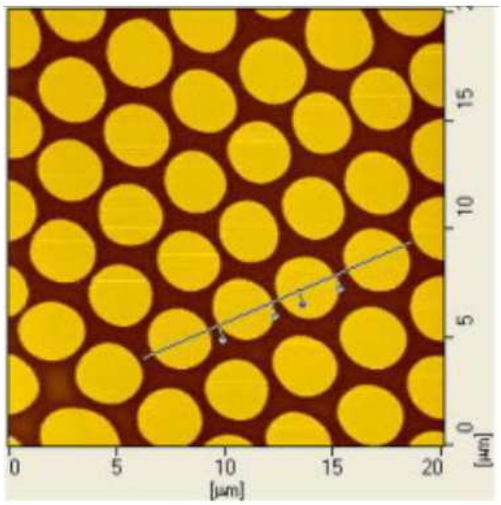

Figure 1.1: (a) An example of a polystyrene film that has been patterned using electrohydrodynamic (EHD) patterning. Scale bar corresponds to 5 μm. Image taken from Schäffer et al. (2000) [1]. (b) An example of a poly(methyl methacrylate) film that has been patterned using thermocapillary (TC) patterning. Image taken from Peng et al. (2004) [2].

changing the polymer rheology [10, 11].

In thermocapillary patterning, a polymer solution is spin-coated onto a substrate, typically a silicon wafer. The coated wafer is then placed onto a temperature-controlled hotplate while a second silicon wafer is mounted at a fixed distance above the surface of the coated film, this wafer in contact with a second hotplate. The temperature of each hotplate is brought above the glass transition temperature of the polymer, with the top hotplate being 10-30 ^{o}C cooler than the bottom. The temperature difference between the two plates creates a temperature gradient in the surface of the film which destabilizes it to mechanical disturbances [12]. As in EHD patterning, the polymer surface self-arranges into a hexagonal array of pillars, an example of which is shown in Figure 1.1(b). Again, the new topography can be locked in by cooling the polymer below its glass transition temperature. Wavelengths of the pillar arrays in TC patterning experiments have been on the order of 1-10 μm [2, 13].

As is evident, the experimental setups and patterns generated by EHD and TC patterning are quite similar. Both methods require a thin polymer film to be deposited onto

a substrate, above which an unpatterned mask is suspended. Both methods destabilize the surface of the polymer film to disturbances which grow into hexagonally arranged micropillars. The smallest achievable wavelength from each of these methods is limited by the magnitude of the field which is applied, this being the potential difference in EHD patterning and the temperature gradient in TC patterning. Because of the similarities in experimental setups and patterns that are generated, it may be possible to generate smaller pillar-to-pillar distances by simultaneously applying both an electric and temperature field. In Chapter 2, I use linear stability analysis to study the effects of combined EHD and TC patterning.

1.2 Gravity-driven drainage flows

It can often be desirable to use a uniformly-thin coating to modify surface properties of a material. The benefits of applying a coating could be to improve durability, to modify electrical properties, or to apply a smooth finish to an otherwise coarse surface. In these cases, the objective of the coating process is not to create complex topography on the surface, as is the case in patterning, but to leave a finished smooth and uniform coating on the material's surface. An excellent way of achieving a smooth coating is by applying the material using a liquid solution and then solidifying by either drying or curing the liquid.

There are a variety of coating processes for depositing a liquid onto a solid substrate, such as spray coating, dip coating, spin coating, among many others. If the initial deposition of the liquid is not perfectly uniform, regions of the film which are thicker than the surrounding liquid area can form. If a thicker region of liquid is resting on a surface that is inclined, then gravity-driven drainage flows will occur. Often as the driven film flows down the substrate, the thicker region will naturally spread under the forces of gravity and surface tension, and generate the desired uniform film. Goodwin and Homsy (1991) [14] and Moriarty et al. (1991) [15] found quasi-steady solutions for the spreading of two-dimensional gravity-driven films indicating that a thin uniform film would be obtained in the absence of perturbations. Schwartz et al. (2005) [16] studied the spreading of three-dimensional drops down a vertical wall and found that partially-wetting liquids can separate into a series of droplets, in agreement with prior

experiments [17].

The gravity-driven spreading of droplets in the absence of other external forces has been studied extensively. However, external forces such as electric fields or temperature gradients may be present under certain circumstances, such as if the liquid is electrically conductive, undergoing electrospray deposition, or undergoing heat-assisted drying. If such forces are present, nonuniformities in film height could respond in unintended ways. Instead of smoothly spreading into a uniform film as studies in the absence of external forces show, an electric or temperature field could enhance the nonuniformities and lead to defects in the final coating. Although thin film flows driven by electric fields and temperature gradients have been studied in a variety of circumstances, it is not clear how these external forces may affect thin films with contact lines that are driven by gravity.

A common feature of gravity-driven film flows (as well as films driven by forces other than gravity such as electric fields [18] and temperature gradients [19]) is the formation of a ridge of liquid near the advancing film front known as the capillary ridge. The capillary ridge has been shown to promote instabilities in the transverse direction of flow which can result in fingers or streaks covering a portion of the substrate. Additionally, nonuniformities in film height will be subject to different magnitudes of electric and temperature fields, which in turn generate liquid flow that might oppose surface tension's tendency to smooth out liquid interfaces. In Chapter 3, I study how electric and temperature fields affect the gravity-driven spreading of constant-volume liquid films on inclined planes. I use a 2-dimensional model with finite-differences to examine how the shape of the liquid-air interface responds to the presence of electric and temperature fields. Simulations are conducted for a variety of liquids, ranging from non-conductive to weakly conductive and from perfectly to partially wetting.

1.3 Stability of dynamic contact lines

A fundamental issue in coating flows is maintaining a stable film profile in order to ensure uniform coverage of the substrate. The requirement of stability is most critical at the front of a liquid film where air, liquid, and solid substrate meet, a region which is referred to as the contact line. In thin films driven by body forces, this contact line can become

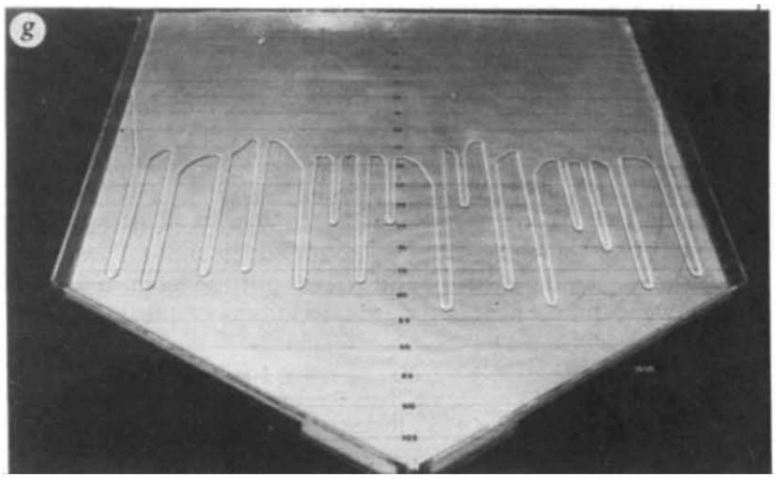

Figure 1.2: Example of fingering instability observed in flow of glycerine film down an inclined plane. Image taken from Huppert (1982) [3].

unstable to transverse perturbations, or perturbations lying in the plane of the substrate but perpendicular to the direction of flow. These perturbations can grow into fingers or rivulets which travel down the length of the substrate, resulting in a partially-coated streaky surface instead of a uniform coating. Anyone who was applied too much paint to a brush while painting a wall in his/her house has observed the streaks which slide down the vertical surface. In this situation it is easy enough to smooth out the mistake, but in automated coating processes it could be costly not only to have to closely inspect every square centimeter of a surface, but then to smooth out any nonuniformities which arose do to the fingering instability. It would be best to be design coating processes such that the fingering instability is unlikely to occur at all.

A particularly egregious example of the fingering instability was seen in glycerine flows by Huppert (1982) [3] and is shown in Figure 1.2. Initially the front of the glycerine film was straight, but as the film moves down the substrate mechanical vibrations or roughness on the substrate can perturb the initially uniform front. The resulting fingering instability can be ruinous in any process which relies upon steady, uniform flow down an inclined or vertical plane. It is critical to understand what parameters the contact-line instability depends upon and to seek out methods for inhibiting the developments of these rivulets.

In the decades after Huppert published his results on the fingering instability in glycerine flows, several groups set out to study the development of the fingers. Silvi and Dussan (1984) [20] performed experiments to study the effect of contact angle on the surface coverage. Troian et al. (1989) [21] performed a linear stability analysis to study the effect that the cross-sectional profile of the film had on the fingering instability. Since then, a number of theoretical studies have been conducted in order to refine the numerical model [14, 15, 22] and/or gain insight on how various other factors affect the development of the instability (for viscoelasticity, see Spaid and Homsy (1996) [23]; for transient effects, see Bertozzi and Brenner (1997) [24]; for the inclination angle, see Kondic and Diez (2001) [25]. Improvement to experimental techniques have also been made by Johnson et al. (1999) [26] by using fluorescent imaging to better measure the finger spacing, tip velocity, and three-dimensional shape of the film.

With the interest in controlling liquids at small length scales growing rapidly, it is worth taking another look at the development of the fingering instability and what tools may be available to inhibit it. Electric fields and temperature gradients offer two potential methods for exerting control over the contact-line instability of a driven spreading film. In Chapter 4, I use a linear stability analysis to study the effects of electric and temperature fields on the contact-line instability of a gravity-driven spreading film. Furthermore, I perform an energy analysis to gain insight on the physical mechanisms through which the electric and temperature fields affect the stability of the contact line.

1.4 Electrohydrodynamics

Electric fields have been used as a means of manipulating liquids for over a century [27]. Throughout the first half of the twentieth century, studies focused on either perfectly conducting liquids such as mercury and water or perfect dielectrics such as benzene and other organic liquids [28]. Although a perfect dielectric liquid does not conduct charge, its molecules contain dipoles which become aligned with each other in the presence of an external electric field. In a homogeneous bulk liquid, the positive and negative ends of each dipole will be close in proximity and cancel each other out. However at a liquid interface, assuming the liquids do not have equal relative permittivities, there will be an interfacial layer with a net partial charge. The electric field exerts a force on this layer

and can influence or generate interfacial flows.

In the second half of the twentieth century, it was discovered that extremely small conductivities could allow enough charge to accumulate at liquid interfaces to observe phenomena that could not be explained using either the perfect conductor or perfect dielectric models [29, 30]. This discovery led to the development of the leaky dielectric model for the description of weakly conductive liquids. The first quantitative experimental comparisons to the leaky dielectric model were made by Torza et al. (1971) [31] using both steady and oscillatory electric fields to study drop behavior. The qualitative aspects of the drop behavior were captured well by the leaky dielectric model, however quantitative agreement was lacking. A number of later studies attempted to resolve the discrepancy between theory and experiments by making the electrohydrodynamic theory more general (including some nonlinear electric field terms [32], including electrokinetic effects [33]), but little improvement was found. Eventually further experiments were conducted, and Vizika and Saville (1992) [34] found that careful measurement of physical properties such as conductivity was critical to improving agreement between theory and experiment.

Made possible in part by improved agreement between electrohydrodynamic theory and experiments, electrohydrodynamic models have been used to understand a variety of natural and industrial liquid flows, ranging from blue haze appearing above heavily forested areas [35] to electrohydrodynamic jet printing and electrospray coating. Electric fields are of increasing interest in thin film flows due to their ability to control liquids at small length scales [36, 37], and they also have demonstrated to be of use in suppressing the coffee ring effect observed in evaporating colloidal flows [38]. As improved computing power has allowed more rigorous and more general models to be tested, electrohydrodynamics continues to be a field with rich opportunities for exploring new methods of controlling microscale liquid flows.

1.5 Thesis overview

Each of the remaining chapters of this thesis focuses on a specific problem that is relevant to the issues discussed in the preceding sections. Here we briefly describe the problems that are discussed in the upcoming chapters.

1.5.1 Combined electrohydrodynamic and thermocapillary patterning of thin liquid films

In Section 1.1 we discussed some of the challenges associated with patterning of liquid films at micron to sub-micron length scales. The difficulty in fabricating patterned lithographic masks has motivated the search for techniques which do not require pre-patterned equipment, such as thermocapillary and electrohydrodynamic patterning. In Chapter 2 we examine the combined thermocapillary and electrohydrodynamic patterning of thin polymer liquid films. We solve the Stokes equations in the lubrication limit for both Newtonian and non-Newtonian liquids and perform a linear stability analysis to investigate the effects of simultaneous application of electric and temperature fields. We investigate both perfect dielectric and leaky dielectric liquids, as well as heat transfer through both thermal conduction and convection. Through this work, we gain insight into the conditions under which the electric field and temperature field will play the largest role in the patterning process.

1.5.2 Spreading of thin droplets of perfect and leaky dielectric liquids on inclined surfaces

In Section 1.2 we discussed some common coating processes that can involve liquid flow down an inclined plane. Both electric and temperature fields may be present either by design or accident, and it is not clear what effects these forces may have on spreading droplets. In Chapter 3 we investigate how electric and temperature fields can influence the gravity-driven spreading of long, slender, two-dimensional liquid drops. We again consider both perfect and leaky dielectric liquids, but for heat transfer we assume only thermal conduction is relevant. We also compare how electrohydrodynamic and thermocapillary effects influence perfectly and partially wetting liquids. In particular, we focus on how electrohydrodynamics, thermocapillarity, and wetting properties affect the interface of the liquid film and create conditions under which the drop separates into a series of smaller droplets.

1.5.3 Electrohydrodynamic and thermocapillary stabilization of dynamic contact lines

In Section 1.3 we discussed how the contact line of a liquid film undergoing gravity-driven spreading can become unstable and lead to the growth of fingers which hurt the uniformity of a liquid coating. Through their influence on the interface of gravity-driven liquid films, both electric and temperature fields can influence the tendency of the contact-line region to become unstable. In Chapter 4, we examine the effects that electric and temperature fields have on the interface shape and stability of gravity-driven liquid films in the lubrication limit. We consider perfect dielectric liquids and assume heat transfer occurs through thermal conduction. In particular, we find that both electric and temperature fields can stabilize the contact line and examine the physical mechanisms behind these observed phenomena.

Chapter 2

Combined electrohydrodynamic and thermocapillary patterning of thin liquid films

2.1 Introduction

Surface topography plays an important role in the function of many materials. The physical characteristics of a surface affect how the material reflects light, conducts electricity, and even how cells can grow on the surface [4]. For materials in the form of thin liquid films, surface topography can be altered by various phenomena (such as surface charge [39], evaporation [40], thermocapillary forces [41, 42], etc.) and then locked in by solidifying the film. Because a material's properties can be so strongly affected by its surface topography, it is of interest to understand at a fundamental level how various forces interact with and shape the surfaces of thin liquid films.[1]

One technique for modifying surface topography that has been investigated recently [43, 44, 1, 45] is called electrohydrodynamic (EHD) patterning. In EHD patterning, a liquid film is deposited onto a substrate and then exposed to an electric field perpendicular to its surface. Two electrohydrodynamic models [28] have been used to describe the films. The "perfect dielectric" model assumes the film has no conductivity. In this case,

[1] This chapter was originally published as A. Corbett and S. Kumar "Combined thermal and electrohydrodynamic patterning of thin liquid films" *Journal of Engineering Mathematics* 94 (2015) 81-96.

destabilization of the film surface is a result of the cumulative effect of electric dipoles aligning under the influence of the electric field. The more general "leaky dielectric" model assumes the bulk of the film has negligible charge, but the film's finite conductivity allows charge to build up at the interface over time. In this case, the electric field acts on both the polarized film and the charge which accumulates at the interface. Numerous studies have investigated EHD patterning [39, 7, 46, 47, 48, 49, 8] and generally have shown leaky dielectric films to pattern more quickly and generate smaller features than perfect dielectric films.

Another process for patterning films that has also been studied [50, 51, 52, 12, 53, 13] and is related to EHD patterning is called thermal patterning. In thermal patterning, the polymer film is heated from the substrate it is resting on, and cooled from a mask suspended above. When the temperature of a film is nonuniform, a disturbance at the surface will cause the surface temperature to be nonuniform as well. The surface tension of most fluids decreases as temperature is raised. If the peaks of a wave are at a lower temperature than the troughs, as will be the case in thermal patterning, then fluid will flow toward the peaks resulting in the destabilization of the film surface.

In theoretical studies of EHD patterning, the film is assumed to be at a uniform temperature or to possess only temperature-independent properties. It is possible that the temperature in the film is nonuniform and that the resulting Marangoni forces could affect the pattern observed on the film. In order to harness the destabilizing effects of both EHD and thermal patterning, a film undergoing EHD patterning could be subject to a temperature gradient in an identical fashion as is used in thermal patterning. This simultaneous application of electric and thermal fields, hereafter referred to as "thermal-EHD patterning", could unlock regimes of feature size inaccessible through use of only one of the two methods.

In this paper, we study the thermal-EHD patterning of a single-layer polymer film via a linear stability analysis as well as nonlinear simulations. For simplicity we focus most analysis on the thermal-EHD patterning of Newtonian fluids. However in the linear stability analysis we also consider viscoelastic effects using the Jeffreys constitutive model. The Jeffreys model is a linear model that treats the film as a polymer dissolved in a Newtonian solvent and has previously been used to investigate viscoelastic effects in EHD patterning [10, 11, 9]. We begin the paper by introducing the model that we

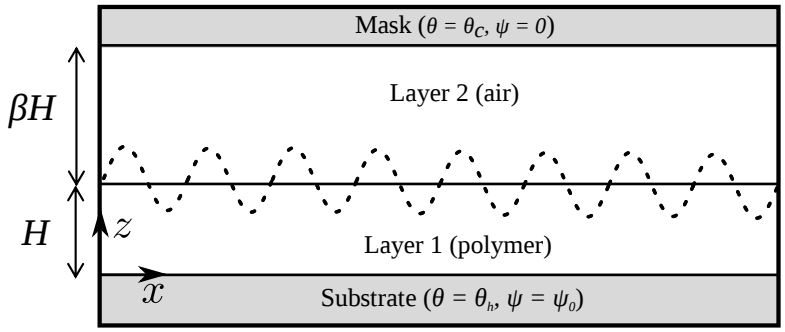

Figure 2.1: Schematic of problem geometry

use, then discuss the results of the linear stability analysis and nonlinear simulations.

2.2 Model

We consider a film of thickness H resting on an electrically and thermally conductive substrate (Figure 2.1). A conductive mask rests a distance of βH above the surface of the undisturbed film. The temperature and electrostatic potential in each layer are given by θ_i and ψ_i, respectively. The subscript 1 refers to the film and 2 refers to the air gap. The substrate is held at a constant temperature θ_h and potential ψ_0. The mask is electrically grounded (zero potential) and held at temperature θ_c. It is usually assumed that $\theta_c < \theta_h$. The film has a shear viscosity η_0 and surface tension γ.

The variables x and z represent the horizontal and vertical coordinates, respectively. The film is assumed to extend infinitely in the x direction. The interface of the undisturbed film is located at $z = 0$ and the interface of the disturbed film is located at $z = h(x,t)$. The normal and tangent vectors are given by $\mathbf{n}$ and $\mathbf{t}$, with the normal vector directed upward into layer 2.

We examine two different methods of heat transfer: (1) thermal conduction through the film and (2) thermal convection at the film surface. We assume the film (layer 1) has a thermal conductivity k_1 and the air (layer 2) has a thermal conductivity k_2. For the case of convection, we also denote the fluid-air heat transfer coefficient by α. In general, all physical properties will vary with temperature. However, in order to isolate the influence of Marangoni flows, we allow only the surface tension to vary with

temperature. For pure thermal patterning, this assumption yields predictions in good agreement with experimental measurements [53].

2.2.1 Governing Equations and Boundary Conditions

The electrostatic potentials are governed by Laplace's equation

$$\nabla^2 \psi_i = 0\,, \tag{2.1}$$

with the boundary conditions

$$\psi_1(z = -H) = \psi_0, \tag{2.2}$$

$$\psi_2(z = \beta H) = 0, \tag{2.3}$$

$$\psi_1(z = h) = \psi_2(z = h). \tag{2.4}$$

The interfacial charge q is equal to the jump in the normal component of the electric field [28]

$$q = \{-\varepsilon_i \varepsilon_0 \nabla \psi_i\} \cdot \mathbf{n}, \tag{2.5}$$

where $\{f_i\} = f_2 - f_1$, ε_i denotes the relative permittivity of layer 1 or 2, and ε_0 denotes the permittivity of free space. The electric field $\mathbf{E}_i$ in each layer is related to the potential ψ_i by

$$\mathbf{E}_i = -\nabla \psi_i. \tag{2.6}$$

The creeping-flow equations govern the hydrodynamics of each layer:

$$\nabla \cdot \mathbf{v}_i = 0, \tag{2.7}$$

$$-\nabla p_i + \nabla \cdot \mathbf{T}_i = 0. \tag{2.8}$$

Here, $\mathbf{v}_i = (v_{x,i}, v_{z,i})$ represents the fluid velocity, and p_i is the pressure in each layer of the system. In this study we take the air pressure (p_2) to be negligible. The stress tensor $\mathbf{T}_i$ is the sum of the viscous stress tensor and the Maxwell electrical stress tensor

$$\mathbf{T}_i = \boldsymbol{\tau}_i + \mathbf{M}_i, \tag{2.9}$$

where $\mathbf{M}_i$ is given by

$$\mathbf{M}_i = \varepsilon_i \varepsilon_0 \left[\mathbf{E}_i \mathbf{E}_i - \tfrac{1}{2} (\mathbf{E}_i \cdot \mathbf{E}_i) \mathbf{I} \right], \tag{2.10}$$

and $\mathbf{I}$ is the identity tensor. We assume $\boldsymbol{\tau}_i$ is negligible in the air layer, so for convenience we neglect the subscript 1 when writing the film velocity and viscous stress tensor. As noted earlier, we use the Jeffreys stress tensor to consider viscoelasticity in the linear regime:

$$\boldsymbol{\tau} = \int_{-\infty}^{t} G(t - t') [\nabla \mathbf{v} + (\nabla \mathbf{v})^T] dt', \tag{2.11}$$

where $G(t - t')$ is known as the relaxation modulus

$$G(t - t') = \eta_0 \left[\frac{1}{\lambda_1} \left(1 - \frac{\lambda_2}{\lambda_1} \right) e^{-\frac{t - t'}{\lambda_1}} + 2 \frac{\lambda_2}{\lambda_1} \hat{\delta}(t - t') \right], \tag{2.12}$$

with $\hat{\delta}(t - t')$, λ_1, and λ_2 denoting the Dirac delta function, polymer relaxation time, and polymer retardation time, respectively. Note that in the Newtonian limit, $\lambda_1 = \lambda_2$ and thus $G(t - t') = 2\eta_0 \hat{\delta}(t - t')$, reducing $\boldsymbol{\tau}$ to the Newtonian stress tensor. The hydrodynamics in layer 2 are ignored, so the stress is governed by the Maxwell tensor for the layer.

We impose no-slip and no-penetration at the substrate to get

$$\mathbf{v}(z = -H) = 0. \tag{2.13}$$

The interface is governed by normal and tangential stress balances

$$\{ \mathbf{n} \cdot \mathbf{T}_i \cdot \mathbf{n} \} = \gamma \mathcal{H}, \tag{2.14}$$

$$\{ \mathbf{n} \cdot \mathbf{T}_i \cdot \mathbf{t} \} = \nabla_S \gamma \cdot \mathbf{t}, \tag{2.15}$$

where $\mathcal{H}$ and ∇_S denote the mean curvature and surface gradient, respectively, and are given by

$$\mathcal{H} = [(\mathbf{I} - \mathbf{nn}) \cdot \nabla] \cdot \mathbf{n}, \tag{2.16}$$

$$\nabla_S = \nabla - \mathbf{n}(\mathbf{n} \cdot \nabla). \tag{2.17}$$

It is assumed that the surface tension of the film decreases linearly as temperature

increases.

The energy conservation equation [42] is enforced

$$\rho_i c_i \left(\frac{\partial \theta_i}{\partial t} + v_x \frac{\partial \theta_i}{\partial x} + v_z \frac{\partial \theta_i}{\partial z} \right) = k_i \nabla^2 \theta_i, \tag{2.18}$$

with c_i and ρ_i denoting the specific heat and density of layer i, respectively. Note that in the air gap, we have $v_x = v_z = 0$. The boundary conditions for temperature depend on which mode of heat transfer is assumed to be dominant. For thermal conduction, the boundary conditions are

$$\theta_1(z = -H) = \theta_h, \tag{2.19}$$

$$\theta_2(z = \beta H) = \theta_c, \tag{2.20}$$

$$\theta_1(z = h) = \theta_2(z = h), \tag{2.21}$$

$$\{k_i \nabla \theta_i\} \cdot \mathbf{n} = 0 \text{ at } z = h. \tag{2.22}$$

For convection, we assume the air layer is a thermal reservoir at temperature θ_c and apply Newton's law of cooling at the interface, as well as the fixed-temperature condition at the substrate.

$$k_1 \nabla \theta_1 \cdot \mathbf{n} + \alpha \left(\theta_1(z = h) - \theta_c \right) = 0, \tag{2.23}$$

$$\theta_1(z = -H) = \theta_h. \tag{2.24}$$

In each case, we impose the kinematic condition and charge conservation at the interface

$$\frac{\partial h}{\partial t} = v_z - v_x \frac{\partial h}{\partial x}, \tag{2.25}$$

$$\frac{\partial q}{\partial t} = q\mathbf{n} \cdot (\mathbf{n} \cdot \nabla)\mathbf{v} - \mathbf{v} \cdot \nabla_S \, q + \sigma \mathbf{E}_1 \cdot \mathbf{n}, \tag{2.26}$$

where σ is the electrical conductivity of the film. We assume the air gap acts as a perfect dielectric.

2.2.2 Scalings

Dimensionless variables are defined as follows:

$$\begin{array}{ccc} (v_x, v_z) = (U\bar{v}_x, W\bar{v}_z), & p = P\bar{p}, & q = Q\bar{q}, \\ (x, z) = (L\bar{x}, H\bar{z}), & t = T\bar{t}, & \bar{\theta} = \frac{\theta-\theta_c}{\theta_h-\theta_c}, \\ \bar{\gamma} = \frac{\gamma-\gamma_c}{\gamma_h-\gamma_c} & \bar{\sigma} = \sigma\eta_0 L^2/(\varepsilon_0^2\psi_0^2). & \end{array}$$

Dimensionless variables are denoted by overbars and scales by capital letters. The vertical distance is scaled by the film thickness H. The horizontal velocity is found from the continuity equation to be $U = WL/H$. The pressure scale comes from the x-component of momentum conservation (2.8) and is $P = \eta_0 UL/H^2$. The charge scale comes from equation (2.5) and is $Q = \varepsilon_0\psi_0/H$. The x-component of the momentum balance equations (2.8) gives the vertical velocity scale to be $W = H\varepsilon_0\psi_0^2/(\eta_0 L^2)$. The horizontal length scale comes from the normal stress balance and is $L = \left[H^3\gamma/(\varepsilon_0\psi_0^2)\right]^{1/2}$. Time is simply the length divided by velocity $T = L/U$. $\bar{\theta}$ is the dimensionless temperature. In the expression for dimensionless surface tension $\bar{\gamma}$, γ_c and γ_h denote the surface tension evaluated at temperatures θ_c and θ_h, respectively. A dimensionless conductivity $\bar{\sigma}$ comes from the charge conservation equation (2.26).

2.2.3 Lubrication Equations

After non-dimensionalization, we apply the lubrication approximation. In applying this approximation, we expand each equation in terms of $\hat{\epsilon} = H/L \ll 1$ and keep only the leading-order terms. In this section, we have listed the equations after application of the approximation. All variables are dimensionless, so we have omitted the overbars for convenience.

The governing equations are

$$\frac{\partial v_x}{\partial x} + \frac{\partial v_z}{\partial z} = 0, \tag{2.27}$$

$$-\frac{\partial p}{\partial x} + \int_{-\infty}^{t} G(t-t')\frac{\partial^2 v_x}{\partial z^2} dt' = 0, \tag{2.28}$$

$$\frac{\partial p}{\partial z} = 0, \tag{2.29}$$

$$\frac{\partial^2 \psi_i}{\partial z^2} = 0, \tag{2.30}$$

$$\frac{\partial^2 \theta_i}{\partial z^2} = 0. \tag{2.31}$$

The dimensionless relaxation modulus is given by

$$G(t-t') = \frac{1-\delta}{\mathrm{De}} e^{-(t-t')/\mathrm{De}} + 2\delta\,\hat{\delta}(t-t'), \tag{2.32}$$

where δ is the ratio of the retardation time to the relaxation time (equivalent to a dimensionless solvent viscosity), and De is the Deborah number, given by

$$\delta = \frac{\lambda_2}{\lambda_1}, \tag{2.33}$$

$$\mathrm{De} = \frac{\lambda_1}{T}. \tag{2.34}$$

The boundary conditions are

$$\psi_1(z=-1)=1, \tag{2.35}$$

$$\psi_2(z=\beta)=0, \tag{2.36}$$

$$\psi_1(z=h)=\psi_2(z=h), \tag{2.37}$$

$$q=\varepsilon\frac{\partial\psi_1}{\partial z}-\frac{\partial\psi_2}{\partial z}, \tag{2.38}$$

$$v_x(z=-1)=0, \tag{2.39}$$

$$v_z(z=-1)=0, \tag{2.40}$$

$$p-\frac{1}{2}\left[\varepsilon\left(\frac{\partial\psi_1}{\partial z}\right)^2-\left(\frac{\partial\psi_2}{\partial z}\right)^2\right]+\frac{\partial^2 h}{\partial x^2}=0, \tag{2.41}$$

$$\int_{-\infty}^{t}G(t-t')\frac{\partial v_x}{\partial z}\,dt'+\mathrm{M}\frac{\partial\theta(z=h)}{\partial x}+q\frac{\partial\psi(z=h)}{\partial x}=0. \tag{2.42}$$

In the air layer $\varepsilon_2=1$, so for convenience we let $\varepsilon_1=\varepsilon$. From the tangential stress balance comes the Marangoni number M, defined by

$$\mathrm{M}=\frac{(\gamma_c-\gamma_h)H}{\varepsilon_0\psi_0^2}. \tag{2.43}$$

The Marangoni number is typically defined as a ratio of surface-tension-gradient forces to viscous forces, taking the form $\mathrm{M}=\Delta\gamma H/(\eta_0 UL)$ in the lubrication limit. As described in Section 2.2.2, the horizontal velocity and length scales are obtained from balances of viscous and electrical forces. Thus, the Marangoni number becomes a balance between surface-tension-gradient and electrical forces. When surface tension depends linearly on temperature, $\Delta\gamma$ is proportional to $(\theta_c-\theta_h)$.

For the case of thermal conduction, one uses the following boundary conditions:

$$\theta_1(z=-1)=1, \tag{2.44}$$

$$\theta_2(z=\beta)=0, \tag{2.45}$$

$$\theta_1(z=h)=\theta_2(z=h), \tag{2.46}$$

$$\kappa\frac{\partial\theta_2}{\partial z}-\frac{\partial\theta_1}{\partial z}=0. \tag{2.47}$$

In Equation (2.47), κ represents the ratio of thermal conductivities

$$\kappa = \frac{k_2}{k_1}. \tag{2.48}$$

For the case of convection at the surface, the boundary conditions become

$$\theta_1(z=-1) = 1, \tag{2.49}$$

$$\frac{\partial \theta_1}{\partial z} + \mathrm{B}\theta_1(z=h) = 0, \tag{2.50}$$

$$\theta_2 = 0. \tag{2.51}$$

The Biot number B is defined as

$$\mathrm{B} = \frac{\alpha H}{k_1}. \tag{2.52}$$

The evolution equations are then given by

$$\frac{\partial h}{\partial t} = v_z(z=h) - v_x(z=h)\frac{\partial h}{\partial x}, \tag{2.53}$$

$$\frac{\partial q}{\partial t} = -v_x(z=h)\frac{\partial q}{\partial x} + q\left[\frac{\partial v_z}{\partial z} - \frac{\partial h}{\partial x}\frac{\partial v_x}{\partial z}\right] - \sigma\frac{\partial \psi_1}{\partial z}\bigg|_{z=h}. \tag{2.54}$$

The velocity and potential functions are obtained by solving equations (2.27)-(2.30) and boundary conditions (2.35)-(2.42). The temperatures in each layer are obtained using equation (2.31) and either boundary conditions (2.44)-(2.47) or (2.49)-(2.51), depending on the mode of heat transfer.

In order to recover the perfect dielectric case, one must set $q(x,t) = 0$ and $\sigma = 0$. In the Newtonian ($\delta = 1$) limit, this results in the height evolution equation given by

$$\begin{aligned}\frac{\partial h}{\partial t} = -\frac{\partial}{\partial x}\Bigg[&\frac{1}{3}(1+h)^3\frac{\partial^3 h}{\partial x^3} \\ &+ \left(\frac{\varepsilon(\varepsilon-1)^2(1+h)^3}{3(h(1-\varepsilon)+1+\beta\varepsilon)^3} + \frac{\mathrm{M}\kappa(1+\beta)(1+h)^2}{2(h(\kappa-1)+\kappa+\beta)^2}\right)\frac{\partial h}{\partial x}\Bigg]\end{aligned} \tag{2.55}$$

Even in the Newtonian limit, the final forms of the leaky dielectric evolution equations are cumbersome and thus are given as Equations (A.1) and (A.2) in the appendix.

2.3 Results

2.3.1 Linear Stability Analysis

We begin our investigation by conducting a linear stability analysis. We consider four scenarios, choosing one of two forms of heat transfer (conduction or convection) and one of two electrohydrodynamic models (perfect dielectric or leaky dielectric). Each variable is described by a normal mode decomposition as outlined below:

$$f = f_0 + \tilde{f}\, e^{i\,k\,x} e^{c\,t} \tag{2.56}$$

where the subscript 0 denotes the base state, the tilde denotes the perturbation, and k and c are the wave number and growth rate, respectively. We will focus mainly on the results from thermal conduction, but briefly discuss thermal convection as well.

Perfect Dielectric

We first consider the case of heat transfer by thermal conduction through a perfect dielectric film. The normal mode decomposition reduces the height evolution equation (2.55) to the following dispersion relation

$$c = \frac{1}{\eta}\left[-\frac{k^4}{3} + \frac{\varepsilon(\varepsilon-1)^2}{3(1+\beta\,\varepsilon)^3}k^2 + \frac{\mathrm{M}\,\kappa(1+\beta)}{2(\beta+\kappa)^2}k^2\right], \tag{2.57}$$

where η is the frequency-dependent viscosity defined by

$$\eta = \frac{1+\delta\,\mathrm{De}\,c}{1+\mathrm{De}\,c}. \tag{2.58}$$

For the time being, we will assume the film is Newtonian ($\delta = 1$). In this case, the growth rate is simply the sum of three uncoupled contributions. The first term originates from the stabilizing force of surface tension, the second represents the destabilizing electric polarization force, and the third term represents the destabilizing Marangoni force. It is also possible to solve for the most unstable wave number k_{MU} for a given set of

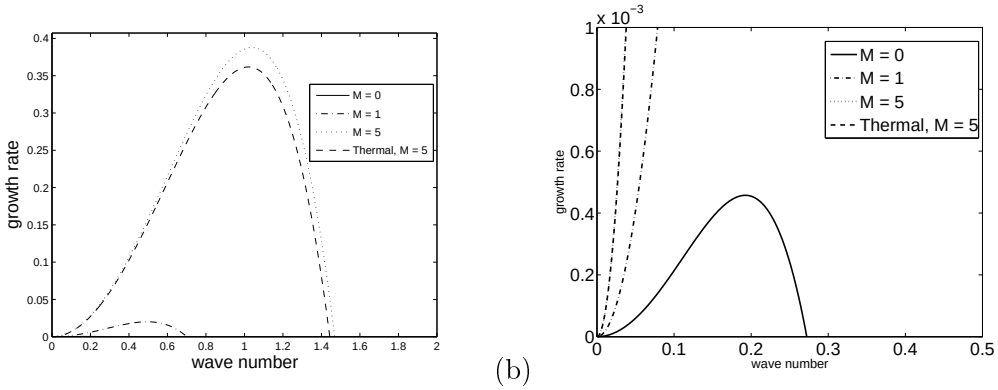

(a) (b)

Figure 2.2: (a) Growth rate curves for various Marangoni numbers (perfect dielectric). Values of other variables are: $\beta = 1$, $\varepsilon = 2$, $\kappa = 5$. The dashed line labeled "Thermal, M = 5" represents the case of patterning in the absence of an electric field. (b) Magnification of panel (a).

parameters, which is shown in equation (2.59),

$$k_{MU} = \left[\frac{\varepsilon(\varepsilon - 1)^2}{2(1 + \beta\,\varepsilon)^3} + \frac{3\mathrm{M}\kappa(1 + \beta)}{4(\beta + \kappa)^2} \right]^{1/2}. \tag{2.59}$$

Figure 2.2 illustrates how the Marangoni number affects the thermal-EHD patterning of a perfect dielectric film. As noted before, the Marangoni number M is proportional to the temperature difference between the substrate and the mask. Positive M corresponds to a heated substrate relative to the mask, thus destabilizing the surface of the film and promoting instability growth. The curve where M = 0, which represents typical EHD patterning in the absence of thermal effects, is dwarfed by the curves with M > 0 to a degree such that the dispersion relation cannot even be seen in panel (a). It is clear from Figure 2.2 that the growth rates are significantly enhanced by the presence of a thermal gradient.

Varying the Marangoni number allows one to control the magnitude of the thermal effects without altering the electric field at all. In contrast, altering the gap thickness β simultaneously affects both the thermal and electric effects. One can see from simply examining the dispersion relation that the electric contribution decays as β^{-3}, but the Marangoni term has a maximum at $\beta = \kappa - 2$ before decaying as β^{-1}. As a consequence,

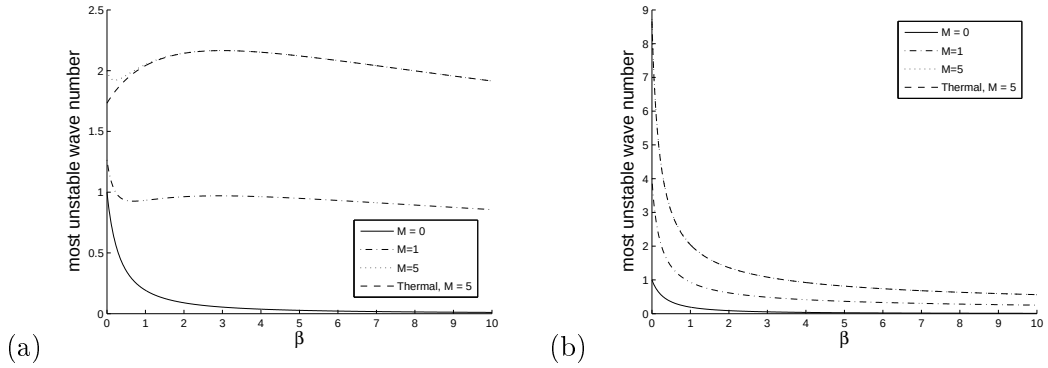

Figure 2.3: Dependence of most unstable wave number on β (perfect dielectric). Values of other parameters are: (a) $\varepsilon = 2$, $\kappa = 5$, (b) $\varepsilon = 2$, $\kappa = 0.2$.

in pure Marangoni patterning when $\kappa > 2$ there will be an ideal gap thickness for maximizing k_{MU}, while electric polarization slightly reduces this ideal gap thickness. Figure 2.3 shows the effect that gap thickness has on k_{MU} at various Marangoni numbers. However, in most cases $\kappa < 1$ and thus the most unstable wave number is maximized by minimizing β, as shown in Figure 2.3 (b).

As noted before, the thermal and thermal-EHD growth-rate curves dwarf the EHD curves for perfect dielectric films. This suggests that in terms of observed feature size, in perfect dielectric films an electric field will be of little to no consequence when compared to the thermal gradient.

Leaky Dielectric

Linearizing the leaky dielectric evolution equations (2.53) and (2.54) and applying the normal mode decomposition yields the following equation:

$$c \begin{pmatrix} \tilde{h} \\ \tilde{q} \end{pmatrix} = \begin{pmatrix} a_{11} & a_{12} \\ a_{21} & a_{22} \end{pmatrix} \begin{pmatrix} \tilde{h} \\ \tilde{q} \end{pmatrix},$$

$$a_{11} = \frac{1}{\eta}\left[-\frac{k^4}{3} + \left(\frac{(3+2\varepsilon)}{6\,\beta^2(1+\beta\,\varepsilon)} + \frac{\mathrm{M}\,\kappa(1+\beta)}{2(\beta+\kappa)^2}\right)k^2\right], \tag{2.60}$$

$$a_{12} = \frac{1}{\eta}\left[\frac{(2-3\beta)}{6\,\beta(1+\beta\,\varepsilon)}k^2\right], \tag{2.61}$$

$$a_{21} = \frac{1}{\beta\,\eta}\left[-\frac{k^4}{2} + \left(\frac{(2+\varepsilon)}{2\,\beta^2(1+\beta\,\varepsilon)} + \frac{\mathrm{M}\,\kappa(1+\beta)}{(\beta+\kappa)^2}\right)k^2\right] + \frac{\sigma}{\beta(1+\beta\,\varepsilon)}, \tag{2.62}$$

$$a_{22} = \frac{(1-2\beta)}{2\,\eta\,\beta^2(1+\beta\,\varepsilon)}k^2 - \frac{\beta\,\sigma}{(1+\beta\,\varepsilon)}. \tag{2.63}$$

As in previous sections, we focus our analysis on the case of a Newtonian film, namely $\delta = 1 \Rightarrow \eta = 1$. Letting $n_{ij} = a_{ij}(\delta = 1)$, we recover expressions for two roots of the eigenvalue problem

$$c_{N,u} = \frac{n_{11}+n_{22}}{2} + \frac{\sqrt{(n_{11}-n_{22})^2 + 4\,n_{12}\,n_{21}}}{2} \tag{2.64}$$

$$c_{N,s} = \frac{n_{11}+n_{22}}{2} - \frac{\sqrt{(n_{11}-n_{22})^2 + 4\,n_{12}\,n_{21}}}{2} \tag{2.65}$$

One can verify that $c_{N,s}$ is always stable, so we are generally only interested in the mode $c_{N,u}$ that has positive values for certain wave numbers. Note that in contrast to the perfect dielectric case, the contributions of surface tension, electrical forces, and thermal effects to the growth rate are all coupled together. Thus, it is not apparent how the growth rate is influenced by each of these factors without looking at the behavior of equation (2.64) for different cases.

As shown in Figure 2.4, the Marangoni number affects leaky dielectric films in a manner similar to how it affects perfect dielectric films, increasing both the most unstable wave number and growth rate of the instability. However, unlike the case of perfect dielectrics, electrostatic forces do have a significant effect on instability growth. For the case shown in Figure 2.4, there is a difference of roughly 7% in the most unstable wave numbers and 33% in growth rates for thermal patterning at $\mathrm{M} = 10$ and thermal-EHD patterning at $\mathrm{M} = 10$.

In Figure 2.5, it is seen that the most unstable wave number depends on β in qualitatively the same way as in the perfect dielectric case. However, whereas in perfect

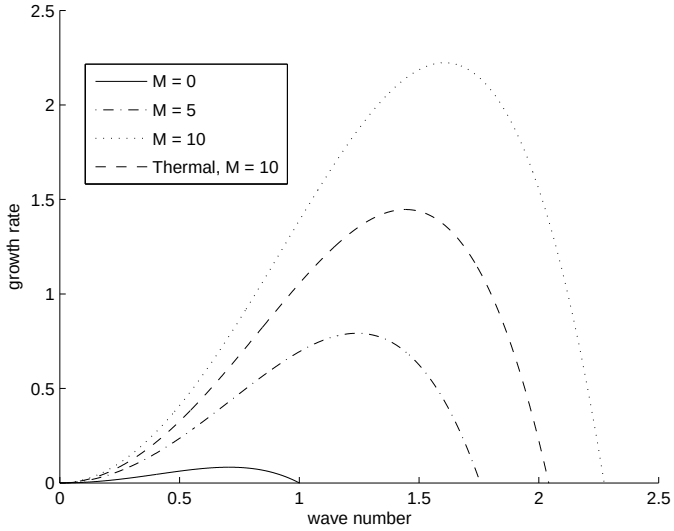

Figure 2.4: Effect of Marangoni number on thermal-EHD patterning of leaky dielectric film. Values of other parameters are: $\beta = 1$, $\varepsilon = 2$, $\sigma = 1000$, $\kappa = 5$.

dielectric films with $\kappa > 2$ one could see clearly defined maxima in k_{MU} relative to β, the maxima in leaky dielectric films are much less pronounced. Thus, the wavelength one observes in a leaky dielectric film becomes almost constant once β is greater than approximately 2. Figure 2.5 also tells us something about the relative magnitude of electric and thermal effects in separate regimes of β. For small air gaps, the strength of the electric field relegates the thermal gradient to play only a minor role. For large β ($\beta > 2$), the electric effects are playing the minor role. When the thickness of the air gap is approximately the same as the film thickness ($0.5 < \beta < 2$), one can see significant increases in k_{MU} going from pure thermal patterning or EHD patterning to thermal-EHD patterning. This intermediate regime is where one expects to find the greatest benefit from simultaneous application of temperature and electric fields.

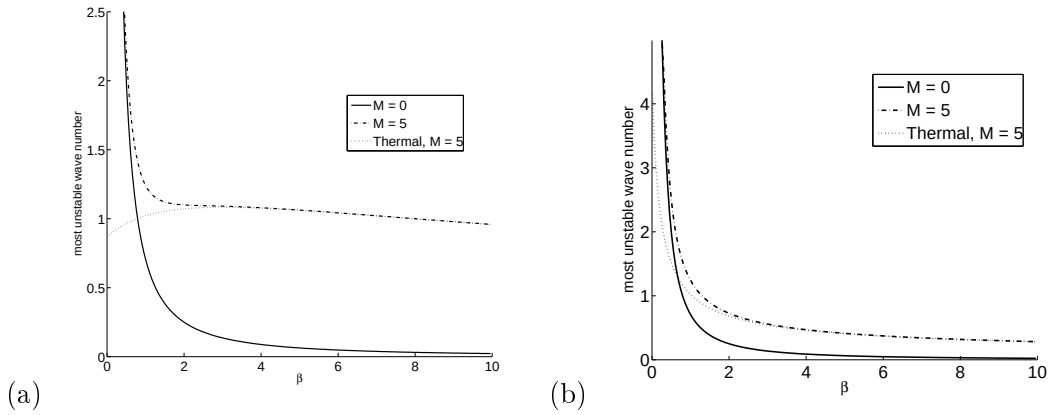

Figure 2.5: Effect of gap thickness β on most unstable wave number for leaky dielectric Newtonian films at various Marangoni numbers. Values of other parameters are: (a) $\varepsilon = 2$, $\sigma = 1000$, $\kappa = 5$, (b) $\varepsilon = 2$, $\sigma = 1000$, $\kappa = 0.2$.

Thermal Convection

When studying the case of heat transfer by thermal convection, we use the boundary conditions (2.49) and (2.50) to determine the temperature profile in the film. The qualitative trends are the same as those shown in Figures 2.2 and 2.4, with the growth rates and most unstable wave number increasing with M. However, the magnitude of convective thermal effects on thermal-EHD patterning depends on the Biot number as well as the Marangoni number. Recall from equation (2.52) that the Biot number is proportional to the film thickness H. Thus, in laboratory scale experiments such as those performed by McLeod et al. [13], where the film thicknesses were $\sim$160 nm, the Biot number would be quite small ($\sim 10^{-6}$). In these cases convective thermal effects are negligible compared to thermal conduction and electric effects, even in perfect dielectric films and certainly in leaky dielectric ones. This raises the following question: in what range of Biot numbers will one be able to notice convective thermal effects? Figure 2.6 reveals that the optimal Biot number is unity. However, the most unstable wave number begins to rise noticeably at B $\sim 10^{-2}$, corresponding to film thicknesses in the millimeter to centimeter range.

One also must consider the validity of Newton's law of cooling. One of the assumptions is that there is a thermal boundary layer just above the surface of the film and that

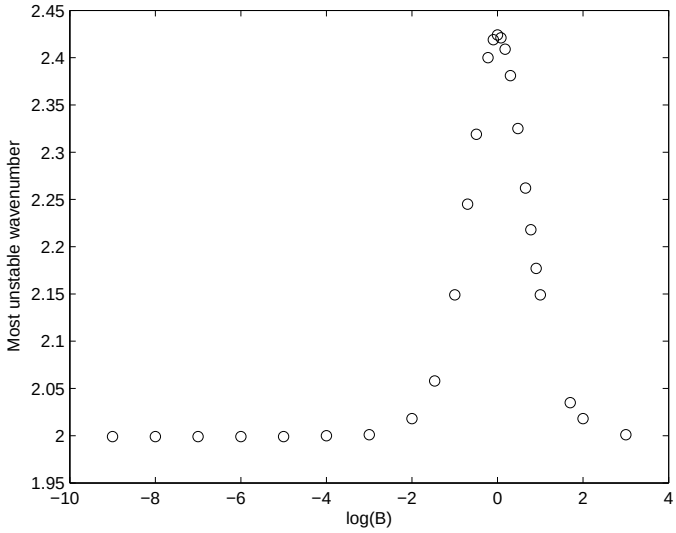

Figure 2.6: Dependence of most unstable wave number on $\log_{10}$ of the Biot number. Other parameters constant at values of: $\beta = 0.5$, $\varepsilon = 2$, $M = 2$, $\sigma = 1000$.

the temperature of the rest of the air layer is approximately constant. This assumption is valid when the air gap is sufficiently large and there is freely moving air above the surface of the film. This might be the case for films moving on a belt or for stationary films cooled with a fan, or for films thick enough that thermal conduction is slow compared to convection.

Viscoelastic Effects

Thus far we have analyzed only the patterning of Newtonian fluids, despite having conducted the linear stability analysis using the Jeffreys model for viscoelasticity. The Jeffreys model treats the fluid as a polymer dissolved in a Newtonian solvent and is characterized by two dimensionless numbers, the Deborah number De and the solvent viscosity δ. The limit of a Maxwell fluid is recovered when $\delta = 0$.

The Deborah number reflects the time scale for stress relaxation and the solvent viscosity inhibits the storage of elastic energy during deformation [54]. Although several viscoelastic models have been used in the study of EHD patterning, the effects of

viscoelasticity on thermal patterning have not yet been studied. In this section we will briefly examine the effect that each of these parameters has on patterning.

When one describes a perfect dielectric film with the Jeffreys model, instead of a single growth rate two are obtained. Letting c denote the expression given by equation (2.57) when $\eta = 1$, we obtain the following growth rates for a Jeffreys film:

$$c_{Jeff,u} = \frac{c\mathrm{De} - 1 + \sqrt{(1 - c\mathrm{De})^2 + 4\delta c\mathrm{De}}}{2\delta\mathrm{De}} \tag{2.66}$$

$$c_{Jeff,s} = \frac{c\mathrm{De} - 1 - \sqrt{(1 - c\mathrm{De})^2 + 4\delta c\mathrm{De}}}{2\delta\mathrm{De}} \tag{2.67}$$

Again, we find that one mode is unstable and the other stable. For leaky dielectric films, setting the determinant of the matrix given at the beginning of Section 2.3.1 equal to zero produces a fourth-order polynomial equation, as observed in prior analyses of EHD patterning [10, 11, 9]. The impact of viscoelasticity on these systems is not immediately obvious due to the additional tangential stress that enters through the temperature field.

It is found that viscoelasticity affects perfect and leaky dielectric materials in very similar ways. For both perfect and leaky dielectric films, greater solvent viscosity decreases the growth rate, and greater Deborah numbers tend to increase it. Figure 2.7 shows the effects of De and δ on leaky dielectric films. It can be seen in Figure 2.7 that neither parameter appears to have a noticeable effect on the most unstable wave number. This is also the case for pure thermal patterning (results not shown). According the Jeffreys model, viscoelasticity seems to affect thermal-EHD patterning in exactly the same way as it affects EHD patterning [10, 11, 9].

2.3.2 Nonlinear Simulations

Linear stability theory serves as a useful tool for obtaining explicit equations for the size of the initially fastest growing perturbation as a function of experimental parameters. However it is only strictly valid for small-amplitude disturbances and is not guaranteed to be reliable when those disturbances have grown large. For that information, it is necessary to examine the nonlinear evolution equations. Due to the complexity of the

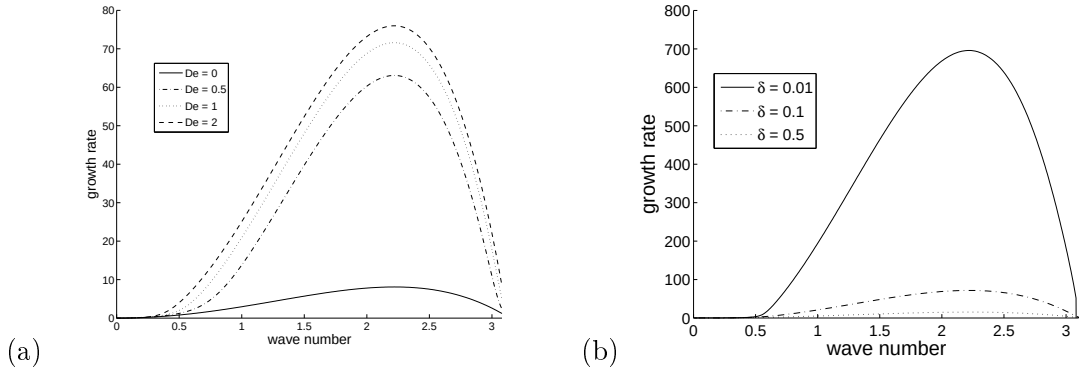

Figure 2.7: (a) Dispersion relations at various Deborah numbers. Values of other parameters are: $\delta = 0.1$, $\beta = 0.5$, $\varepsilon = 2.5$, $\sigma = 1000$, M $= 5$, $\kappa = 5$. (b) Dispersion relations at various viscosities. Values of other parameters are: De $= 1$, $\beta = 0.5$, $\varepsilon = 2.5$, $\sigma = 1000$, M $= 5$, $\kappa = 5$.

problem, we have assumed the film to be Newtonian ($\delta = 1$) in all of the nonlinear simulations. We use a fourth-order accurate finite-difference scheme with periodic boundary conditions to discretize the domain. After discretizing the variables, we integrate equations (A.1) and (A.2) over time with the DASPK3.1 package. In the simulations described here, the initial condition was a perturbation of magnitude $\beta/1000$ with wave number equal to the most unstable wave number predicted by linear theory.

The linear stability analysis for leaky dielectric films shows that there are important contributions from both thermal conduction and electric effects in patterning. The nonlinear evolution of a leaky dielectric film undergoing thermal-EHD patterning is of particular interest because the fluid at the interface is subject to two shear stresses: stress from the surface tension gradient induced by the temperature field, and stress from the electric field acting on charge (see equation (2.42)). It can be seen from inspection of equations (A.1) and (A.2) that the Marangoni terms, or more specifically the derivatives of the temperature at the fluid-air interface, appear in the evolution equations for both height and charge. It is not clear from simply inspecting the equations how the Marangoni terms affect the EHD patterning process.

In general, the nonlinear simulations confirm the conclusions of the linear stability analysis. Figure 2.8 shows the result of a simulation of thermal-EHD patterning for one set of parameters, but the result is qualitatively similar for other cases. As can

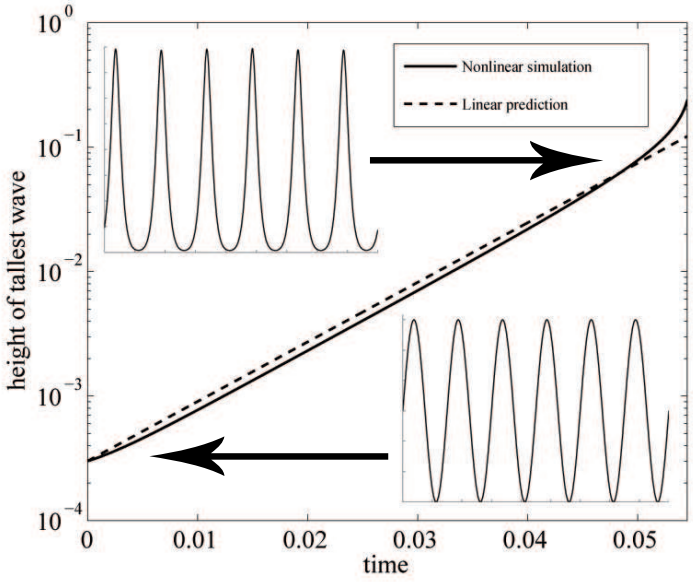

Figure 2.8: Comparison of growth as predicted by linear stability analysis and nonlinear simulations. Values of parameters are: $\beta = 0.3$, $\varepsilon = 2.5$, $\sigma = 1000$, $\kappa = 5$, M $= 5$. Insets show the profile of pillars at start of patterning (amplitude of perturbation $\approx \beta/1000$) and just before contact with mask.

be seen in Figure 2.8, the rate of patterning in the nonlinear simulations is very close to that predicted by the linear theory until the pillars reach approximately 90% of the gap height, at which point the nonlinear growth begins to exceed the linear prediction. The shape of the pillars gradually changes from a simple sine wave to waves with sharp curvature at the peaks and shallow curvature at the troughs; this was no different from simulations of either pure EHD patterning or pure thermal patterning. Simulations with random initial conditions were also run and verified that the most unstable wavelength matches the prediction of linear theory. Analogous results are observed in simulations of perfect dielectric films.

2.4 Conclusions

We have presented a theoretical study of how thermal and electrohydrodynamic effects may be used simultaneously in the patterning of polymer films. It was shown that in the case of perfect dielectric films, the destabilizing force from thermal conduction dwarfs that of electric polarization. In leaky dielectric films, it was seen that when the thicknesses of the air gap and film height are approximately equal, both electrohydrodynamic and thermocapillary forces have noticeable effects on the most unstable wave number. Nonlinear simulations showed close agreement with the length scales and growth rates predicted by linear theory. The combined destabilizing forces serve to generate smaller wavelengths than would be observed in either EHD or thermal patterning alone. Inclusion of viscoelasticity via the Jeffreys model showed that in agreement with previous studies, controlling rheology serves to modify the growth rate of waves without affecting the most unstable wave number. We note that none of these results can be inferred easily without carrying out a detailed analysis, due to the complex coupling between electric, thermal, and viscoelastic effects.

This paper shows how combined thermal-EHD patterning may provide a way of generating even smaller features than are possible through only thermal or EHD patterning. It also demonstrates in what regimes each mechanism is most important, which may help guide experimental studies in this area. Experiments show that polystyrene lends itself to both thermal [52, 13] and EHD [1] patterning making it an ideal candidate as a test material. Polymethylmethacrylate has also been used in both thermal [12] and EHD [43] patterning experiments. For best comparison to the results described in this paper, the parameters would be of the following orders: $h_0 \sim 1\,\mu m$, $\Delta T \sim 10 - 100^o\mathrm{C}$, $\psi_0 \sim 30\,V$. It would be useful to extend the present work to a two-dimensional system in order to see how the Marangoni-charge interaction might affect pattern symmetry in addition to wavelength.

Chapter 3

Spreading of thin droplets of perfect and leaky dielectric liquids on inclined surfaces

The conceptually simple system of a droplet spreading down an inclined plane has been of interest for decades [3]. Experiments reveal and theory confirms that the initially uniform front of the droplet is unstable to perturbations in the transverse direction. In applications where uniformity of the resulting liquid film is critical, these instabilities can be detrimental to a film's usefulness. The gravity-driven flow of droplets is relevant to spray coating [55] and other processes [56] for coating discrete objects such as medical devices [55], solar cells [57], and microchips [58].

At the droplet front, competition between the gravitational driving force and viscous resistance causes a ridge of liquid to rise above the rest of the film. This ridge, which is smoothed by surface tension and thus called the capillary ridge, is largely responsible for the transverse instability that develops in this region of the film [21, 23, 24]. The transverse instability leads to the formation of fingers and uneven coating [21, 14, 15, 23, 24]. The ridge behavior is strongly dependent on parameters including but not limited to fluid properties, the inclination angle, and film thickness. Other forces, such as those arising from electric fields, may also play important roles and could possibly be used to manipulate droplet spreading. It is thus of interest to advance physical understanding

of how electric fields and other external forces influence capillary-ridge behavior.

The study of how electric fields influence flows, electrohydrodynamics, is of increasing importance in the search for methods of controlling liquids at the micro- and nano-scales. In addition to being a possible means for manipulating droplet spreading, the effects of electric fields are of interest for two other reasons. First, it is possible that static charge can accumulate on a substrate resulting in an electric field through a liquid film coating it [59]. Second, in both electrospray deposition [60] and electrohydrodynamic jet printing [61], a voltage is supplied at the nozzle ejecting droplets, possibly resulting in an electric field through the film that forms when a droplet contacts a substrate.

The related field of electrowetting principally involves the study of how electric fields modify the static contact angles of liquid-solid systems. The Young-Lippmann equation [62, 63, 64] shows that the static contact angle decreases when a small electric field is applied, and electric fields have been shown to impact precursor-film formation [65]. A technique separate from electrowetting, dielectrophoresis has been shown experimentally [66, 18, 67] (as well as numerically in [67]) to be a means of deforming thin liquid films under a non-uniform electric field. Electric fields can be used for droplet manipulation on horizontal substrates [36, 37, 68, 69, 70, 71, 72, 73, 74, 75, 76, 77], controlling contact-angle hysteresis on inclined planes [78], and deforming drops containing colloidal particles [79, 38]. The effects of electric fields on gravity-driven flow of thin films over topography in the absence of contact lines have also been studied for perfectly conducting liquids [80] and perfect dielectric liquids [81]. All of these configurations are relevant to microfluidics [82]. Despite this prior work, little is understood about how a normal electric field will affect the gravity-driven spreading of a droplet down an inclined plane.

In this study, we apply lubrication theory to investigate how an electric field influences the gravity-driven spreading of a thin, constant-volume droplet down an inclined plane. We focus on the evolution of the droplet profile, and not the development of a fingering instability (which will be the focus of future work). The inclusion of an electric field is a significant difference from previous studies of gravity-driven droplet spreading, and it is not at all obvious what effects the electric field will have due to the highly nonlinear way it is coupled with the other problem variables. By incorporating the effects of gravity, our study also extends previous work concerning the use of electric fields

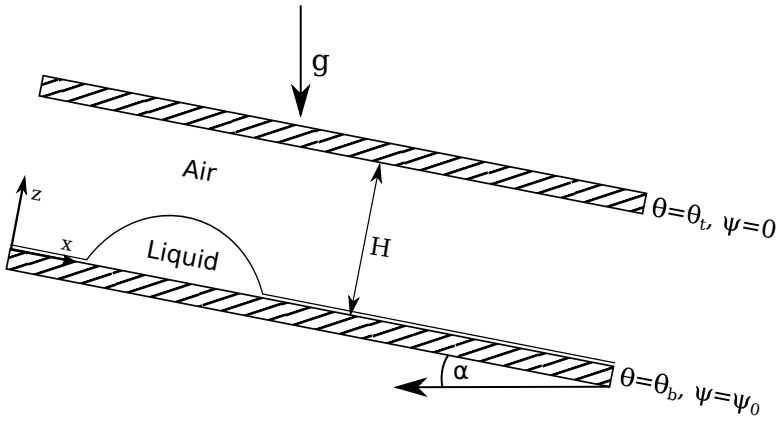

Figure 3.1: Schematic of droplet spreading down an inclined plane

to manipulate droplets on horizontal substrates. Additionally, our work differs significantly from previous studies of electrohydrodynamic effects on gravity-driven thin-film flows since we consider flows that contain apparent contact lines.

The paper is organized as follows. In section 3.1, we describe our mathematical model and numerical solution method. In section 3.2, we use the perfect dielectric model to examine the spreading of non-conducting liquids, and in section 3.3 we use the leaky dielectric model to examine the spreading of weakly conducting liquids. In section 3.4, we examine how an applied temperature gradient and the resulting thermocapillary forces interact with electrostatic forces to influence droplet behavior. Only perfectly wetting liquids are considered in sections 3.2-3.4. In section 3.5, we revisit the results from sections 3.2-3.4 to account for partial wetting. Finally, in section 3.6, we summarize our results and make some concluding remarks.

3.1 Mathematical Model

We consider the case of a droplet spreading on an inclined substrate under the force of gravity in the presence of electric and temperature fields (Figure 1). The substrate is inclined at an angle α; the x-axis is oriented along and the z-axis perpendicular to the substrate. The droplet is assumed to be two-dimensional so that variations in the spanwise direction are neglected. An electrode is suspended above and parallel to the

substrate at a height H. An electrostatic potential of magnitude ψ_0 is applied at the substrate and the top electrode is grounded. We also assume the substrate is held at constant temperature θ_b and the top electrode at θ_t. The liquid, layer 1, has viscosity η, density ρ, surface tension γ, dielectric constant ε, and electrical conductivity σ. We assume the air (layer 2) above the liquid has negligible density and viscosity and thus is of uniform pressure.

We use the parallel electrode configuration shown in Figure 3.1 for several reasons. Although the electrodes need not be parallel in general, the parallel configuration considered here provides a good starting point for building physical understanding. In addition, by assuming H is small in comparison to the horizontal length scale (taken to be the initial droplet width L in section 3.1.3), the lubrication approximation can be invoked. This allows derivation of evolution equations for interfacial height and charge, which can be solved numerically at a relatively modest cost. The parallel electrode configuration can also be realized relatively easily in the laboratory, which we expect will help motivate complementary experimental work in future studies.

3.1.1 Governing Equations

The electric field is given by

$$\mathbf{E}_i = -\nabla\psi_i, \tag{3.1}$$

where ψ is the potential and the subscript i refers to variables in layer i. The potential in each layer is governed by the Laplace equation

$$\nabla^2\psi_i = 0, \tag{3.2}$$

and the boundary conditions

$$\psi_1(z=0) = \psi_0, \tag{3.3}$$

$$\psi_2(z=H) = 0, \tag{3.4}$$

$$\psi_1(z=h) = \psi_2(z=h), \tag{3.5}$$

where $h = h(x,t)$ represents the position of the liquid-air interface. Equations (3.3) and (3.4) set the magnitude of the potential difference between the electrodes, while equation

(3.5) stipulates that the potential is continuous at the liquid-air interface. The equation for interfacial charge results from a balance of the normal component of the electric field at the interface [28],

$$q = \parallel \varepsilon_i \varepsilon_0 \mathbf{E}_i \parallel \cdot \mathbf{n}. \tag{3.6}$$

In equation (3.6), $\parallel f_i \parallel = f_2 - f_1$ for some quantity f_i in layer i, ε_0 is the permittivity of free space, and $\mathbf{n}$ is a vector normal to the interface $h(x,t)$ and pointing into layer 2. Because we are interested in liquid-air systems, we set $\varepsilon_1 = \varepsilon$ and $\varepsilon_2 = 1$.

There are two common models for describing the flow of non-conducting and weakly-conducting fluids: the perfect dielectric model and the leaky dielectric model [28]. In the perfect dielectric model, the conductivity of the fluid is assumed to be zero and thus charge does not flow through the fluid at all. In the leaky dielectric model, the conductivity is nonzero. Assuming in our case that the air layer has zero conductivity and the liquid non-zero conductivity, charge will accumulate at the interface as long as the electric field is present. Ion concentrations in the bulk liquid are assumed to be negligible.

We track the evolution of charge at the interface with the charge conservation equation

$$\frac{\partial q}{\partial t} = q\mathbf{n} \cdot (\mathbf{n} \cdot \nabla)\, \mathbf{v} - \mathbf{v} \cdot \nabla_S\, q + \sigma \mathbf{E}_1 \cdot \mathbf{n} + D_S \nabla_S^2 q, \tag{3.7}$$

where $\mathbf{v}$ is the velocity vector and ∇_S is the surface-gradient operator [28]. The last term is an artificial surface-diffusion term for charge that we found necessary to include for computational purposes; D_S is the surface-charge diffusion coefficient. The stress due to the electric field in each layer is governed by the Maxwell electrical stress tensor, defined as

$$\mathbf{M}_i = \varepsilon_i \varepsilon_0 \left[\mathbf{E}_i \mathbf{E}_i - \tfrac{1}{2} (\mathbf{E}_i \cdot \mathbf{E}_i) \mathbf{I} \right], \tag{3.8}$$

with $\mathbf{I}$ being the identity tensor.

To model the temperature field θ, we apply the energy conservation equation in both layers,

$$\rho_i c_i \frac{D\theta_i}{Dt} = k_i \nabla^2 \theta_i, \tag{3.9}$$

with ρ_i, c_i, and k_i denoting the density, specific heat, and thermal conductivity of layer i, respectively. Consistent with earlier studies using similar geometries [12, 53, 83], we

have assumed that the effects of thermal convection are negligible, so the boundary conditions are

$$\theta_1(z=0) = \theta_b, \tag{3.10}$$

$$\theta_2(z=H) = \theta_t, \tag{3.11}$$

$$\theta_1(z=h) = \theta_2(z=h), \tag{3.12}$$

$$|k_i \nabla \theta_i| \cdot \mathbf{n} = 0 \text{ at } z=h. \tag{3.13}$$

It is assumed that the liquid surface tension decreases linearly with temperature so that $\gamma(\theta) = \gamma_R + \gamma_\theta(\theta - \theta_R)$, where γ_R is reference surface tension at temperature θ_R, and γ_θ is the derivative of γ with respect to θ.

We use the Navier-Stokes equations to describe the liquid flow,

$$\nabla \cdot \mathbf{v} = 0, \tag{3.14}$$

$$\rho \frac{Dv_x}{Dt} = -\frac{\partial p}{\partial x} + \eta \nabla^2 v_x + \rho g \sin\alpha, \tag{3.15}$$

$$\rho \frac{Dv_z}{Dt} = -\frac{\partial p}{\partial z} + \eta \nabla^2 v_z - \rho g \cos\alpha, \tag{3.16}$$

where g is the magnitude of the gravitational acceleration, v_x and v_z are the horizontal and vertical components of velocity, respectively, and p represents the pressure.

From the normal stress balance, we have at $z = h$

$$\| \mathbf{n} \cdot \mathbf{T} \cdot \mathbf{n} \| = \Pi - \kappa\gamma, \tag{3.17}$$

where

$$\mathbf{T} = -p\,\mathbf{I} + \eta \left[\nabla \mathbf{v} + (\nabla \mathbf{v})^T \right] + \mathbf{M}. \tag{3.18}$$

Here, Π is a disjoining pressure discussed in section 3.1.2, and κ is the mean curvature. The tangential stress balance stipulates that at $z = h$,

$$\| \mathbf{n} \cdot \mathbf{T} \cdot \mathbf{t} \| = -\nabla_S \gamma \cdot \mathbf{t}, \tag{3.19}$$

with $\mathbf{t}$ being a vector tangent to the interface.

We also impose the no-slip and no-penetration conditions at the substrate $z = 0$,

$$\mathbf{v}(z = 0) = 0. \tag{3.20}$$

The interface position is governed by the kinematic condition

$$\frac{\partial h}{\partial t} = v_z(z = h) - \frac{\partial h}{\partial x} v_x(z = h). \tag{3.21}$$

3.1.2 Contact-Line Model

By imposing the no-slip condition and thus immobilizing the liquid in contact with the solid surface, the advancing and receding contact lines are also fixed in place. In order to resolve this issue, we follow a number of earlier studies [21, 15, 84, 25, 16] and assume the presence of a thin precursor film of thickness h_c along the entire substrate. The contact line then becomes an *apparent* contact line, which allows us to apply the no-slip condition without restricting the spreading of the droplet. Previous studies have shown that inclusion of a precursor film in spreading simulations leads to results that are qualitatively independent of h_c [21], although the exact spreading rate is a weak function of h_c.

By assuming the presence of a precursor film, we have created conditions where the liquid-solid system becomes perfectly wetting. Thus, given infinite time and an infinite domain, the droplet would spread into a perfectly flat film. The inclusion of the disjoining pressure Π in the normal stress balance allows us to investigate partially wetting systems. We use a form for Π that has been used for droplets on both horizontal [85] and inclined surfaces [84, 16],

$$\Pi = \frac{C}{h_c^n} \left[\left(\frac{h_c}{h} \right)^n - \left(\frac{h_c}{h} \right)^m \right]. \tag{3.22}$$

In equation (3.22), n and m are integers such that $n > m > 1$, and C is a positive constant that determines the wetting properties. Here, $C = 0$ corresponds to a perfectly wetting system while larger values of C correspond to partially wetting systems. In the lubrication limit, it can be shown that C is related to the equilibrium contact angle θ_e

by the expression [16]

$$C = h_c^{n-1} \frac{(n-1)(m-1)}{2(n-m)} \gamma \theta_e^2. \tag{3.23}$$

A discussion of several possible values for n and m can be found in Ref. [85], and for computational convenience we have used the values $(n, m) = (3, 2)$.

3.1.3 Scalings, Lubrication Approximation, and Solution Method

We non-dimensionalize variables as follows,

$$\begin{aligned} (v_x, v_z) &= (U\bar{v_x}, W\bar{v_z}), \quad p = P\bar{p}, \quad q = Q\bar{q}, \\ (x, z) &= (L\bar{x}, H\bar{z}), \qquad t = T\bar{t}, \end{aligned}$$

where variables with the overbar are dimensionless.

From the continuity equation, the vertical velocity scales as $W = H\,U/L$. The time scale is defined as $T = L/U$. Based on the x-component of the momentum conservation equations, we choose to scale pressure by $P = L\rho g \sin\alpha$ and the horizontal velocity by $U = H^2 \rho g \sin\alpha/\eta$. The horizontal length scale L will be the initial droplet length.

Three dimensionless groups come out of the normal stress balance: the rescaled capillary number $Ca = (L^3/H^3)\eta U/\gamma = L^3 \rho g \sin\alpha/(H\gamma)$, the dimensionless electric field strength or Coulomb number $Co = \varepsilon_0 \psi_0^2/(H^2 L \rho g \sin\alpha)$, and a dimensionless Hamaker constant $A = Ca^{-1}(L^2/H^2)\theta_e^2$. The Marangoni number $M = (\theta_b - \theta_t) H \gamma_\theta/(\varepsilon_0 \psi_0^2)$ comes from the tangential stress balance, where γ_θ is the derivative of surface tension with respect to temperature. The charge scale comes from the charge boundary condition (3.6) and is $Q = \varepsilon_0 \psi_0/H$. From the charge conservation equation, we get the dimensionless conductivity $\bar{\sigma} = \sigma L \eta/(\varepsilon_0 H^2 \rho g \sin\alpha)$ and Peclet number for surface charge $Pe = UL/D_S$.

After non-dimensionalization, we apply the lubrication approximation, expanding each equation in terms of $H/L \ll 1$ and keeping only the leading-order terms. We solve for the potential, temperature, and velocity in terms of z, $h(x,t)$, and $q(x,t)$ (now dropping the overbars for dimensionless terms). We can then express the kinematic

condition (3.21) and charge conservation equation (3.7) as

$$\frac{\partial h}{\partial t} = f_1(h(x,t), q(x,t)), \tag{3.24}$$

$$\frac{\partial q}{\partial t} = f_2(h(x,t), q(x,t)), \tag{3.25}$$

where f_1 and f_2 are extremely lengthy and thus are given in the appendix. Gravity in the z-direction has been neglected in equations (3.24) and (3.25). After non-dimensionalization, the z-component of gravity is of order $(H/L)\cot\alpha$. As long as $(L/H) \gg \cot\alpha$, this term can safely be neglected under conditions where lubrication theory is valid.

The initial condition we use for the height is given by

$$h(x, t=0) = \begin{cases} h_c \,\forall\, x \in [0, 0.5) \\ a\cos(2\pi x) + a + h_c \,\forall\, x \in [0.5, 1.5) \\ h_c \,\forall\, x \in [1.5, x_{max}] \end{cases} .$$

This choice ensures that the droplet begins near the left side of the domain while minimizing edge effects. Values of $(h_c, a, x_{max}) = (0.01, 0.25, 5)$ are typically selected resulting in the top of the droplet being halfway between the top and bottom surfaces. Changing the initial volume does not qualitatively change the behavior reported later in the paper. The value of h_c chosen is consistent with those used in prior studies [23, 24].

For boundary conditions, we stipulate that the odd spatial derivatives of $h(x,t)$ are equal to zero at each end of the domain. We use several initial conditions for charge, each of which is discussed in section 3.3. For boundary conditions on $q(x,t)$, we stipulate that the first spatial derivative vanishes at each end of the domain.

Equations (3.24) and (3.25) are discretized using a fourth-order-accurate centered finite-difference scheme, and the library DDASPK3.1 is used for time integration. DDASPK3.1 solves equations of the form $F(t, \mathbf{y}(t), \mathbf{y}'(t)) = 0$ with a modified version of Newton's method [86]. To enable the use of a banded solver, we use an interlaced vector of the form $\mathbf{y}(t) = (h_1, q_1, h_2, q_2, ..., h_N, q_N)$ where N is the number of nodes. To obtain numerical convergence, 1200 nodes per unit length were usually required.

3.2 Results - Perfect Dielectric

We begin by examining the spreading of perfect dielectric droplets, i.e., $q(x,t) = 0$ and $\sigma = 0$. This eliminates charge from the equations, and the only way in which the electric field interacts with the liquid is through an additional term in the equation for pressure (which comes from the normal stress balance (3.17))

$$p = -Ca^{-1}\frac{\partial^2 h}{\partial x^2} + \frac{Co}{2}\frac{\varepsilon(1-\varepsilon)}{(h(\varepsilon-1)-\varepsilon)^2} - \Pi. \tag{3.26}$$

The pressure thus has contributions from the capillary pressure, electrostatic pressure, and disjoining pressure. The electrostatic pressure results from the difference in polarizabilities of the liquid and air layers. If $\varepsilon = 1$, then there is no difference in polarizabilities and thus no net normal force at the liquid-air interface. For the remainder of this paper, we set $\varepsilon = 2.5$, which is consistent with the values for many organic solvents and polymers.

For now we also assume the liquid is perfectly wetting ($\Pi = 0$) and there is no temperature gradient. Thus, the parameter of most interest is the dimensionless electric field strength, Co, which depends on properties such as α, ρ, the dimensions of the droplet, and ψ_0. We set $\alpha = 45^o$, $\rho = 1000\,\mathrm{kg}\cdot\mathrm{m}^{-3}$, $L = 10^{-3}$ m, and $H = 0.1L$. In electrospray, the potential difference is $\sim 1 - 15$ kV [87, 88, 89] and in electrohydrodynamic jet printing the potential difference is ~ 10 V [61]. Taking $\psi \sim 10^2$ V and $H \sim 1$ cm yields comparable electric field strengths to those that occur in electrospray coating [90]. These parameter values correspond to $Co \sim 10^{-1}$, which is within the range explored in this paper. Consistent with previous studies on gravity-driven flow of droplets down inclined planes [15, 91], we set $Ca = 1000$. For this large value of Ca, gravity and viscosity are the dominant forces away from the droplet front, with surface tension becoming important very close to the front.

Shown in Figure 3.2(a) is the interface shape at a relatively early time for a droplet spreading down an inclined plane with no electric field and various values of Co. It is clear that increasing the electric field strength (Co) increases the height of the capillary ridge (Increasing the value of ε at fixed Co would have a similar effect.) In addition, the growth a secondary ridge behind the primary capillary ridge can be observed as Co increases. From equation (3.26) we see that in a perfect dielectric liquid, the electrostatic pressure

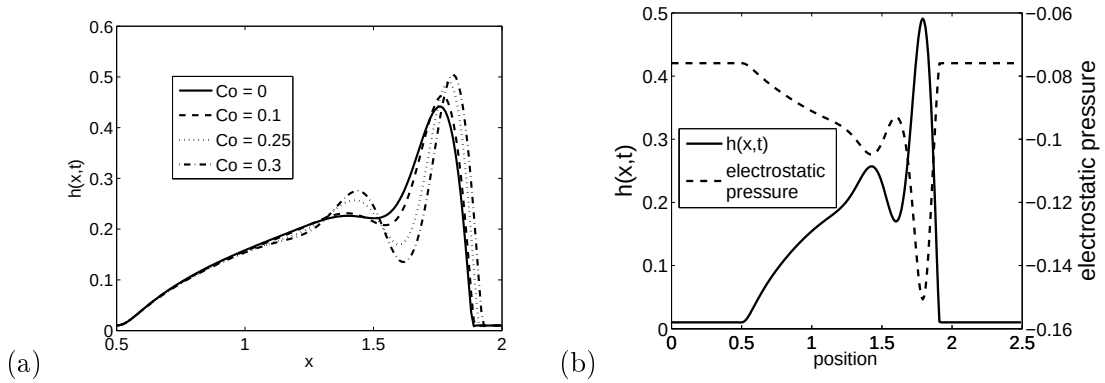

Figure 3.2: (a) Droplet height profiles for perfect dielectrics at $t = 12$. (b) Electrostatic pressure profile overlaid with droplet height profile at $t = 12$ for $Co = 0.25$. Values of other parameters are $Ca = 1000$, $h_c = 0.01$, and $\varepsilon = 2.5$.

is negative as long as $\varepsilon > 1$ (as is the case for most oils and aqueous solutions). In Figure 3.2(b) we see that the electrostatic pressure reaches its minimum where the liquid-air interface reaches its maximum: the capillary ridge. Thus, the electric field drives liquid into the ridge causing an increase in its height, a process which is opposed by capillary pressure and the overall thinning of the droplet as it moves down the substrate.

The height of the capillary ridge as a function of time is shown Figure 3.3 for several values of Co. We again see that the capillary ridge becomes taller as Co is increased, but eventually decays as $t^{-1/3}$ as predicted in Ref. [3]. An interesting feature of Figure 3.3 is the local maximum that is clearly seen in the curve for $Co = 0.25$. This occurs due to the merging of the capillary ridge with the secondary ridge immediately behind it (examples of the ridges can be seen in Fig. 3.2). When the electric field is strong enough, the growth of the adjacent ridges generates high curvature between them. Capillarity causes the ridges to coalesce, which leads to the local maximum in capillary ridge height. After this anomalous behavior, the ridge height eventually decays at the rate of $t^{-1/3}$. Thus, although the electric field increases the height of the capillary ridge and modifies the spreading behavior at short times, the long-time thinning rate of the droplet is unaffected. We also note that at long times, the curves for non-zero Co approach the curve for $Co = 0$.

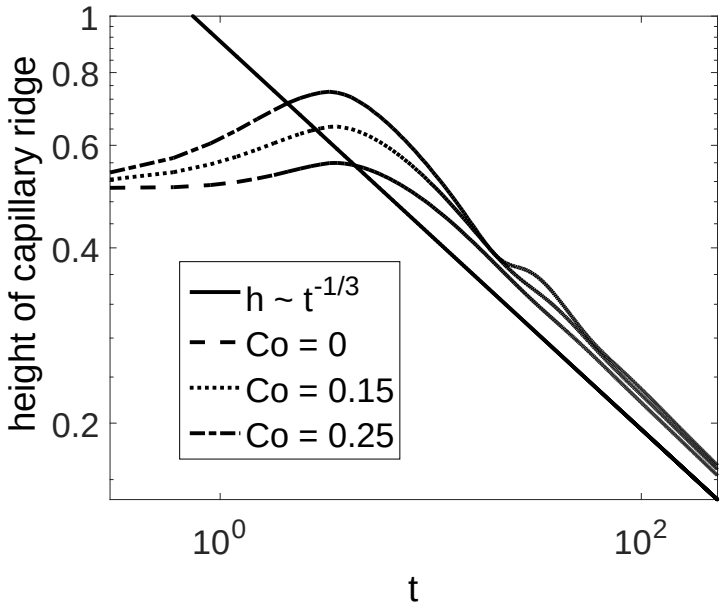

Figure 3.3: Capillary ridge height as a function of time for various Co. The solid line represents a decay rate of $t^{-1/3}$, with a prefactor chosen to offset it from the other curves for clarity. Values of other parameters are $Ca = 1000$, $h_c = 0.01$, and $\varepsilon = 2.5$.

3.3 Results - Leaky Dielectric

We now consider leaky dielectric liquids, for which $\sigma > 0$. In the current section, we consider only perfectly wetting liquids with no temperature gradient. The electric field still creates an electrostatic pressure, however this pressure now depends on the surface charge q as well as the interface height h. As a consequence of surface charge, the interfacial shear stress will no longer be zero (equation (3.19)). Instead, charge accumulates at the interface and produces a shear stress equal to

$$\left.\frac{\partial v_x}{\partial z}\right|_{z=h} = -Co\, q\, \frac{\partial \psi(z=h)}{\partial x}. \tag{3.27}$$

After applying the lubrication approximation, the charge conservation equation (3.7) becomes

$$\frac{\partial q}{\partial t} = -\frac{\partial}{\partial x}\left(q v_x(z=h)\right) - \sigma \left.\frac{\partial \psi_1}{\partial z}\right|_{z=h} + \frac{1}{Pe}\frac{\partial^2 q}{\partial x^2}. \tag{3.28}$$

This equation is the same as that given by Saville [28] except for the diffusion term on the right-hand side, which is usually neglected. We retain it here in to resolve steep gradients in charge that form at the advancing contact line.

In Figure 3.4, we show interface shapes for a typical set of parameter values and different values of Pe. For $Pe > 1000$, the interface shapes are only very weakly dependent on Pe. We thus use the value of $Pe = 1000$ in the rest of the calculations. Below, we first consider the case of zero conductivity, followed by the case of non-zero conductivity.

3.3.1 Zero conductivity

To isolate the influence of surface charge, we first consider the case where the conductivity σ is zero. This situation may arise when a non-conducting droplet is either charged during its formation (e.g., electrospray) or if a flying droplet collides with charged particles that adsorb to its surface. No additional charge will accumulate at the surface because the liquid conductivity is zero, however the existing charge will contribute a shear stress as shown in equation (3.27). To simulate this case, we used an initial condition for charge ($q_0(x) = 0.1\, h_0(x)$) which prescribes a maximum charge concentration centered on the droplet with a smaller, constant concentration on the precursor film.

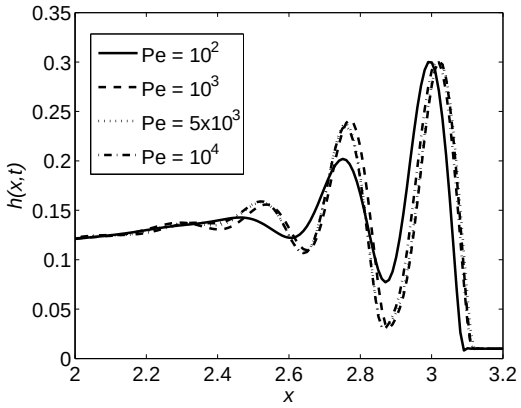

Figure 3.4: Effect of Pe on droplet height profiles at $t = 89.1$. Values of other parameters are $Ca = 1000$, $h_c = 0.01$, $\varepsilon = 2.5$, $Co = 0.25$, and $\sigma = 0.01$.

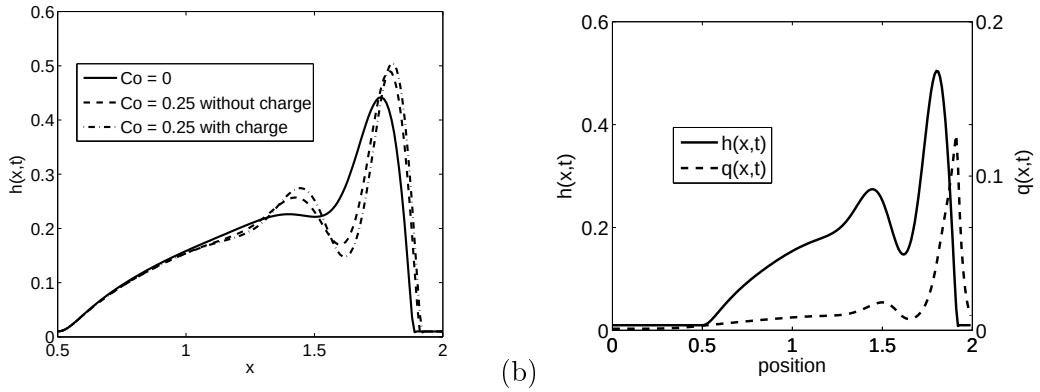

(a) (b)

Figure 3.5: (a) Droplet height profiles for non-conducting droplets with and without surface charge at $t = 11.7$ (The latter case corresponds to a perfect dielectric.) (b) Surface charge distribution near the front superimposed on droplet height profile at $t = 11.7$ for $Co = 0.25$. Values of other parameters are $Ca = 1000$, $h_c = 0.01$, $\varepsilon = 2.5$, $\sigma = 0$, and $Pe = 1000$.

For this case, Figure 3.5(a) shows that the presence of interfacial charge increases the height of the capillary ridge and deepens the valley immediately behind it (These effects would be enhanced as the magnitude of q_0 increases.) Figure 3.5(b) shows that early on, the charge redistributes to form a maximum near the location of the advancing contact line. For the results shown in Figure 3.5 we used an initial charge distribution proportional to the droplet shape, but other initial conditions such as constant charge along the domain also show a maximum concentration quickly developing at the advancing contact line.

A close inspection of the contact-line region (Figure 3.5(b)) shows that this charge is most concentrated on the leading face of the capillary ridge. This, in conjunction with the rapid change of potential along that face, creates a shear stress that pumps liquid up the capillary ridge. The degree to which the capillary ridge is heightened by the shear stress is limited by the fact that the liquid's lack of conduction allows no additional charge to accumulate. The effect of small amounts of charge on non-conducting droplets is thus a marginal increase in capillary-ridge height. This is not guaranteed to be the case when the conductivity is non-zero, in which case charge will constantly be accumulating at the liquid-air interface.

3.3.2 Non-zero conductivity

We now turn to the case where the conductivity σ is non-zero. As pointed out earlier, surface charge will accumulate along the entire liquid-air interface as the droplet moves down the substrate. Shown in Figure 3.6(a) are height and charge profiles for a leaky dielectric droplet that has spread some distance down the substrate. Perhaps the most glaring difference from previous cases is the growth of the minor ridges behind the primary capillary ridge. In the absence of an electric field (and also in the zero-conductivity case considered earlier), these ridges are difficult to observe past the secondary one.

However, as can be inferred from the charge profile in Figure 3.6(a), the minor ridges will grow when charge-induced shear stresses are present. In fact, some of the fluctuations in ridge height visible in Figure 3.6(b) represent the secondary or tertiary ridges overtaking the capillary ridge in height. This behavior differs markedly from any that has been predicted when charge has been absent (Figure 3.2) or present in only small amounts (Figure 3.5). This behavior would be enhanced for larger values of the

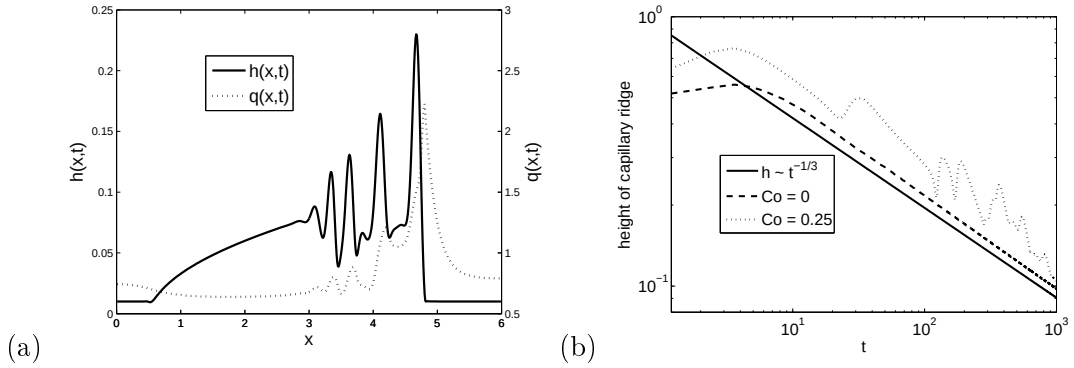

Figure 3.6: (a) Height and surface charge profiles of a leaky dielectric droplet with no initial charge flowing down an inclined plane at $t = 380.8$ for $Co = 0.25$. (b) Capillary ridge height as function of time. The solid line represents a decay rate of $t^{-1/3}$, with a prefactor chosen to offset it from the other curves for clarity. Values of other parameters are $Ca = 1000$, $h_c = 0.01$, $\varepsilon = 2.5$, $\sigma = 0.01$, and $Pe = 1000$.

conductivity σ.

In the cases discussed so far, although the electric field enlarges the capillary ridge, the droplet eventually settles into a long-time regime with the ridge height decaying as $t^{-1/3}$. We see in Figure 3.6(b) that in leaky dielectric droplets, this regime may in some cases never be reached (although the fluctuations in capillary ridge height decrease in magnitude, minor ridges in the droplet continue to grow). This is due to the repeated growth and coalescence of the primary and minor capillary ridges, where the growth results from charge-induced shear stresses and the coalescence results from capillary pressure.

This behavior was not observed in the zero-conductivity case. In that case, the primary ridge accumulated charge by depleting the regions around it. With only trace amounts of charge on the minor ridges, shear stresses did not become strong enough to cause their growth. In contrast, the nonzero conductivity of leaky dielectric droplets causes charge to accumulate across the entire droplet surface, as seen in Figure 3.6(a).

We find that when the conductivity is zero (Figure 3.5), the height of the capillary ridge is increased relative to the case when there is no charge at all. The secondary ridge is also amplified slightly, but other minor ridges are unnoticeably small. However when the conductivity is non-zero, there is significantly more charge buildup at the

leading faces of each ridge and subsequent growth in the height of even the minor ridges (Figure 3.6(a)). This mechanism is similar to that responsible for the instability seen in electrohydrodynamic patterning [7, 46, 47, 8, 92, 9, 83, 93]. The growth and coalescence of the minor ridges can eventually lead to the interior ridges overtaking the primary ridge as the tallest in the droplet. Although taller capillary ridges are generally expected to destabilize the front of a spreading liquid film [21, 23, 24, 84], further study is required to definitively learn how surface charge affects the lateral stability of two-dimensional droplets.

3.4 Results - Thermocapillary effects

A temperature gradient at a fluid interface can cause a gradient in surface tension, in turn generating tangential stresses which are known as Marangoni stresses. These Marangoni stresses are of great importance as a means of understanding and controlling thin-film flows. Thermocapillary stresses are Marangoni stresses arising from temperature gradients, and are of interest as a method for droplet actuation, which is of importance in microelectromechanical and microfluidic devices [94, 95]. Brzoska and co-workers [96] investigated through both modeling and experiments the use of a lateral (parallel to the flow) temperature gradient to induce motion of droplets on horizontal substrates. Since then, other studies on thermocapillary spreading have included effects such as contact-angle hysteresis [97], and spreading up vertical walls [98, 19] and down inclined planes [99]. Several papers [100, 101, 102, 103] have examined gravity-driven spreading down a locally heated surface and although both are present, these focus more on evaporative rather than thermocapillary effects.

In this section, we investigate the gravity-driven spreading of a liquid droplet on a constant-temperature, inclined substrate that is subject to an electric field. Our work is distinguished from previous studies in that there is no temperature difference on the substrate in the direction of flow, i.e. we isolate the effects of the normal temperature gradient. Additionally, we investigate the possibility of using a temperature gradient to counteract the effects of an electric field. We assume evaporation is negligible in order to focus solely on the interplay of thermocapillary and electrohydrodynamic effects.

We non-dimensionalize temperature by $\bar{\theta} = (\theta - \theta_t)/(\theta_b - \theta_t)$ and define the ratio of

the thermal conductivities as $\kappa = k_2/k_1$. The Marangoni force appears in the tangential stress balance, modifying equation (3.27) to the dimensionless form

$$\left.\frac{\partial v_x}{\partial z}\right|_{z=h} = -Co\,q\frac{\partial \psi(z=h)}{\partial x} - M\frac{\partial \theta(z=h)}{\partial x}. \tag{3.29}$$

With regard to temperature gradients, there are two general configurations that are of interest: (a) films heated from below ($M > 0$) and (b) films cooled from below ($M < 0$). In case (a), the liquid closest to the substrate will have a higher temperature and thus regions of the liquid-air interface close to the substrate will have lower surface tension than the liquid near the peak of the capillary ridge (as well as the peaks of the secondary ridges). Thus one would expect flow toward the peaks to be promoted, leading to a higher capillary ridge than would otherwise be observed. Indeed we found this to be the case in our simulations. In case (b), when the liquid is cooled from below, flow toward the peaks will be inhibited and a smaller capillary ridge is expected. It is this second case that is especially interesting in gravity-driven droplet spreading. The ability to use a temperature gradient to suppress the growth of the capillary ridge could be a simple yet powerful means of stabilizing the film front against the formation of rivulets and streaks. We thus consider below the case $M < 0$.

Figure 3.7 shows droplet height profiles and the time-evolution of the capillary ridge height for different values of $M \leq 0$ for both perfect and leaky dielectric droplets. We find that as the Marangoni number declines to greater and greater negative values, the capillary ridge can be suppressed almost entirely (Figures 3.7(a) and (c)). For leaky dielectric droplets, the minor ridges behind the primary capillary ridge are also suppressed (Figure 3.7(c)).

The capillary ridge reaches its greatest height at the very beginning of spreading. In Figures 3.7(b) and (d), we see that the initial rise in capillary ridge height is virtually eliminated when $M = -0.3$. If we assume that the surface tension of most common liquids has a temperature dependence of approximately $d\gamma/d\theta \sim -0.1\,\mathrm{mN/m \cdot K}$ [104], then for a droplet with thickness $H = 10^{-3}$ m, a temperature difference of roughly 50°C would be required to achieve this Marangoni number. Analysis of the results in figures 3.7(b) and (d) also reveals that the capillary ridge height decays as $t^{-1/3}$, with the curves becoming increasingly offset as M increases in magnitude.

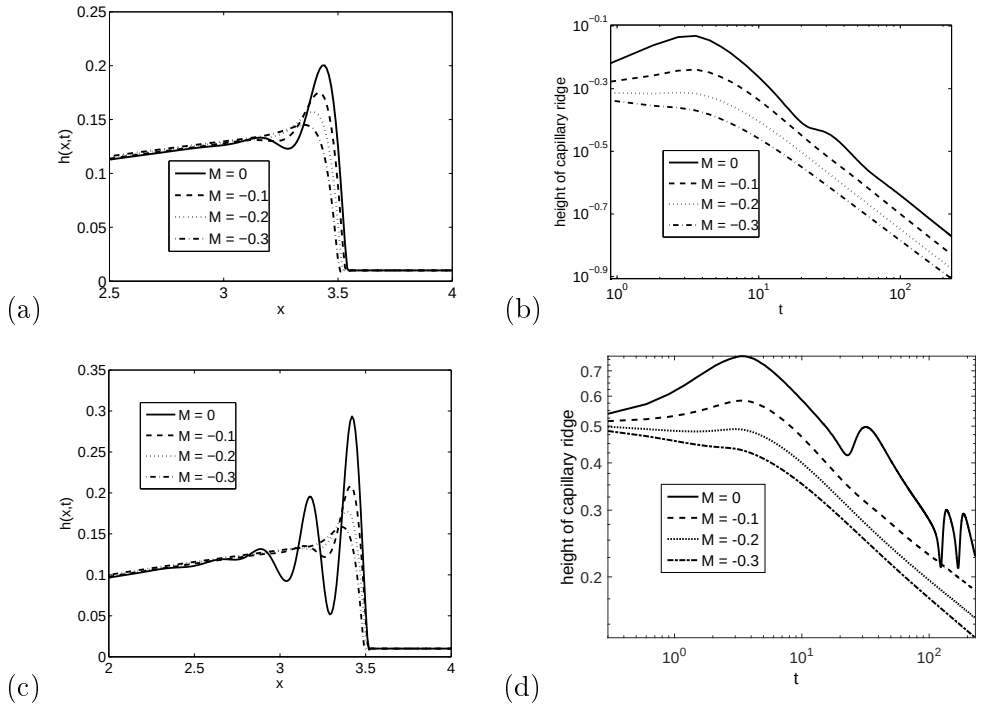

Figure 3.7: (a) Droplet height profiles for perfect dielectric droplets ($\sigma = 0$) spreading down an inclined plane with and without thermocapillary effects at $t = 144$. (b) Capillary ridge height for perfect dielectric droplets as a function of time for various values of M. (c) Same as (a) but for leaky dielectric droplets ($\sigma = 0.01$) at $t = 144$. (d) Same as (b) but for leaky dielectric droplets. Values of other parameters are $Ca = 1000$, $h_c = 0.01$, $\varepsilon = 2.5$, $Co = 0.25$, and $\kappa = 0.2$.

Due to the suppression of the capillary ridge growth, the rest of the interface profile is also affected by the Marangoni forces. With tangential stresses pulling liquid down from the peak, the ridge is forced into a shorter, blunted shape, shown in Figures 3.7(a) and (c) for various values of M. Interestingly, the Marangoni number does not appear to have any effect on the width of the ridge, or as seen in Figures 3.7(b) and (d), the rate at which the droplet thins ($\sim t^{-1/3}$ for long times). We note that all of the effects shown in Figure 3.7 would be enhanced for larger values of the conductivity ratio κ. The results in the absence of an electric field ($Co = 0$) are qualitatively similar to those shown in Figures 3.7(a) and (b) so we do not present them here.

The results of this section show that thermocapillary forces can be used to modify the shape of a droplet flowing down an inclined plane. They differ from previous studies [100, 101, 102, 103] in that the temperature gradient is imposed along the entire substrate (as opposed to localized heating) and in the presence of an electric field. We find that by heating the liquid from above and cooling from below, the growth of the capillary ridge is inhibited. Due to the fact that the capillary ridge is responsible for the fingering instability in gravity-driven flow, the application of a temperature gradient could be a means of suppressing this instability.

3.5 Results - Partially Wetting Liquids

Thus far, all of the results concern liquids that perfectly wet the solid substrate. In this section, we consider the spreading of partially wetting liquids down an inclined plane in the presence of an electric field. A brief discussion of our contact-line model and some relevant references are provided in section 3.1.2. In dimensionless form, equation (3.22) becomes

$$\Pi = A\,\frac{(n-1)(m-1)}{2h_c(n-m)}\left[\left(\frac{h_c}{h}\right)^n - \left(\frac{h_c}{h}\right)^m\right], \tag{3.30}$$

where $A = (\gamma\theta_e^2)/(H\,L\,\rho g\sin\alpha)$.

For partially wetting liquids spreading down a vertical substrate, Eres et al.[84] found that raising the equilibrium contact angle results in a higher capillary ridge. In Figure 3.8(a), we find this holds true for the spreading of perfect dielectric droplets in the presence of an electric field (compare $A = 0.02$ case with $A = 0$ case when $Co = 0.25$). Additionally, we begin to see movement of the receding contact line as the

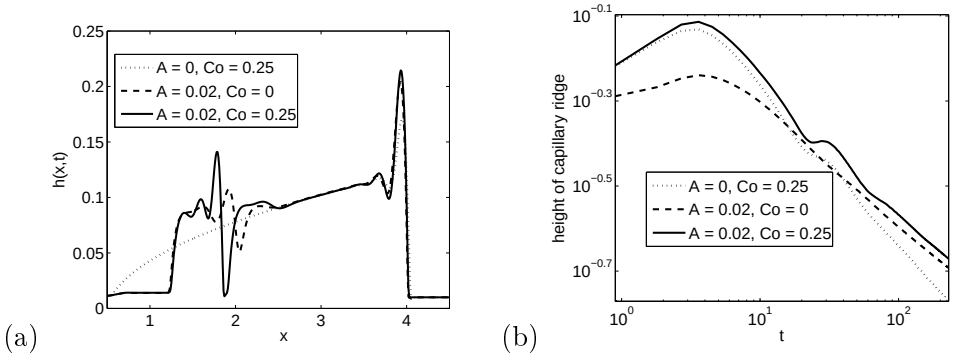

Figure 3.8: (a) Droplet height profiles for perfect dielectrics at $t = 225$. (b) Capillary ridge height as function of time. Values of other parameters are $Ca = 1000$, $h_c = 0.01$, $\varepsilon = 2.5$, and $M = 0$.

droplet front moves down the substrate (compare $A = 0.02$ cases with $A = 0$ case). In perfectly wetting liquids, the receding contact angle decreases as the droplet spreads out, reducing the thickness in that region. In partially wetting liquids, disjoining pressure becomes significant as the droplet thickness decreases and drives the receding contact line forward.

The presence of an electric field can also promote droplet separation in partially wetting liquids. In the absence of an electric field, daughter droplets can begin to form near the receding edge of the main droplet ($A = 0.02$ and $Co = 0$ case in Figure 3.8(a)). In the presence of an electric field, gradients in electrostatic pressure created by interfacial perturbations exacerbate those perturbations, leading to a deeper minimum in the film thickness ($A = 0.02$ and $Co = 0.25$ case near $x = 2$ in Figure 3.8(a)), which would correspond to an earlier droplet separation. Figure 3.8(b) shows that the long-time thinning rate of the droplet is slower when $A = 0.02$ than when $A = 0$. When $A = 0.02$, disjoining pressure causes the receding contact line to move forward with the droplet, shortening the droplet's length and slowing the decay of its height.

In Figure 3.9, we consider the case of leaky dielectric droplets. Here, minor ridges in the film height are much more pronounced in the case of partial wetting (compare $A = 0.02$ case with $A = 0$ case when $Co = 0.25$ in Figure 3.9(a)). Clearly disjoining pressure plays an even more dramatic role in the spreading of leaky dielectric droplets than it does in perfect dielectric droplets (Figure 3.8). This can be understood by

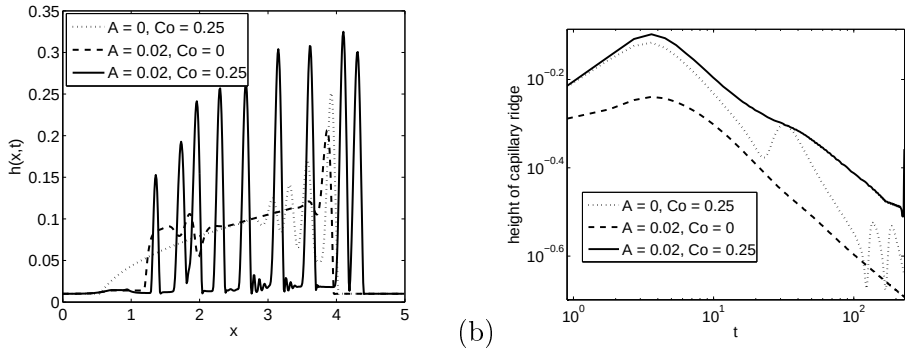

(a) (b)

Figure 3.9: (a) Droplet height profiles for leaky dielectrics at $t = 225$. (b) Capillary ridge height as function of time. Values of other parameters are $Ca = 1000$, $h_c = 0.01$, $\varepsilon = 2.5$, $\sigma = 0.01$, and $M = 0$.

recalling Figure 3.6(a), where it was observed that the minor ridges of leaky dielectric droplets begin to grow in the presence of an electric field. During this growth, the valleys between the ridges can become thin enough for disjoining pressure to be significant. When a valley approaches the thickness of the precursor film, disjoining pressure becomes large and drives liquid into the ridges on each adjacent side of the valley. This has the effect of separating the main droplet into a series of smaller droplets.

Figure 3.9(b) shows that, as is the case with perfect dielectrics, the long-time thinning rate of the droplet is slower in partially wetting liquids (compare $A = 0.02$ case with $A = 0$ case when $Co = 0.25$ in Figure 3.9(b)). Notably, the fluctuations in ridge height that are present in the $A = 0$, $Co = 0.25$ case are mostly absent in $A = 0.02$, $Co = 0.25$ case (except for a sharp rise in ridge height visible at the far right edge of Figure 3.9(b)). In perfectly wetting systems ($A = 0$), capillarity can cause adjacent ridges to coalesce, leading to fluctuations in the ridge height. However, in partially wetting systems ($A = 0.02$), disjoining pressure tends to separate the ridges into discrete droplets and oppose their merging into a single larger ridge.

Finally, we briefly comment on thermocapillary effects, but do not show the results for brevity. As in section 3.4, negative values of the Marangoni number M suppress the height of the capillary ridge, and also suppresses the minor ridges (in the case of leaky dielectrics). The daughter droplets near the receding contact line are also suppressed, even in the absence of an electric field.

3.6 Conclusions

In this work, we have used lubrication theory to understand the fundamentals of gravity-driven spreading of liquid droplets in the presence of an electric field and temperature gradient. We investigated both perfect dielectric and leaky dielectric liquids, and also accounted for perfectly and partially wetting systems. In perfect dielectric liquids, electric fields increase the height of the capillary ridge near the front of the droplet. At high electric fields, the secondary ridge can grow and eventually merge with the capillary ridge before the front settles into a quasi-steady state. In leaky dielectric liquids, high concentrations of charge along the surface of the droplet generate shear stresses that lead to growth of multiple minor ridges and possible splitting of the main droplet. In both perfect and leaky dielectric liquids, partial wetting effects result in movement of the receding contact line and an increase in the height of the capillary ridge. Partial wetting also promotes splitting of daughter droplets from the main droplet. Thermocapillary forces generated from cooling the substrate can be a means of suppressing the growth of the capillary ridge and thus counteract the influence of the electric field.

These results are of interest due to the presence of electric fields in liquid coatings. Voltages are often used in spray coating to disperse the liquid into smaller droplets, possibly creating an electric field through the liquid coating. Our results suggest that high amounts of charge on the liquid surface can cause droplet splitting, which may oppose the formation of a uniform liquid film. Inclusion of disjoining pressure in our model indicates that this problem may be more common in partially wetting liquids than in perfectly wetting liquids. Establishing a temperature gradient through the droplet by cooling from the coated substrate may help to suppress the effects of an electric field.

Several extensions of this work are of interest. First, extending the model to account for additional effects such as three-dimensionality, non-slender droplets, and inertia would generalize the model for comparison to a wider variety of physical situations. The inclusion of electrokinetic effects may also be insightful [105]. Second, complementary experiments should be performed to test the theoretical predictions made here and to possibly reveal phenomena that may not be describable by the present model. Finally, it is worthwhile to examine the stability of the droplet profiles found here to perturbations in the transverse direction. The extent to which electric fields can modify the fingering

instability remains an open issue, one which we look forward to investigating in future work.

Chapter 4

Electrohydrodynamic and thermocapillary stabilization of dynamic contact lines

4.1 Introduction

Thin liquid films with dynamic contact lines driven by body forces arise in many technological applications, ranging from the operation of microfabricated devices [58] to the coating of medical devices [55] and beyond. When a liquid film with a contact line is driven by gravity, a ridge of liquid known as the capillary ridge rises above the film in the upstream region. In these situations, traveling wave solutions for the liquid profile can be calculated which show the quasi-steady shape of the capillary ridge [23, 24, 25]. The capillary ridge has been shown to destabilize the front of the liquid film to disturbances in the spanwise direction which can grow into rivulets or fingers and negatively impact the uniformity of a liquid coating [21, 106]. It is thus of interest to investigate methods for controlling the growth of the capillary ridge and stabilizing the contact line to spanwise disturbances.

Electric fields [107, 108, 109] and temperature gradients [110, 111] can be used to control liquids at small length scales and may be able play a role in stabilizing the contact lines of driven liquid films. Electric fields are already present in gravity-driven flows

which arise in electrospray coating [60] where uniform films are typically desired, and temperature gradients can be used to drive and influence spreading films [98, 101]. Although methods for stabilizing dynamic contact lines could be instrumental in producing more uniform coatings, little is understood about how electric and temperature fields might affect the stability of the film front. Tseluiko *et al.* [80, 81] have shown that electric fields affect capillary ridge growth in gravity-driven film flows over topography where there are no contact lines. Kataoka and Troian [98] observed the fingering instability in thermally-driven films, while Klentzman and Ajaev [101] showed that Marangoni effects can promote the fingering instability in gravity-driven films when heated from below. However, the effects of electric fields or cooling the liquid from below on the spanwise stability of gravity-driven films with contact lines have not been studied.

Here we examine the gravity-driven flow of a constant-flux liquid film in the presence of normal electric and temperature fields. We apply the lubrication approximation and obtain an evolution equation for interface height. We first study electrohydrodynamic (EHD) and thermocapillary (TC) effects on the traveling wave solutions to the height evolution equation. We then conduct a linear stability analysis of the traveling wave solutions and characterize the effects of the electric and temperature fields on the stability of the dynamic contact line. An energy analysis is performed to gain insight into the mechanisms behind the EHD and TC effects on the contact-line instability. Our results demonstrate that electric fields and temperature gradients can be used to suppress the fingering instability in gravity-driven thin-film flows, and could be of use in efforts to generate uniform coatings.

4.2 Problem formulation

We consider a constant flux of liquid being driven down a vertical substrate by gravity (Figure 4.1). An electrode is suspended above and parallel to the substrate at a height H. An electrostatic potential of magnitude Ψ_0 is applied at the substrate while the top electrode is grounded. We assume the substrate and electrode are held at constant temperatures Θ_b and Θ_t, respectively. The parallel configuration of the electrodes provides a good starting point for gaining physical understanding by allowing us to invoke the lubrication approximation when the electrode spacing H is small compared to the

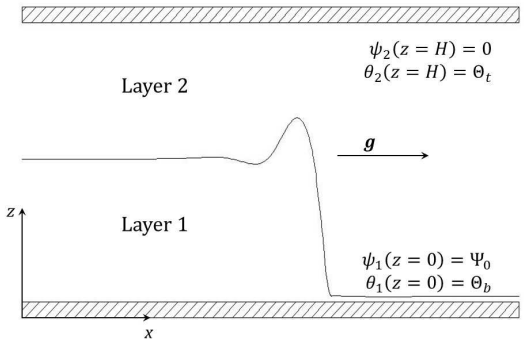

Figure 4.1: Schematic of problem geometry. The x- and z-axes are shown, while the y-axis points into the page. The electrostatic potential and temperature in each layer are denoted by ψ_i and θ_i, respectively.

horizontal length scale L (defined in section 4.2.2). The liquid, layer 1, has viscosity η, density ρ, and surface tension γ. We assume the liquid is a perfect dielectric with dielectric constant ε_1. The air layer above the liquid is denoted as layer 2 and assumed to have small enough viscosity and density such that its flow can be neglected.

4.2.1 Governing equations

We use the Navier-Stokes equations to describe the liquid flow in layer 1,

$$\nabla \cdot \mathbf{v} = 0, \tag{4.1}$$

$$\rho \frac{D\mathbf{v}}{Dt} = -\nabla \cdot \mathbf{T}_1 + \rho g \mathbf{e}_x, \tag{4.2}$$

where g is the constant gravitational acceleration, $\mathbf{v} = (v_x, v_y, v_z)$ is the velocity vector, and $\mathbf{T}_1$ is the total stress tensor of the liquid, defined as

$$\mathbf{T}_1 = -p_1 \mathbf{I} + \frac{1}{2}\eta \left[\nabla \mathbf{v} + (\nabla \mathbf{v})^T\right] + \mathbf{M}_1, \tag{4.3}$$

where $\mathbf{I}$ is the identity tensor, p_1 is the liquid pressure, and $\mathbf{M}_1$ is the Maxwell stress tensor which is defined later in this section. We ignore the flow in the air layer, and thus

the stress tensor in the air is the sum of the pressure and Maxwell stress tensor, given by

$$\mathbf{T}_2 = -p_2\mathbf{I} + \mathbf{M}_2, \tag{4.4}$$

where p_2 is the pressure in the air.

We let $h(x, y, t)$ denote the location of the liquid-air interface, so from the normal stress balance we have at $z = h(x, y, t)$

$$\| \mathbf{n} \cdot \mathbf{T}_i \cdot \mathbf{n} \| = -\kappa\gamma, \tag{4.5}$$

where $\mathbf{n}$ is a vector normal to the interface pointing into layer 2, κ is the mean curvature of the interface, and $\| f_i \| = f_2 - f_1$ for a given function f_i. The tangential stress balances state that at $z = h(x, y, t)$,

$$\| \mathbf{n} \cdot \mathbf{T}_i \cdot \mathbf{t} \| = -\nabla_S\gamma \cdot \mathbf{t}, \tag{4.6}$$

where $\mathbf{t}$ represents two vectors that are tangent to the interface and ∇_S is the surface gradient operator.

We also impose the no-slip and no-penetration conditions at the the substrate,

$$\mathbf{v}(z = 0) = 0. \tag{4.7}$$

The interface position is governed by the kinematic condition

$$\frac{\partial h}{\partial t} = -\nabla \cdot (h\mathbf{v}) . \tag{4.8}$$

The electric field is given by

$$\mathbf{E}_i = -\nabla\psi_i, \tag{4.9}$$

where ψ_i is the electrostatic potential. The potential in each layer is governed by the Laplace equation

$$\nabla^2\psi_i = 0, \tag{4.10}$$

and the boundary conditions

$$\psi_1(z=0) = \Psi_0, \tag{4.11}$$

$$\psi_2(z=H) = 0, \tag{4.12}$$

$$\psi_1(z=h) = \psi_2(z=h). \tag{4.13}$$

We consider only perfect dielectric (i.e., non-conductive) liquids, so the jump in the normal component of the electric field is [28]

$$\parallel \varepsilon_i \varepsilon_0 \mathbf{E}_i \parallel = 0, \tag{4.14}$$

where ε_0 is the permittivity of free space. We set the permittivity of the air layer as $\varepsilon_2 = 1$, and denote the permittivity of the liquid layer as $\varepsilon_1 = \varepsilon$. As noted above, the interaction between the electric field and the fluids is described by the Maxwell stress tensor, defined in each layer i as

$$\mathbf{M}_i = \varepsilon_i \varepsilon_0 \left[\mathbf{E}_i \mathbf{E}_i - \tfrac{1}{2} \left(\mathbf{E}_i \cdot \mathbf{E}_i \right) \mathbf{I} \right]. \tag{4.15}$$

To model the temperature field θ, we apply the energy conservation equation in both layers,

$$\rho_i c_i \frac{D\theta_i}{Dt} = k_i \nabla^2 \theta_i, \tag{4.16}$$

where ρ_i, c_i, and k_i denote the density, specific heat, and thermal conductivity of layer i, respectively. Consistent with earlier studies (on problems without dynamic contact lines) [12, 53, 111] that use similar geometries, we assume that the effects of thermal convection are negligible, so the boundary conditions are

$$\theta_1(z=0) = \Theta_b, \tag{4.17}$$

$$\theta_2(z=H) = \Theta_t, \tag{4.18}$$

$$\theta_1(z=h) = \theta_2(z=h), \tag{4.19}$$

$$\parallel k_i \nabla \theta_i \parallel \cdot \mathbf{n} = 0 \text{ at } z = h. \tag{4.20}$$

It is assumed that the liquid surface tension decreases linearly with temperature so that

$\gamma(\theta) = \gamma_R + \gamma_\theta(\theta - \Theta_R)$, where γ_R is a reference surface tension at temperature Θ_R and θ is the temperature at the interface.

By imposing the no-slip condition and thus immobilizing the liquid in contact with the solid surface, the advancing contact line is also fixed in place. To resolve this issue, we follow a number of earlier studies [21, 15, 84, 25, 16] and assume that a thin precursor film of thickness b is present along the entire substrate. The contact line then becomes an *apparent* contact line, which allows us to apply the no-slip condition without restricting the spreading of the film.

Previous studies have shown that inclusion of a precursor film in models for the spreading of driven films leads to results that are qualitatively independent of b [21], although the exact rate at which the film front moves down the substrate is a function of b. Other methods for resolving the contact-line issue in spreading problems have included a slip condition [23] and numerical slip [14]. Again, all the methods yield results that are qualitatively similar, although the results differ quantitatively depending on the slip model chosen. In this paper we consider only the precursor-film model.

4.2.2 Scalings and lubrication approximation

We non-dimensionalize the variables as follows,

$$\begin{aligned} (v_x, v_y, v_z) = (U\bar{v_x}, U\bar{v_y}, W\bar{v_z}), \quad p_i = P\bar{p}_i, \qquad \psi_i = \Psi_0\bar{\psi}_i, \\ (x, y, z) = (L\bar{x}, L\bar{y}, H\bar{z}), \qquad t = T\bar{t}, \quad \bar{\theta}_i = (\theta_i - \Theta_t)/(\Theta_b - \Theta_t) \end{aligned}$$

where variables with the overbar are dimensionless.

The vertical length scale is chosen to be the electrode spacing H. From the continuity equation, the vertical velocity is scaled by $W = HU/L$. In the kinematic condition, we choose to scale time as $T = 3L/U$. We choose to scale horizontal velocity with $U = H^2\rho g/\eta$, which represents a balance of viscous and gravitational forces in the x-component of the momentum equations. We scale pressure with the gravitational force, $P = L\rho g$. The horizontal length scale L is determined by a balance of surface tension and gravitational forces to be $L = (\gamma H/\rho g)^{1/3}$. A dimensionless electric force parameter arises in the normal stress balance, defined as the Coulomb number $Co = \varepsilon_0\Psi_0^2/(H^2 L\rho g)$. The Marangoni number comes from the tangential stress balances and

is $Ma = \gamma_\theta \Delta\Theta/(HL\rho g)$, with $\Delta\Theta = \Theta_t - \Theta_b$. The ratio of thermal conductivities is denoted by $\kappa = k_1/k_2$.

After non-dimensionalization, we apply the lubrication approximation and expand each equation in terms of $H/L \ll 1$, keeping only the leading-order terms. We solve for the potential, temperature, and velocities in terms of z and $h(x, y, t)$ (now dropping the overbars for dimensionless terms).

4.2.3 Evolution equations

As is customary in previous constant-flux studies, we change coordinate systems to one that moves at a constant speed along with the contact line: $(x, y, z, t) \to (\xi, y, z, t)$, where $\xi = x - Ut$ (we solve for U in the next section). Then, $h \to h(\xi, y, t)$ and $\nabla \to (\frac{\partial}{\partial \xi}, \frac{\partial}{\partial y})$. We solve for $\mathbf{v}$ in terms of h, ψ, and θ using the lubrication forms of the Navier-Stokes equations (4.1) and (4.2) subject to boundary conditions (4.5)-(4.7), then solve for ψ using equations (4.10)-(4.14) and θ using equations (4.16)-(4.20). We can then express the kinematic condition (4.8) as an evolution equation for h:

$$\frac{\partial h}{\partial t} = U\frac{\partial h}{\partial \xi} - \nabla\cdot(h^3\nabla\nabla^2 h) - \frac{\partial h^3}{\partial \xi} + Co\varepsilon(1-\varepsilon)\nabla\cdot(h^3\nabla c_5^2) + \frac{3}{2}Ma\nabla\cdot(h^2\nabla\theta(h)), \quad (4.21)$$

where

$$c_5 = \frac{1}{(h(\varepsilon - 1) - \varepsilon)}, \quad (4.22)$$

and the interfacial temperature is

$$\theta(z = h) = \frac{h\,\kappa}{h(1-\kappa) - 1} + 1. \quad (4.23)$$

4.3 Traveling wave solutions

As noted earlier, previous studies on constant-flux flows with dynamic contact lines have shown that it is possible to solve the height evolution equation to obtain traveling wave solutions that describe the flow prior to any spanwise perturbations [23, 25]. To recover a traveling wave solution to equation (4.21), let us first assume that h is y-independent

and thus simplify equation (4.21) to

$$\frac{\partial h}{\partial t} = U\frac{\partial h}{\partial \xi} - \frac{\partial}{\partial \xi}\left(h^3\frac{\partial^3 h}{\partial \xi^3}\right) - \frac{\partial h^3}{\partial \xi} + Co\varepsilon(1-\varepsilon)\frac{\partial}{\partial \xi}\left(h^3\frac{\partial c_5^2}{\partial \xi}\right) + \frac{3}{2}Ma\frac{\partial}{\partial \xi}\left(h^2\frac{\partial \theta(h)}{\partial \xi}\right). \tag{4.24}$$

We use the boundary conditions

$$h(0,t) = h_F, \tag{4.25}$$

$$h(L_\xi,t) = b, \tag{4.26}$$

$$\left.\frac{\partial h}{\partial \xi}\right|_{\xi=0} = \left.\frac{\partial h}{\partial \xi}\right|_{\xi=L_\xi} = 0, \tag{4.27}$$

where our domain runs from $\xi = 0$ to $\xi = L_\xi$. By assuming $\partial h/\partial t = 0$ and applying boundary conditions (4.25)-(4.27), equation (4.24) returns a steady-state solution for the interface height which we denote by $h_0(\xi)$. We make the substitution $h(\xi,t) \rightarrow h_0(\xi)$ in equation (4.24) and follow the same procedure as in Ref. [112] to convert equation (4.24) into the following ordinary differential equation for $h_0(\xi)$:

$$0 = Uh_0 - h_0^3\frac{d^3h_0}{d\xi^3} - h_0^3 + Co\,\varepsilon(1-\varepsilon)h_0^3\frac{dc_5^2}{d\xi} + \frac{3}{2}Ma\,h_0^2\frac{d\theta}{d\xi} + d, \tag{4.28}$$

where d is a constant of integration.

Application of the boundary conditions (4.25)-(4.27) (assuming uniform film thickness, uniform electrostatic potential, and uniform temperature at the ends of the domain) allows us to obtain

$$U = b^2 + b\,h_F + h_F^2, \tag{4.29}$$

$$d = -b\,h_F(b + h_F). \tag{4.30}$$

These expressions are equivalent to those found in previous studies, indicating that neither the presence of the electric field nor the temperature gradient appear to affect the velocity at which the film front moves down the substrate. However, equation (4.28) demonstrates that they do have an effect on the profile of the traveling wave through Co and Ma.

We solve for the traveling wave by specifying an initial condition for equation (4.24)

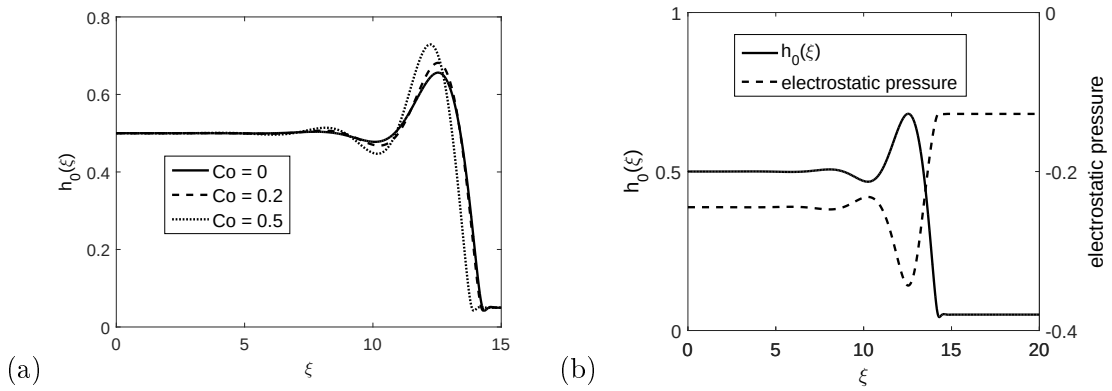

Figure 4.2: (a) Effect of electric field on traveling wave. Values of other parameters are $\varepsilon = 2.5$ and $Ma = 0$. (b) Electrostatic pressure overlaid with traveling wave profile for $Co = 0.2$.

and observing the long-time behavior of h. We use an initial condition similar to that in Ref. [91], a cubic polynomial with a contact line near the middle of the domain, given by

$$h(\xi, t = 0) = a_3\xi^3 + a_2\xi^2 + a_1\xi + a_0, \tag{4.31}$$

$$a_3 = 2(b - h_F)/(\xi_1 - \xi_2)^3, \tag{4.32}$$

$$a_2 = -3(b - h_F)(\xi_1 + \xi_2)/(\xi_1 - \xi_2)^3, \tag{4.33}$$

$$a_1 = 6(b - h_F)\xi_1\xi_2/(\xi_1 - \xi_2)^3, \tag{4.34}$$

$$a_0 = (-b\xi_1^3 + 3b\xi_1^2\xi_2 - 3h_F\xi_1\xi_2^2 + h_F\xi_2^3)/(\xi_1 - \xi_2)^3. \tag{4.35}$$

In our calculations, we typically choose $h_F = 0.5$, $b = 0.05$, and $L_\xi = 20$. The initial contact line is centered between ξ_1 and ξ_2, which are usually chosen to be $(\xi_1, \xi_2) = (14, 14.5)$. With this choice of parameters, the contact line settles well in the interior of our domain, minimizing the risk of edge effects. We use a fourth-order accurate centered finite-difference method to discretize equation (4.24), and $h_0(\xi)$ is obtained from the solution to equation (4.24) at long times.

4.3.1 Electrohydrodynamic effects on traveling wave

We begin by examining the effects of the electric field on the traveling wave. Figure 4.2(a) shows the film profile $h_0(\xi)$ near the contact-line region for several electric field strengths. It is evident that the electric field causes an increase in the height of the capillary ridge. Although we only present results for various values of Co, we note that an increase in the value of ε also enhances the growth of the capillary ridge.

The increase in capillary ridge height is due to electrohydrodynamic effects on the pressure. After non-dimensionalizing and applying the lubrication approximation, the pressure is found from the normal stress balance to be

$$p = -\nabla^2 h + Co\varepsilon(1-\varepsilon)c_5^2, \tag{4.36}$$

with the second term on the right representing the electrostatic contribution to the pressure, or electrostatic pressure. In Figure 4.2(b) we can see that there is a minimum in the electrostatic pressure in the region of the capillary ridge. In the early stages of flow, the ridge forms at the apparent contact line due to viscous resistance to gravity-driven flow in the positive ξ-direction. Simultaneously, the electrostatic pressure acts to drive liquid from thinner regions of the film to thicker regions. Capillary pressure must then oppose both of these effects, which is achieved by the interface developing higher curvature. As Co increases (or similarly, as ε increases), so too does the electrostatic pressure, which results in a higher capillary ridge.

4.3.2 Thermocapillary effects on traveling wave

The ability to control the direction of the temperature gradient allows for more control over the film profile than is possible with an electric field. By choosing either $\theta_t > \theta_b$ or $\theta_t < \theta_b$, the sign of Ma can be either negative or positive, respectively. Shown below is the dimensionless form of the tangential stress balance (4.6):

$$\left.\frac{\partial v_x}{\partial z}\right|_{z=h} = -Ma\frac{\partial\theta(z=h)}{\partial\xi}. \tag{4.37}$$

Due to the way we non-dimensionalize temperature, the direction of the tangential stress along the interface $h(\xi,t)$ is completely determined by the sign of Ma. This contrasts

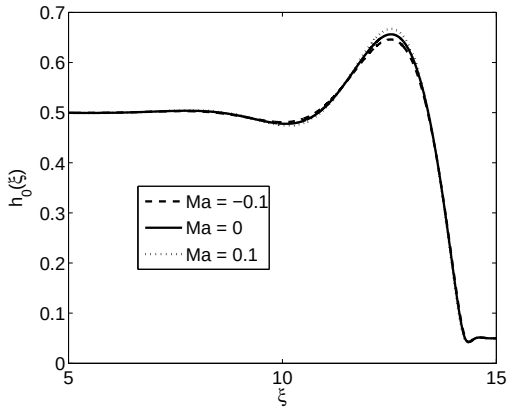

Figure 4.3: Traveling wave profiles for various values of Ma. Values of other parameters are $\kappa = 5$ and $Co = 0$.

with the contribution to the pressure from the electric field, which depends on Co and $c_5(h(\xi,t))^2$, both of which are invariant to the direction of the electric field. Since an increase in the conductivity ratio κ has the effect of reducing the magnitude of the temperature gradient, an increase in κ would lead to a reduction of thermocapillary effects.

Figure 4.3 compares the traveling wave profile in the absence of a temperature gradient with the traveling wave profile in the presence of two different temperature gradients. We see that $Ma > 0$, which corresponds to the top surface being cooled relative to the bottom surface, increases (albeit slightly) the height of the capillary ridge. In this case, a greater interfacial curvature is required for capillarity to counteract the combined effects of both the viscous resistance to gravity-driven flow and the upward shear stress generated from the temperature gradient along the liquid-air interface. Conversely, $Ma < 0$ slightly reduces the height of the capillary ridge as the thermocapillary stress now drives liquid down from the peak of the ridge.

4.4 Linear stability analysis

We now examine the stability of the traveling wave solutions to spanwise perturbations. We consider normal mode perturbations h_1 to the quasi-steady state h_0 using the

expansion

$$h(\xi, y, t) = h_0(\xi) + \delta h_1(\xi, y, t), \tag{4.38}$$

where h_1 has the form $h_1 = g(\xi, t)e^{iqy}$, q denotes the wave number of the perturbation, and δ is a small parameter multiplying the $O(1)$ function h_1. Substitution of this expansion into equation (4.24) yields the following partial differential equation for $g(\xi, t)$ to $O(\delta)$:

$$\begin{aligned}\frac{\partial g}{\partial t} =& U\frac{\partial g}{\partial \xi} - \frac{\partial}{\partial \xi}\left(h_0^3\frac{\partial^3 g}{\partial \xi^3}\right) + \frac{\partial}{\partial \xi}\left(q^2 h_0^3\frac{\partial g}{\partial \xi}\right) - \frac{\partial}{\partial \xi}\left(3h_0^2 g\right) - \frac{\partial}{\partial \xi}\left(3h_0^2\frac{d^3 h_0}{d\xi^3}g\right) + q^2 h_0^3\frac{\partial^2 g}{\partial \xi^2} - q^4 h_0^3 g \\ &- 2Co\varepsilon(\varepsilon-1)^2\frac{\partial}{\partial \xi}\left(h_0^3\frac{\partial}{\partial \xi}\left(c_{5,0}^3 g\right)\right) - 3Co\varepsilon(\varepsilon-1)\frac{\partial}{\partial \xi}\left(h_0^2\left(\frac{dc_{5,0}}{d\xi}\right)g\right) + 2q^2 Co\varepsilon(\varepsilon-1)^2 c_{5,0}^3 g \\ &+ \frac{3}{2}Ma\left[\frac{\partial}{\partial \xi}\left(2h_0\frac{dT_0}{d\xi}g\right) + \frac{\partial}{\partial \xi}\left(h_0^2\frac{\partial T_1}{\partial \xi}\right) - q^2 h_0^2 T_1\right],\end{aligned} \tag{4.39}$$

where

$$c_{5,0} = 1/(h_0(\varepsilon-1) - \varepsilon), \tag{4.40}$$

$$T_0 = (h_0 - 1)/(h_0(1-\kappa) - 1), \text{ and} \tag{4.41}$$

$$T_1 = \left[1/(h_0(1-\kappa)-1) + (1-\kappa)(h_0-1)/(h_0(1-\kappa)-1)^2\right] g. \tag{4.42}$$

For boundary conditions, we require $g(\xi, t)$ to decay to 0 as $\xi \to \pm\infty$. We then begin with a generic initial condition for g (we chose one period of a sine wave centered around $\xi = 10$, with $g(\xi, t) = 0$ everywhere else) and solve equation (4.39) numerically with a fourth-order accurate centered finite-difference method. At long times, $\partial g/\partial t$ grows or decays exponentially, and a growth rate σ at a given q can be calculated from the L^2-norm of g. [112]. This process is then repeated over a range of q values to obtain a dispersion relation.

4.4.1 Electrohydrodynamic effects on front stability

We first consider electrohydrodynamic effects on the stability of the film front in the absence of a temperature gradient, i.e. $Co \neq 0$ and $Ma = 0$. Before exploring the full range of wave numbers, we analytically examine the low-q limit in manner similar to that described in Ref. [112]. We assume g grows exponentially with t so that $g = \phi(\xi)e^{\sigma t}$,

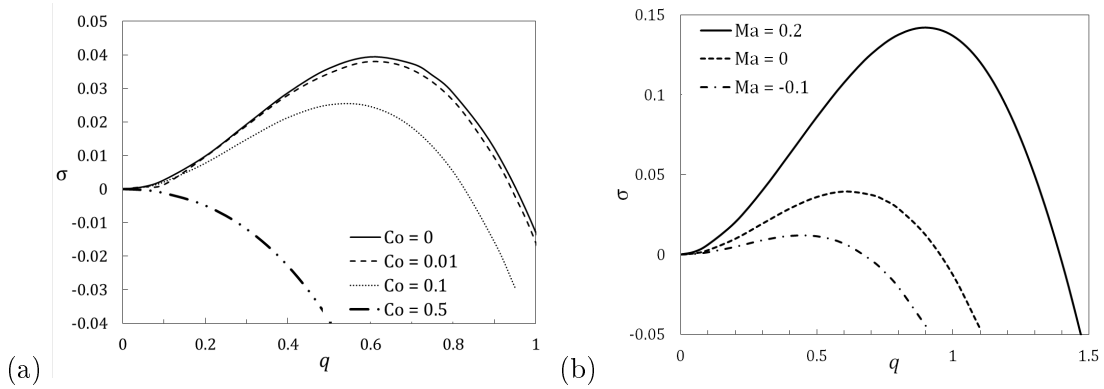

Figure 4.4: (a) Dispersion relations showing electrohydrodynamic effects on front stability at various values of Co. Values of other parameters are $\varepsilon = 2.5$ and $Ma = 0$. (b) Dispersion relations showing thermocapillary effects on front stability at various values of Ma. Values of other parameters are $\kappa = 5$ and $Co = 0$.

and then expand both σ and g as follows: $\sigma = \sigma_0 + q^2\sigma_1 + O(q^4)$ and $g = (\phi_0(\xi) + q^2\phi_1(\xi) + O(q^4))e^{\sigma t}$. These expansions are then substituted into equation (4.39) and expressions for σ_0 and σ_1 are obtained. We find that for $Co \neq 0$, $\sigma_0 = 0$ and the growth rate can be approximated to $O(q^2)$ by

$$\sigma \approx \frac{q^2}{h_F - b} \int_{-\infty}^{\infty} (h_0 - b)(h_0 - h_F)(h_0 + h_F + b) d\xi. \tag{4.43}$$

This expression is identical to that obtained in the absence of an electric field, suggesting that in the low-q limit, the electric field only influences stability through its effect on the shape of the base state $h_0(\xi)$.

Figure 4.4(a) shows the growth rate plotted against the wave number calculated from equation (4.39) at various values of Co. The results for $Co = 0$ agree well with previous studies [21, 23], with quantitative differences arising from differing initial conditions ($h_F = 0.5$ instead of 1, $b = 0.05$ instead of 0.1 or 0.01). Remarkably, the presence of an electric field reduces both the most unstable wave number and maximum growth rate. When $Co = 0.5$, the front appears to be linearly stable to perturbations of all wave numbers. Although not shown here for brevity, results from the asymptotic formula (4.43) agree well with solutions of equation (4.39) at low q.

The stabilization created by the electric field is in contrast to what one might expect

based on the results of section 3.1. The electric field increases the height of the capillary ridge, which might be expected to lead to a more unstable flow. Clearly, the electric field plays a larger role in the stability behavior than simply influencing the profile of the traveling wave. We look further into the mechanism for this stabilization in section 4.5.

4.4.2 Thermocapillary effects on front stability

We now consider thermocapillary effects on the stability of the film front in the absence of an electric field, i.e. $Ma \neq 0$ and $Co = 0$. We performed a low-q analysis of equation (4.39) for $Ma \neq 0$, but were unable to obtain an explicit expression for σ such as equation (4.43). Figure 4.4(b) shows the growth rate plotted against the wave number calculated from equation (4.39) at various values of Ma. Here we see that the effect of the temperature gradient on the instability is indicated by its effect on the capillary ridge. Temperature fields corresponding to $Ma > 0$ result in a higher capillary ridge, and accordingly increase the growth rate and most unstable wave number. Likewise, $Ma < 0$ results in a lower capillary ridge and stabilization of the front, as seen by the reduction of both the growth rate and most unstable wave number. However, we note that in both cases the influence of the temperature gradient on the instability is quite large and thus is unlikely to be explained solely by the relatively minor increase in the height of the capillary ridge of the traveling wave profile seen in Figure 4.3. We discuss the mechanisms for these effects in more detail in section 4.5.

4.5 Energy Analysis

In this section we perform an energy analysis similar to those done by Spaid and Homsy [23] and Tiwari *et al.* [113]. We can see from equation (4.39) that the time-rate-of-change of g is the sum of thirteen terms: seven which are present in the gravity-driven spreading problem [23], three which arise from the electric field (multiplied by Co), and three which result from the temperature field (multiplied by Ma).

The mechanical energy associated with the perturbation g of the capillary ridge is given by:

$$E = \frac{1}{2}\int_{-\infty}^{\infty} g^2 d\xi = \frac{1}{2}\langle g^2 \rangle. \tag{4.44}$$

We can rewrite equation (4.39) in a more compact form as

$$\frac{\partial g}{\partial t} = -L[g], \tag{4.45}$$

and take the inner product of equation (4.45) with g to obtain

$$\frac{\partial}{\partial t}\langle g^2 \rangle = 2\frac{\partial E}{\partial t} = \langle -L[g], g \rangle. \tag{4.46}$$

Assuming exponential dependence on time of g implies $\partial g/\partial t = \sigma g$ and thus

$$\sigma = \frac{\langle g, -L[g] \rangle}{\langle g, g \rangle} \tag{4.47}$$

We can now individually examine the contribution of each of the thirteen terms of L to the growth rate σ over a range of q. It follows that at a given q, the sum of the 13 terms equals σ. These terms are listed and described in Table 4.1. The first seven terms are identical to those listed in Ref. [23], while terms 8-10 result from the electric field and terms 11-13 come from the temperature gradient. Any term that is negative indicates that it has a stabilizing effect on the perturbation, while positive terms have a destabilizing effect.

Table 4.1: Terms of operator L in the stability problem along with their physical meanings

		Physical Meaning
Term 1	$U\frac{\partial g}{\partial \xi}$	Flow in ξ-direction due to reference velocity
Term 2	$-\frac{\partial}{\partial \xi}\left(h_0^3\frac{\partial^3 g}{\partial \xi^3}\right)$	Flow in ξ-direction due to ξ-curvature
Term 3	$\frac{\partial}{\partial \xi}\left(q^2 h_0^3\frac{\partial g}{\partial \xi}\right)$	Flow in ξ-direction due to y-curvature
Term 4	$-\frac{\partial}{\partial \xi}\left(3h_0^2 g\right)$	Flow in ξ-direction due to gravity
Term 5	$-\frac{\partial}{\partial \xi}\left(3h_0^2\frac{d^3 h_0}{d\xi^3}g\right)$	Flow in ξ-direction driven by base-state pressure gradient
Term 6	$q^2 h_0^3\frac{\partial^2 g}{\partial \xi^2}$	Flow in y-direction due to ξ-curvature
Term 7	$-q^4 h_0^3 g$	Flow in y-direction due to y-curvature
Term 8	$-2Co\varepsilon(\varepsilon-1)^2\frac{\partial}{\partial \xi}\left(h_0^3\frac{\partial}{\partial \xi}\left(c_{5,0}^3 g\right)\right)$	Flow in ξ-direction due to ξ-gradient in perturbed electrostatic pressure
Term 9	$-3Co\varepsilon(\varepsilon-1)\frac{\partial}{\partial \xi}\left(h_0^2\left(\frac{dc_{5,0}}{d\xi}\right)^2 g\right)$	Flow in ξ-direction due to ξ-gradient in base-state electrostatic pressure
Term 10	$2q^2 Co\varepsilon(\varepsilon-1)^2 c_{5,0}^3 g$	Flow in y-direction due to y-gradient in perturbed electrostatic pressure
Term 11	$\frac{3}{2}Ma\frac{\partial}{\partial \xi}\left(2h_0\frac{dT_0}{d\xi}g\right)$	Flow in ξ-direction due to ξ-gradient in base-state temperature field
Term 12	$\frac{3}{2}Ma\frac{\partial}{\partial \xi}\left(h_0^2\frac{\partial T_1}{\partial \xi}\right)$	Flow in ξ-direction due to ξ-gradient in perturbed temperature field
Term 13	$-\frac{3}{2}Ma\, q^2 h_0^2 T_1$	Flow in y-direction due to y-gradient in perturbed temperature field

We begin by examining the effects of the electric field on the first seven terms in Table 4.1. These are the standard terms that are present even in the absence of electric and temperature fields. Figure 4.5(a) shows each term plotted against q when the only external force present is gravity; the behavior is similar to that shown in Figure 13 of Ref. [23] (Term 1 is neglected because it is uniformly 0). Like with Figure 4.4, the quantitative differences between this study and that of Spaid and Homsy [23] arise from the difference in initial condition for $h(\xi, t=0)$. Figure 4.5(b) shows those same seven terms when an electric field is present, with the strength of the electric field taken as $Co = 0.2$. Other values of Co can be chosen, and although the precise values of the curves for each term will be different, the trends that we discuss below are largely the same.

Inspection of Figures 4.5(a) and (b) reveals that, in general, the electric field has

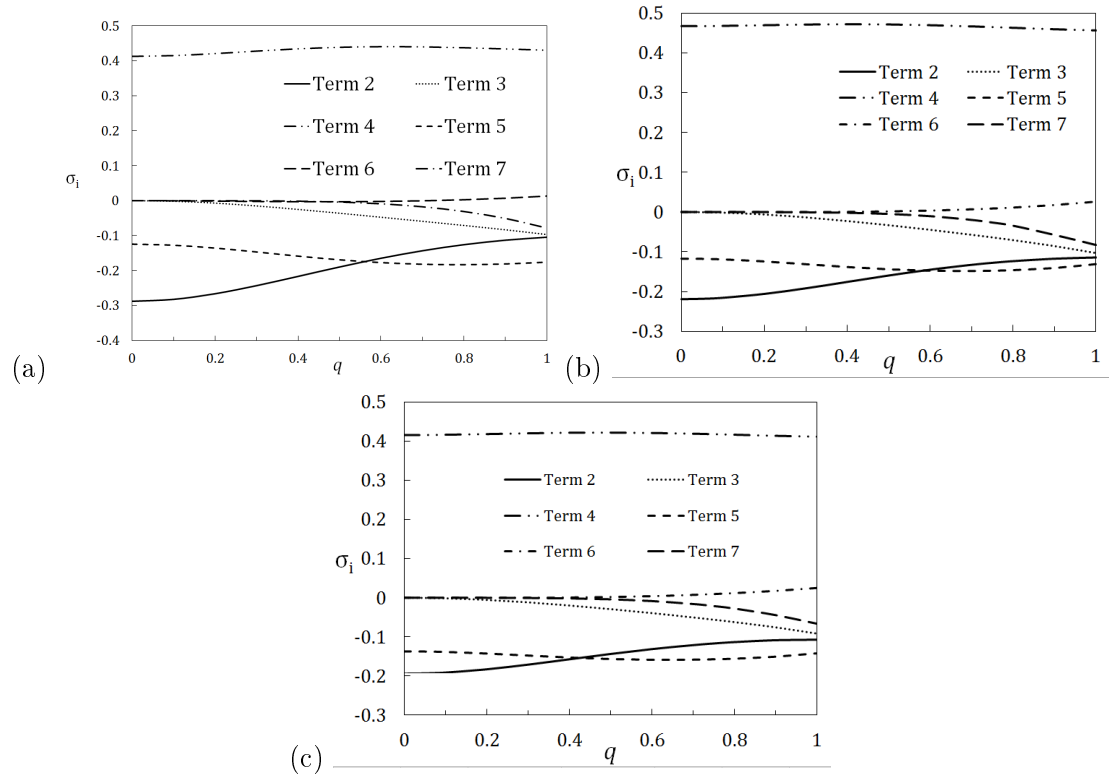

Figure 4.5: Contributions to the growth rate from each of the first seven terms of operator L. Panel (a) shows the terms with no electric or temperature field, panel (b) shows the terms in the presence of only an electric field ($Co = 0.2$), and panel (c) shows the terms in the presence of only a temperature field ($Ma = -0.1$). Values of other parameters are $\varepsilon = 2.5$ and $\kappa = 5$.

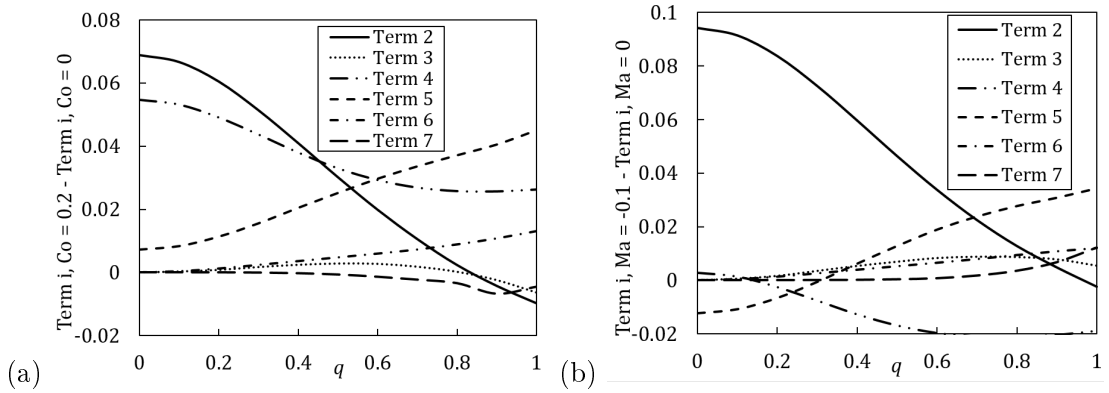

Figure 4.6: (a) Difference between each standard term with $Co = 0.2$ and $Co = 0$ with $\varepsilon = 2.5$. (b) Difference between each standard term with $Ma = -0.1$ and $Ma = 0$ with $\kappa = 5$.

a destabilizing effect on the standard terms. This is expected given that these terms represent the behavior of the perturbation g in response to the traveling wave profile of h_0—the higher capillary ridge should result in a larger contribution to the growth rate from these terms. At q lower than approximately 0.5, terms 2 and 4 are affected the most by the electric field. We see that term 2 in Figure 4.5(b), although still negative, is not as strongly stabilizing as when the electric field is absent. Term 4, representing flow in the ξ-direction due to gravity, is seen to have a greater value when an electric field is present.

We can get a more quantitative picture of how the electric field effects each physical mechanism by plotting the difference between each term with and without an electric field across the spectrum of q. In Figure 4.6(a) we see that up to approximately $q = 0.8$, terms 2, 4, and 5 show the largest increases as a consequence of the electric field. Term 7 is weakly stabilized by the electric field, but not enough to offset the increases seen in the other five terms. Indeed the collective sum of terms 1-7 is larger with an electric field than without.

This is the opposite of what we would expect after viewing Figure 4.4(a), which shows that the electric field reduces the growth rate of the perturbation. So the electric field must act on the perturbation in two competing ways. First as we just described, it destabilizes the front implicitly through its impact on the capillary ridge, as demonstrated by examining the standard terms of L (Figures 4.5(a) and (b)). Second, the

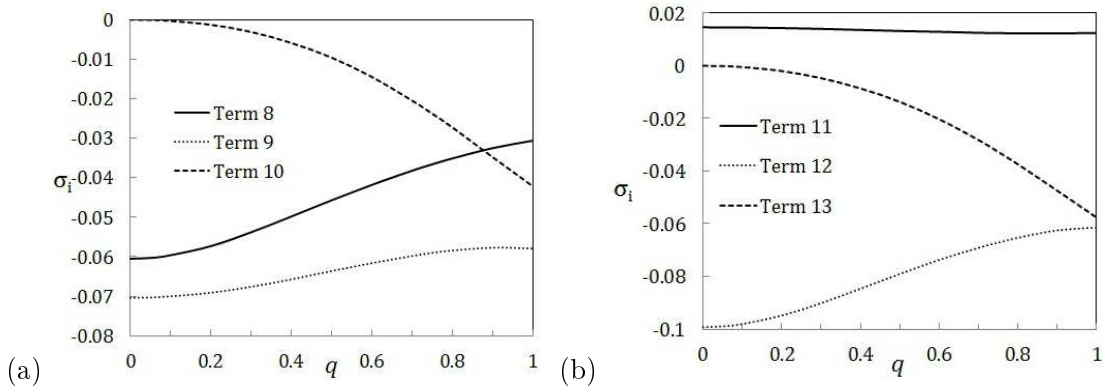

Figure 4.7: Energy analysis results for (a) $Co = 0.2$, $\varepsilon = 2.5$ ($Ma = 0$) and (b) $Ma = -0.1$, $\kappa = 5$ ($Co = 0$).

electric field must act directly on the perturbation to stabilize it to generate the decreased growth rates shown in Figure 4.4(a). This corresponds to the additional terms in the operator L that are multiplied by Co.

We now turn to examining these additional terms. Figure 4.7(a) shows the contributions to the growth rate from terms 8-10 introduced by the electric field. All three terms are non-positive over the range of q shown. Terms 8 and 9, resulting from ξ-curvature in the perturbed and base-state electrostatic pressure, respectively, begin as strongly stabilizing and gradually decrease in magnitude as q increases. Term 10 arises from y-curvature of the perturbed electrostatic pressure field and scales as $-q^2$, rapidly stabilizing the film front as q increases. Thus when the contributions from terms 8-10 are included, the net effect of the electric field is to reduce the overall growth rates of the spanwise perturbations.

To examine the effects of thermocapillarity on the standard terms, we compare Figure 4.5(c) to 4.5(a). Term 4 is now slightly more stabilizing relative to the case with no temperature and electric field. This is to be expected as term 4 is the contribution from gravity acting on the film, and this action is reduced due to the smaller size of the capillary ridge. We see that term 2, originating from the curvature of the perturbed height profile, is significantly less stabilizing than it is in the case with no temperature field. The difference between each standard term at $Ma = -0.1$ and $Ma = 0$ is shown in Figure 4.6(b). From this plot, we can see that the differences between most terms follow

the same trends as they do in Figure 4.6(a). Overall, the contribution to the growth rate from terms 1-7 is slightly increased at low q, but rapidly decreases at $q > 0.6$ mainly due to terms 2 and 4. The rest of the stabilization is due to thermocapillary effects acting directly on the perturbed height profile, as evidenced by terms 11-13 and discussed below.

We plot the effects of terms 11-13 across a range of wave numbers in Figure 4.7(b). Here we see mixed contributions from the interfacial temperature gradient, with term 11 destabilizing the perturbation and terms 12 and 13 acting as stabilizing influences. Term 11 is a result of the ξ-curvature of the base-state temperature field, while terms 12 and 13 both come from curvature of the perturbed temperature field. At low q, there is negligible y-curvature in the perturbed temperature field so term 13 is also negligible. Thus, term 12, arising from ξ-curvature of the perturbed temperature field is the dominant stabilizing mechanism until $q \approx 1$. Interestingly term 11, which arises from the base-state temperature field, is approximately constant across the range of q shown, consistent with the fact that the base-state temperature field is independent of q.

We now offer additional physical explanations for the effects that electric and temperature fields have on the stability of the film front. By supposing a sinusoidal form of the disturbance $g(\xi, t)$, the perturbation to $h_0(\xi)$ generates alternating thick and thin regions of liquid in the y-direction. Spaid and Homsy [23] postulate two possible explanations for why fingers result from this alternating thickness profile. First, the thicker regions are more massive and thus are pushed forward more rapidly by the body force. Second, the thicker regions are less affected by viscous drag, increasing the mobility in these regions of the film. Either way, faster growth of $g(\xi, t)$ increases the height disparity between the thick and thin regions of the liquid and will result in earlier onset of the fingering instability.

In Figure 4.8, we plot the traveling wave solution $h_0(\xi)$ and corresponding eigenfunction $g(\xi, t)$ of the operator L with $q = 0.5$ in the presence of (a) no electric or temperature field, (b) an electric field ($Co = 0.2$), and (c) a temperature field ($Ma = -0.1$). In each case, the non-zero region of the eigenfunction develops in the same region of the domain as the *leading face* of the capillary ridge. The growth rate σ is calculated from the L^2-norm of $g(\xi, t)$, and because $g(\xi, t)$ is zero everywhere except on the leading face of the

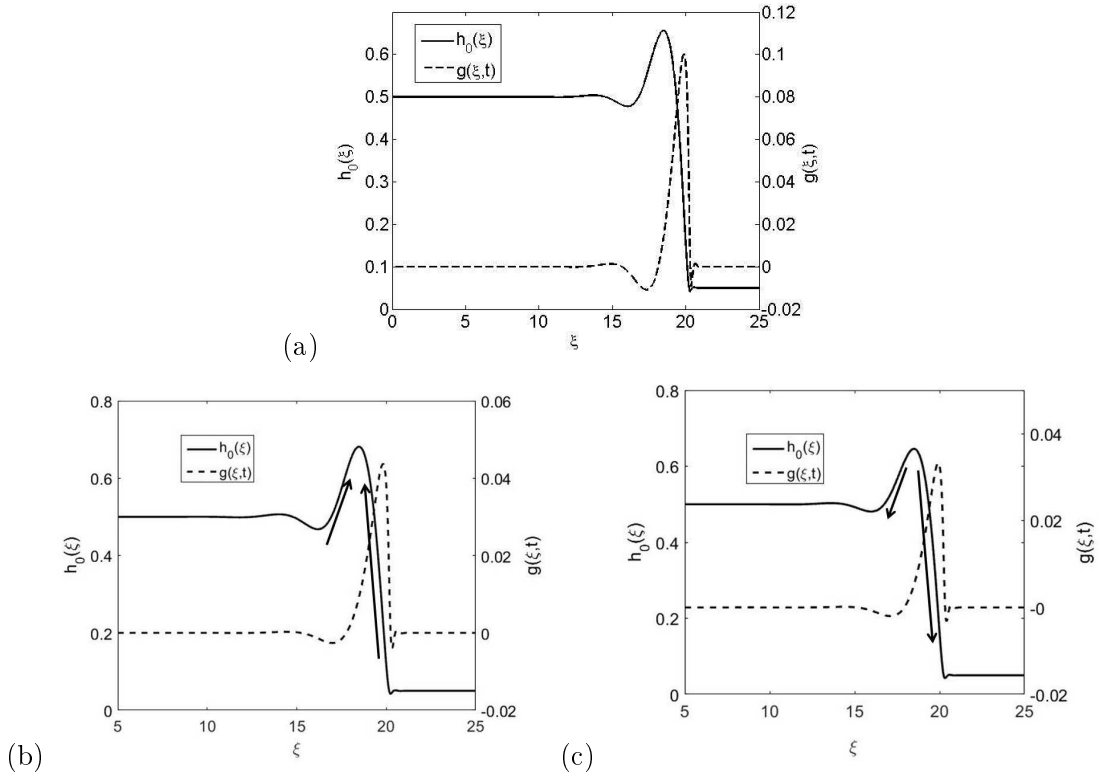

Figure 4.8: Eigenfunctions of operator $L(q = 0.5)$ overlaid with base states for (a) $Co = 0$, $Ma = 0$, (b) $Co = 0.2$, $\varepsilon = 2.5$ ($Ma = 0$) and (c) $Ma = -0.1$, $\kappa = 5$ ($Co = 0$). Arrows in panels (b) and (c) denote the direction of flow driven by (b) base-state electrostatic pressure and (c) base-state thermocapillary force.

capillary ridge, its growth in this region determines the growth rate of the instability.

To understand the role the electric field plays in inhibiting the growth of the instability, recall the distribution of the electrostatic pressure in the traveling wave solution to equation (4.24). Figure 4.2(b) shows that there is a minimum in electrostatic pressure located directly on the capillary ridge which increases its height by pumping liquid from the surrounding areas. As the arrows show in Figure 4.8(b), one of the regions from which the base-state electrostatic pressure pumps liquid is the leading face of the capillary ridge, i.e. the region most critical to the growth of $g(\xi, t)$. This action of the base state electrostatic pressure inhibits the ability of $g(\xi, t)$ to grow in that region and results in the negative values of Term 9 that we see in Figure 4.7(a). We see that terms 8 and 10 are also stabilizing to lesser degrees, and both terms are highly coupled to the base-state electric field. Thus, the electric field decreases the growth rate of the instability (Figure 4.4(a)).

The eigenfunction $g(\xi, t)$ and base state $h_0(\xi)$ for the case of thermocapillary stabilization is shown in Figure 4.8(c). Once again the non-zero part of $g(\xi, t)$ develops on the leading face of the capillary ridge. In this case, the arrows in Figure 4.8(c) show that thermocapillary forces from the base-state temperature gradient pump liquid down from the peak of the capillary ridge into the region where $g(\xi, t)$ is non-zero (i.e., from the hotter region with lower surface tension to the cooler regions with higher surface tension). This base-state thermocapillary flow encourages the growth of $g(\xi, t)$ and causes term 11 to be positive, thus increasing the growth rate (see Figure 4.7(b)). However we also see in Figure 4.7(b) that terms 12 and 13, which arise due to gradients in the perturbed temperature field, are strongly stabilizing. This is because thermocapillary stresses in the height perturbation drive liquid out of the hotter peaks and into the cooler valleys of $g(\xi, t)$, flattening the perturbation and slowing the growth of $g(\xi, t)$. We see that the combined stabilization from terms 12 and 13 outweighs the destabilizing effect of term 11, thus generating the overall diminished growth rates seen in Figure 4.4(b) for $Ma < 0$.

4.6 Conclusions

In this paper we have examined the effects of electric and temperature fields on the linear stability of gravity-driven thin liquid films with contact lines. We considered a perfect dielectric liquid with surface tension that decreases linearly with increasing temperature. Using lubrication theory, an evolution equation for the film thickness was derived which predicted the existence of traveling wave liquid profiles in the presence of both electric and temperature fields. We found that the electric field always acts to increase the height of the capillary ridge of the traveling wave profile. Despite the fact that increases in capillary ridge height generally promote the fingering instability, the electric field was found to decrease both the growth rate and most unstable wave number of the instability. Furthermore, the front can be completely stabilized by making the electric field sufficiently strong. A temperature field can either increase (when $Ma > 0$) or decrease (when $Ma < 0$) the height of the capillary ridge of the traveling wave profile, depending on the direction of the temperature gradient.

An energy analysis was performed to gain insight into the physical mechanisms behind the effects that electric and temperature fields have on the linear stability of driven films. In the case of electric fields, it was determined that the base-state electrostatic pressure was the dominant force responsible for stabilization of the film front. With temperature fields such that $Ma < 0$, the dominant stabilizing mechanisms were from the gradients in the perturbed temperature field.

In both the cases of electric and temperature fields, it was found that these external forces impact stability not only through their influence on the capillary ridge, but also through the perturbed profiles of the interface height. Because the analysis was focused mainly on regimes where perturbation growth rates are positive, transient amplification was not considered [114]. It is possible that in situations where the growth rates are significantly damped by either an electric or temperature field, transient amplification of disturbances may become important. A transient analysis and three-dimensional nonlinear simulations would be helpful toward developing a more complete understanding of electrohydrodynamic and thermocapillary effects on the fingering instability in gravity-driven spreading films.

Chapter 5

Final Remarks

In this thesis, we have considered several mathematical models related to electrohydrodynamic and thermocapillary effects on thin film flows. In this chapter we summarize the key results and propose future research directions which will lead to greater insight on using external forces to control thin film flows.

5.1 Conclusions

5.1.1 Conclusions on electrohydrodynamic and thermocapillary patterning

In Chapter 2 we studied the patterning of thin liquid films using electric and temperature gradients. We investigated the regimes in which the electric field and temperature gradient each would most contribute to the growth of the hexagonal patterns of pillars. A linear stability analysis was conducted which incorporated a linear viscoelastic model, and nonlinear simulations were conducted in the case of Newtonian liquids. We examined two different models for heat transfer through the film: thermal convection and thermal conduction. It was found that in configurations typical to electrohydrodynamic or thermocapillary patterning, heat transfer by thermal convection would be negligible compared to heat transfer by thermal conduction. In the case of perfect dielectric films, thermocapillary forces tend to dominate the patterning process. We found that an interfacial electrohydrodynamic force sufficient to affect patterning will not be generated

without the accumulation of charge at the interface. In the case of leaky dielectric films, that is films with low but nonzero conductivity, both electrohydrodynamic and thermocapillary forces contribute significantly to the patterning process. The linear stability analysis showed that controlling the rheology of the film can modify the growth rate of the pillars without affecting the wavelength of the pillar pattern. Increasing the elasticity of the polymer will increase the growth rate of the pattern, while increasing the amount of solvent in the solution will decrease the growth rate. These results demonstrated that smaller feature sizes are achievable through the simultaneous application of electric and temperature fields.

5.1.2 Conclusions on electrohydrodynamic and thermocapillary effects on gravity-driven spreading

In Chapter 3, we investigated electrohydrodynamic and thermocapillary effects on gravity-driven droplet spreading. We used nonlinear simulations in order to study the effect that electric and temperature fields would have on the shape of the liquid-air interface. Both perfect dielectric and leaky dielectric liquids were considered, in addition to both perfectly and partially wetting liquids. It was found that in perfect dielectric liquids, the electric field increases the height of the capillary ridge near the front of the droplet. A secondary ridge immediately behind the capillary ridge can also grow at high electric field strengths before either flattening out naturally or merging with the capillary ridge. Despite affecting the growth of the capillary ridges, the droplet eventually settles into a quasi-steady state and uniformly flattens as it spreads over the substrate. It was found for leaky dielectric liquids that surface charge can generate interfacial shear stresses strong enough to induce several minor ridges to grow. Continued growth of minor ridges eventually leads to splitting up of the main drop into a series of smaller droplets. Thermocapillary forces can be used to inhibit the growth of the minor ridges by cooling the droplet from below (or equivalently heating it from above). For liquids that are partially wetting, the main drop is more susceptible to splitting into a series of smaller droplets. In partially wetting liquids even perfect dielectric drops are observed to split. Again, thermocapillary forces can be used as a means of preventing or slowing the division of the main drop.

5.1.3 Conclusions on electrohydrodynamic and thermocapillary stabilization of dynamic contact lines

In Chapter 4, we used a linear stability analysis to study the effects of electric and temperature fields on the contact line instability of gravity-driven thin film flows. We found the surprising result that in perfect dielectric films, the electric field actually stabilizes the contact line and inhibits the growth of fingers or rivulets. This was surprising because the increased height of the capillary ridge has generally been linked to destabilization of the contact line, and the electric field increases the height of the capillary ridge. However, an energy analysis revealed that there are complex interactions between the base-state electric field and the disturbances at the contact line which serve to inhibit their growth. Thermocapillary forces can either enhance or diminish the growth of the disturbances depending on the direction of the temperature field. Again, there were interactions between the base-state temperature field and perturbations which governed the manner in which the disturbances grew. These results demonstrated that electric fields and temperature gradients could be of use in suppressing the fingering instability in gravity-driven thin film flows.

5.2 Future Research Directions

In this thesis we have investigated electrohydrodynamic and thermocapillary effects on thin liquid films using a number of model geometries which are motivated by situations that could arise in industrial applications. There are many unanswered questions on each of these problems which are worth pursuing in future work.

Further analysis on viscoelastic effects on combined EHD and TC patterning is certainly warranted. Our work incorporated only a single linear viscoelastic model when there are countless varieties of polymers and polymeric solutions which encompass a wide spectrum of non-Newtonian effects. On one hand, it could prove useful to perform nonlinear simulations on the two-dimensional film using the full Oldroyd-B model as opposed to linearizing it and only investigating viscoelastic effects in the context of a linear stability analysis. Performing simulations such as this would reveal whether there are nonlinear viscoelastic effects which impact more than just the growth rate of the instability, such as most unstable wavelength or the shape of the pillars. On the

other hand, exploring other linear models within a linear stability analysis could also be enlightening on the extent to which non-Newtonian effects can impact the growth rate and wavelength of the instability.

There is also much more worth studying regarding the effects of electric and temperature fields on gravity-driven film spreading. For constant-volume droplets, extending the model to three dimensions would allow one to compare theoretical results to discrete droplets, opposed to long and slender liquid sheets. Also, exploring different geometries of the electric field could also facilitate comparison to situations closer to what might be encountered in industry. For example, while the parallel plate configuration is advantageous in that it allows us to use the lubrication approximation to describe the electric field in the air layer, it is not a good approximation to the electric field that might be present in electrospray coating. Instead, it would prove useful to model the electric field as emanating from a point source of very high voltage very far away from the liquid film. In using the parallel plate configuration we made efforts to approximate the electric field strength felt through the film in electrospray coating, but our model does not capture the decaying strength of the electric field as the liquid film moves down the substrate.

In our investigation on contact-line stability, we modeled the electrohydrodynamics of the liquid using the perfect dielectric model. This was done because we were unable to verify that a steady-state would ever exist for a leaky dielectric film. However, there may be situations involving charge bound to the surface of a perfect dielectric film where steady solutions to the height evolution and charge conservation equations may be found. If this is the case, then it would be possible to perform a linear stability analysis that would reveal what effect surface charge would have on the fingering instability. It may also be interesting to include temperature-dependent viscosity in the model. The results in this thesis suggest that a temperature gradient could be imposed on the film to stabilize the contact line, but we did not consider the possible effects of a viscosity that varies with temperature. If there is a significant difference in temperature between the liquid in contact with the substrate and the liquid at the interface, then this could impact the shape or existence of a steady state as well as the development of the contact-line instability.

5.3 Outlook

As the complexity of microelectronic and microfluidic devices continues to increase, the demand for greater control over liquids at small length scales will increase with it. Electric and temperature fields provide myriad ways of manipulating liquids at the micro- and nano-scales. Electrohydrodynamic and thermocapillary models can offer descriptions of the phenomena that are observed as well as inspire new methods for controlling liquid coating flows. We hope that the information contained in this thesis will improve our understanding of how electric and temperature fields influence thin film flows and will help to drive further research into electrohydrodynamic and thermocapillary effects in liquid coatings.

References

[1] E. Schaffer, T. Thurn-Albrecht, T.P. Russell, and U. Steiner. Electrically induced structure formation and pattern transfer. *Nature*, 403:874–877, 2000.

[2] J. Peng, H. Wang, B. Li, and Y. Han. Pattern formation in a confined polymer film induced by a temperature gradient. *Polymer*, 45:8013–8017, 2004.

[3] H. Huppert. Flow and instability of a viscous current down a slope. *Nature*, 300:427–429, 1982.

[4] H. Assender, V. Bliznyuk, and K. Porfyrakis. How surface topography relates to materials' properties. *Science*, 297:973–976, 2002.

[5] Q. Xia and S.Y. Chou. Applications of excimer laser in nanofabrication. *Appl. Phys. A*, 98:9–59, 2010.

[6] N. Arun, A. Sharma, P. Pattader, I. Banerjee, H. Dixit, and K. Narayan. Electric-Field-Induced Patterns in Soft Viscoelastic Films: From Long Waves of Viscous Liquids to Short Waves of Elastic Solids. *Phys. Rev. Lett.*, 102(25):1–4, June 2009.

[7] L.F. Pease III and W.B. Russel. Electrostatically induced submicron patterning of thin perfect and leaky dielectric films: A generalized linear stability analysis. *J. Chem. Phys.*, 118:3790–3803, 2003.

[8] S.A. Roberts and S. Kumar. AC electrohydrodynamic instabilities in thin liquid films. *J. Fluid Mech.*, 631:255–279, 2009.

[9] L. Espín, A. Corbett, and S. Kumar. Electrohydrodynamic instabilities in thin viscoelastic films - AC and DC fields. *J. Non-Newtonian Fluid Mech.*, 196:102–111, 2013.

[10] L. Wu and S.Y. Chou. Electrohydrodynamic instability of a thin film of viscoelastic polymer underneath a lithographically manufactured mask. *J. Non-Newtonian Fluid Mech.*, 125:91–99, 2005.

[11] G. Tomar, V. Shankar, A. Sharma, and G. Biswas. Electrohydrodynamic instability of a confined viscoelastic liquid film. *J. Non-Newtonian Fluid Mech.*, 143:120–130, 2007.

[12] M. Dietzel and S.M. Troian. Formation of nanopillar arrays in ultrathin viscous films: The critical role of thermocapillary stresses. *Phys. Rev. Lett.*, 103:074501, 2009.

[13] E. McLeod, Y. Liu, and S.M. Troian. Experimental verification of the formation mechanism for pillar arrays in nanofilms subject to large thermal gradients. *Phys. Rev. Lett.*, 106:175501, 2011.

[14] R. Goodwin and G.M. Homsy. Viscous flow down a slope in the vicinity of a contact line. *Phys. Fluids A*, 3:515–528, 1991.

[15] J.A. Moriarty, L.W. Schwartz, and E.O. Tuck. Unsteady spreading of thin liquid films with small surface tension. *Phys. Fluids A*, 3:733–742, 1991.

[16] L.W. Schwartz, D. Roux, and J.J. Cooper-White. On the shapes of droplets that are sliding on a vertical wall. *Physica D*, 209:236–244, 2005.

[17] T. Podgorski, J.-M. Flesselles, and L. Limat. Corners, cusps, and pearls in running drops. *Phys. Rev. Lett.*, 87:036102, 2001.

[18] P. Kim, C. Duprat, S.S.H. Tsai, and H.A. Stone. Selective spreading and jetting of electrically driven dielectric films. *Phys. Rev. Lett.*, 107:034502, 2011.

[19] J.M. Davis, D.E. Kataoka, and S.M. Troian. Transient dynamics and structure of optimal excitations in thermocapillary spreading: Precursor film model. *Phys. Fluids*, 18:092101, 2006.

[20] N. Silvi and E.B. Dussan V. On the rewetting of an inclined solid surface by a liquid. *Phys. Fluids*, 28:5–7, 1985.

[21] S.M. Troian, E. Herbolzeimer, S.A. Safran, and J.F. Joanny. Fingering instabilities of driven spreading films. *Europhys. Lett.*, 10:25–30, 1989.

[22] D.T. Moyle, M.-S. Chen, and G.M. Homsy. Nonlinear rivulet dynamics during unstable wetting flows. *Int. J. Multiphase Flow*, 25:1243–1262, 1999.

[23] M.A. Spaid and G.M. Homsy. Stability of Newtonian and viscoelastic dynamic contact lines. *Phys. Fluids*, 8:460–478, 1996.

[24] A.L. Bertozzi and M.P. Brenner. Linear stability and transient growth in driven contact lines. *Phys. Fluids*, 9:530–539, 1997.

[25] L. Kondic and J. Diez. Pattern formation in the flow of thin films down an incline: Constant flux configuration. *Phys. Fluids*, 13:3168–3184, 2001.

[26] M.F.G. Johnson, R.A. Schluter, M.J. Miksis, and S.G. Bankoff. Experimental study of rivulet formation on an inclined plate by fluorescent imaging. *J. Fluid Mech.*, 394:339–354, 1999.

[27] L. Rayleigh. On the equilibrium of liquid conducting masses charged with electricity. *Phil. Mag. Ser.*, 14:184–186, 1882.

[28] D.A. Saville. Electrohydrodynamics: The Taylor-Melcher Leaky Dielectric Model. *Annu. Rev. Fluid Mech.*, 29:27–64, 1997.

[29] R.S. Allan and S.G. Mason. Particle behavior in shear and electric fields. i. deformation and burst of fluid drops. *Proc. R. Soc. A*, 267:45–61, 1962.

[30] G.I. Taylor. Studies in electrohydrodynamics i. the circulation produced in a drop by an electric field. *Proc. R. Soc. A*, 291:159–166, 1966.

[31] S. Torza, R.G. Cox, and S.G. Mason. Electrohydrodynamic deformation and burst of liquid drops. *Phil. Trans. R. Soc. A*, 269:295–319, 1971.

[32] O.O. Ajayi. A note on taylor's electrohydrodynamic theory. *Proc. R. Soc. A*, 364:499–507, 1978.

[33] J.C. Baygents and D.A. Saville. The circulation produced in a drop by an electric field: A high field strength electrokinetic model. *AIP Conf. Proc.*, 197:7–17, 1990.

[34] O. Vizika and D.A. Saville. The electrohydrodynamic deformation of drops suspended in liquids in steady and oscillatory fields. *J. Fluid Mech.*, 239:1–21, 1992.

[35] B.R. Fish. Electrical generation of natural aerosols from vegetation. *Science*, 175:1239–1240, 1972.

[36] S.I. Betelú and M.A. Fontelos. Spreading of a charged microdroplet. *Physica D*, 209:28–35, 2005.

[37] L.Y. Yeo, R.V. Craster, and O.K. Matar. Drop manipulation and surgery using electric fields. *J. Colloid Interface Sci.*, 306:368–378, 2007.

[38] A.W. Wray, D.T. Papageorgiou, R.V. Craster, K. Sefiane, and O.K. Matar. Electrostatic suppression of the "coffee stain effect". *Langmuir*, 30:5849–5858, 2014.

[39] J.R. Melcher and C.V. Smith. Electrohydrodynamic charge relaxation and interfacial perpendicular-field instability. *Phys. Fluids*, 12:778–790, 1969.

[40] D.J. Harris, H. Hu, J.C. Conrad, and J.A. Lewis. Patterning colloidal films via evaporative lithography. *Phys. Rev. Lett.*, 98:148301, 2007.

[41] S.H. Davis. Thermocapillary instabilities. *Annu. Rev. Fluid Mech.*, 19:403–435, 1987.

[42] A. Oron, S.H. Davis, and S.G. Bankoff. Long-scale evolution of thin liquid films. *Rev. Mod. Phys.*, 69:931–980, 1997.

[43] S.Y. Chou, L. Zhuang, and L. Guo. Lithographically induced self-construction of polymer microstructures for resistless patterning. *Appl. Phys. Lett.*, 75:1004–1006, 1999.

[44] S.Y. Chou and L. Zhuang. Lithographically induced self-assembly of periodic polymer micropillar arrays. *J. Vac. Sci. Technol., B*, 17:3197, 1999.

[45] N. Wu and W.B. Russel. Micro- and nano-patterns created via electrohydrodynamic instabilities. *Nano Today*, 4:180, 2009.

[46] Shankar V. and A. Sharma. Instability of the interface between thin fluid films subjected to electric fields. *J. Colloid Interface Sci.*, 274:294–308, 2004.

[47] R.V. Craster and O.K. Matar. Electrically induced pattern formation in thin leaky dielectric films. *Phys. Fluids*, 17:032104, 2005.

[48] N. Wu, L.F. Pease, and W.B. Russel. Electric-field-induced patterns in thin polymer films: weakly nonlinear and fully nonlinear evolution. *Langmuir*, 21:12290, 2005.

[49] D Bandyopadhyay and A. Sharma. Electric field induced instabilities in thin confined bilayers. *J. Colloid Interface Sci.*, 311:595, 2007.

[50] R.J. Deissler and A. Oron. Stable localized patterns in thin liquid films. *Phys. Rev. Lett.*, 68:2948–2951, 1992.

[51] L.Y. Yeo, R.V. Craster, and O.K. Matar. Marangoni instability of a thin liquid film resting on a locally heated horizontal wall. *Phys. Rev. B*, 67:056315, 2003.

[52] E. Schaffer, S. Harkema, M. Roerdink, R. Blossey, and U. Steiner. Morphological instability of a confined polymer film in a thermal gradient. *Macromolecules*, 36:1645–1655, 2003.

[53] M. Dietzel and S.M. Troian. Mechanism for spontaneous growth of nanopillar arrays in ultrathin films subject to a thermal gradient. *J. Appl. Phys.*, 108:074308, 2010.

[54] F.A. Morrison. *Understanding Rheology.* Oxford University Press, 2001.

[55] H. Hansen. Method for spray-coating medical devices. US patent 6669980B2. 2003.

[56] D. Maza, S. Kumar, and M.S. Carvalho. Spreading and merging of liquid streams flowing down an inclined plane: Modeling and experiments. *Chem. Eng. Sci.*, 95:221–231, 2013.

[57] C. Girotto, B.P. Rand, J. Genoe, and P. Heremans. Exploring spray coating as a deposition technique for the fabrication of solution-processed solar cells. *Sol. Energ. Mat. Sol. C.*, 93:454–458, 2009.

[58] B. Preinerstorfer, M. Lämmerhofer, and W. Lindner. Advances in enantioselective separations using electromigration capillary techniques. *Electrophoresis*, 30:100–132, 2009.

[59] A. Ramkrishnan and S. Kumar. Electrohydrodynamic effects in the leveling of coatings. *Chem. Eng. Sci.*, 101:785–799, 2013.

[60] O.V. Salata. Tools of nanotechnology: Electrospray. *Curr. Nanosci.*, 1:25–33, 2005.

[61] J.U. Park, M. Hardy, S.J. Kang, K. Barton, K. Adair, D.K. Mukhopadhyay, C.Y. Lee, M.S. Strano, A.G. Alleyne, J.G. Georgiadis, P.M. Ferreira, and J.A. Rogers. High-resolution electrohydrodynamic jet printing. *Nat. Mater.*, 6:782–789, 2007.

[62] F. Mugele. Fundamental challenges in electrowetting: From equilibrium shapes to contact angle saturation and drop dynamics. *Soft Matter*, 5:3377–3384, 2009.

[63] V. Vancauwenberghe, P. Di Marco, and D. Brutin. Wetting and evaporation of a sessile drop under an external electrical field: A review. *Colloids and Surfaces A: Physiochem. Eng. Aspects*, 432:50–56, 2013.

[64] L. Chen and E. Bonaccurso. Electrowetting - from statics to dynamics. *Adv. Colloid Interface Sci.*, 210:2–12, 2014.

[65] S.R. Mahmoudi, K. Adamiak, G.S.P. Castle, and K.K. Varanasi. Electrostatic precursor films. *Soft Matter*, 9:9918–9923, 2013.

[66] T.B. Jones, M. Gunji, M. Washizu, and M.J. Feldman. Dielectrophoretic liquid actuation and nanodroplet formation. *J. Appl. Phys.*, 89:1441–1448, 2001.

[67] C.W.J. Berendsen, C.J. Kuijpers, J.C.H. Zeegers, and A.A. Darhuber. Dielectrophoretic deformation of thin liquid films induced by surface charge patterns on dielectric substrates. *Soft Matter*, 9:4900–4910, 2013.

[68] M.A. Fontelos and U. Kindelán. The shape of charged drops over a solid surface and symmetry-breaking instabilities. *SIAM J. Appl. Math.*, 69:126–148, 2008.

[69] S.R. Mahmoudi, K. Adamiak, and G.S.P. Castle. Spreading of a dielectric droplet through an interfacial electric pressure. *Proc. R. Soc. A*, 467:3257–3271, 2011.

[70] S.R. Mahmoudi, K. Adamiak, and G.S.P. Castle. On the corona discharge spreading of dielectric liquid films. *J. Electrostat.*, 71:496–498, 2013.

[71] D. Orefon, K. Sefiane, and M.E.R. Shanahan. Evaporation of nanofluid droplets with applied DC potential. *J. Colloid Interface Sci.*, 407:29–38, 2013.

[72] O. Ghazian, K. Adamiak, and G.S.P. Castle. Electric-field-induced oscillations of water droplets deposited on insulating surfaces. *J. Electrostat.*, 71:489–495, 2013.

[73] O. Ghazian, K. Adamiak, and G.S.P. Castle. Spreading and retraction control of charged dielectric droplets. *Colloids and Surfaces A*, 448:23–33, 2014.

[74] F.Y. Leong, U.M. Mirsaidov, P. Matsudaira, and L. Mahadevan. Dynamics of a nanodroplet under a transmission electron microscope. *Phys. Fluids*, 26:012003, 2014.

[75] L.T. Corson, C. Tsakonas, B.R. Duffy, N.J. Mottram, I.C. Sage, C.V. Brown, and S.K. Wilson. Deformation of a nearly hemispherical conducting drop due to an electric field: Theory and experiment. *Phys. Fluids*, 26:122106, 2014.

[76] I. Roghair, M. Musterd, D. van den Ende, C. Kleijn, M. Kreutzer, and F. Mugele. A numerical technique to simulate display pixels based on electrowetting. *Microfluid. Nanofluid.*, 19:465–482, 2015.

[77] D. Crowdy. Exact solutions for the static dewetting of two-dimensional charged conducting droplets on a substrate. *Phys. Fluids*, 27:061705, 2015.

[78] M. Luo, R. Gupta, and J. Fréchette. Modulating contact angle hysteresis to direct fluid droplets along a homogeneous surface. *ACS Appl. Mater. Interfaces*, 4:890–896, 2012.

[79] M. Ouriemi and P.M. Vlahovska. Electrohydrodynamics of particle-covered drops. *J. Fluid Mech.*, 751:106–120, 2014.

[80] D. Tseluiko, M.G. Blyth, D.T. Papageorgiou, and J.-M. Vanden-Broeck. Electrified viscous thin film flow over topography. *J. Fluid Mech.*, 597:449–475, 2008.

[81] D. Tseluiko, M.G. Blyth, D.T. Papageorgiou, and J.-M. Vanden-Broeck. Electrified film flow over step topography at zero Reynolds number: An analytical and computational study. *J. Eng. Math.*, 69:169–183, 2011.

[82] A.A Darhuber and S.M. Troian. Principles of microfluidic actuation by modulation of surface stresses. *Annu. Rev. Fluid Mech.*, 37:425–455, 2005.

[83] A. Corbett and S. Kumar. Combined thermal and electrohydrodynamic patterning of thin liquid films. *J. Eng. Math.*, 2013.

[84] M.H. Eres, L.W. Schwartz, and R.V. Roy. Fingering phenomena for driven coating films. *Phys. Fluids*, 12:1278–1295, 2000.

[85] L.W. Schwartz and R.R. Eley. Simulation of droplet motion on low-energy and heterogeneous surfaces. *J. Colloid Interface Sci.*, 202:173–188, 1998.

[86] P.N. Brown, A.C. Hindmarsh, and L.R. Petzold. Using Krylov methods in the solution of large-scale differential-algebraic systems. *SIAM J. Sci. Comput.*, 16:1467–1488, 1994.

[87] I.B. Rietveld, K. Kobayashi, H. Yamada, and K. Matsushige. Morphology control of poly(vinylidene fluoride) thin film made with electrospray. *J. Colloid Interface Sci.*, 298:639–651, 2006.

[88] A. Rezvanpour and C.H. Wang. Computational and experimental studies of electrospray deposition process in pharmaceutical micro-pattern formation. *Chem. Eng. Sci.*, 66:3836–3849, 2011.

[89] F. Rietzler, M. Piermaier, A. Deyko, H.P. Steinruck, and F. Maier. Electrospray ionization of ultrathin ionic liquid films: $[C_8C_1Im]Cl$ and $[C_8C_1Im][Tf_2N]$ on Au(111). *Langmuir*, 30:1063–1071, 2014.

[90] C. Chen, E.M. Kelder, P.J.J.M. van der Put, and J. Schoonman. Morphology control of thin $LiCoO_2$ films fabricated using the electrostatic spray deposition (esd) technique. *J. Mater. Chem.*, 6:765771, 1996.

[91] L. Espín and S. Kumar. Forced spreading of films and droplets of colloidal suspensions. *J. Fluid Mech.*, 742:495–519, 2014.

[92] S.A. Roberts and S. Kumar. Electrohydrodynamic instabilities in thin liquid trilayer films. *Phys. Fluids*, 22:122102, 2010.

[93] A. Ramkrishnan and S. Kumar. Electrohydrodynamic deformation of thin liquid films near surfaces with topography. *Phys. Fluids*, 26:122110, 2014.

[94] C.H. Ho and Y.C. Tai. Micro-electro-mechanical-systems (MEMS) and fluid flows. *Annu. Rev. Fluid Mech.*, 30:579–612, 1998.

[95] D. Bonn, J. Eggers, J. Indekeu, J. Meunier, and E. Rolley. Wetting and spreading. *Rev. Mod. Phys.*, 81:739–805, 2009.

[96] J.B. Brzoska, F. Brochard-Wyart, and F. Rondelez. Motions of droplets on hydrophobic model surfaces induced by thermal gradients. *Langmuir*, 9:2220–2224, 1993.

[97] J.Z. Chen, S.M. Troian, A.A. Darhuber, and S. Wagner. Effect of contact angle hysteresis on thermocapillary droplet actuation. *J. Appl. Phys.*, 97:014906, 2005.

[98] D.E. Kataoka and S.M. Troian. A theoretical study of instabilities at the advancing front of thermally driven coating films. *J. Colloid Interface Sci.*, 192:350–362, 1997.

[99] G. Karapetsas, K.C. Sahu, and O.K. Matar. Effect of contact line dynamics on the thermocapillary motion of a droplet on an inclined plate. *Langmuir*, 29:8892–8906, 2013.

[100] V.S. Ajaev. Viscous flow of a volatile liquid on an inclined heated surface. *J. Colloid Interface Sci.*, 280:165–173, 2004.

[101] J. Klentzman and V.S. Ajaev. The effect of evaporation on fingering instabilities. *Phys. Fluids*, 21:122101, 2009.

[102] N. Tiwari and J.M. Davis. Stability of a volatile film spreading along a heterogeneously-heated substrate. *J. Colloid Interface Sci.*, 355:243–251, 2011.

[103] V.S. Ajaev, J. Klentzman, T. Gambaryan-Roisman, and P. Stephan. Fingering instability of partially wetting evaporating liquids. *J. Eng. Math.*, 73:31–38, 2012.

[104] J.C. Berg. An Introduction to Interfaces and Colloids. *World Scientific Publishing Co. Pte. Ltd.*, 2010.

[105] O. Schnitzer and E. Yariv. The Taylor-Melcher leaky dielectric model as a macroscale electrokinetic description. *J. Fluid Mech.*, 773:1–33, 2015.

[106] R.V. Craster and O.K. Matar. Dynamics and stability of thin liquid films. *Rev. Mod. Phys.*, 81:1131–1198, 2009.

[107] R.A. Hayes and B.J. Feenstra. Video-speed electronic paper based on electrowetting. *Nature*, 425:383–385, 2003.

[108] F. Mugele and J.-C. Baret. Electrowetting: from basics to applications. *J. Phys.: Condens. Matter*, 17:R705–R774, 2005.

[109] M. Mohammadi, H. Madadi, and J. Casals-Terré. Microfluidic point-of-care blood panel based on a novel technique: Reversible electroosmotic flow. *Biomicrofluidics*, 9:054106, 2015.

[110] J.M. Davis and S.M Troian. Influence of attractive van der waals interactions on the optimal excitations in thermocapillary-driven spreading. *Phys. Rev. E*, 67:016308, 2003.

[111] A. Corbett and S. Kumar. Combined thermal and electrohydrodynamic patterning of thin liquid films. *J. Eng. Math.*, 94:81–96, 2015.

[112] L. Kondic. Instabilities in gravity driven flow of thin fluid films. *SIAM Review*, 45:95–115, 2003.

[113] N. Tiwari, Z. Mester, and J.M. Davis. Stability and transient dynamics of thin liquid films flowing over locally heated surfaces. *Phys. Rev. E*, 76:056306, 2007.

[114] R.O. Grigoriev. Transient growth in driven contact lines. *Physica D*, 209:105–116, 2005.

Appendix A

Additional equations for chapter 2

Shown below are the nonlinear evolution equations for height and charge in a leaky dielectric film

$$\begin{aligned}\frac{\partial h}{\partial t} =& -\frac{1}{3}(1+h)^3\frac{\partial^4 h}{\partial x^4} - (1+h)^2\frac{\partial^3 h}{\partial x^3}\frac{\partial h}{\partial x} + \frac{(1+h)^3}{6(h(1-\varepsilon)+1+\beta\varepsilon)^2}\left(\frac{\partial q}{\partial x}\right)^2 A_1 \\ & - \frac{(1+h)^2}{6(h(1-\varepsilon)+1+\beta\varepsilon)^3}\frac{\partial^2 h}{\partial x^2}A_2 + \frac{(1+h)}{(h(1-\varepsilon)+1+\beta\varepsilon)^4}\left(\frac{\partial h}{\partial x}\right)^2 A_3 \\ & + \frac{(1+h)^3}{6(h(1-\varepsilon)+1+\beta\varepsilon)^2}\frac{\partial^2 q}{\partial x^2}A_4 - \frac{(1+h)^2}{6(h(1-\varepsilon)+1+\beta\varepsilon)^3}\left(\frac{\partial h}{\partial x}\right)\left(\frac{\partial q}{\partial x}\right)A_5 \\ & \frac{1}{2}(1+h)^2\mathrm{M}\frac{\partial^2\theta(z=h)}{\partial x^2} + (1+h)\mathrm{M}\frac{\partial h}{\partial x}\frac{\partial\theta(z=h)}{\partial x}, \end{aligned} \tag{A.1}$$

$$\begin{aligned}\frac{\partial q}{\partial t} =& \frac{1}{2}q(1+h)^2\frac{\partial^4 h}{\partial x^4} - \frac{1}{2}(1+h)^2\frac{\partial q}{\partial x}\frac{\partial^3 h}{\partial x^3} - q(1+h)\frac{\partial^3 h}{\partial x^3}\frac{\partial h}{\partial x} \\ & + \frac{q}{2(h(1-\varepsilon)+1+\beta\varepsilon)^4}\left(\frac{\partial h}{\partial x}\right)^2 B_1 + \frac{(1+h)^2}{2(h(1-\varepsilon)+1+\beta\varepsilon)^2}\left(\frac{\partial q}{\partial x}\right)^2 B_2 \\ & \frac{q(1+h)^2}{2(h(1-\varepsilon)+1+\beta\varepsilon)^2}\frac{\partial^2 q}{\partial x^2}B_3 - \frac{q(1+h)}{2(h(1-\varepsilon)+1+\beta\varepsilon)^3}\frac{\partial^2 h}{\partial x^2}B_4 \\ & - \frac{(1+h)}{2(h(1-\varepsilon)+1+\beta\varepsilon)^3}\frac{\partial h}{\partial x}\frac{\partial q}{\partial x}B_5 + \frac{1+q(h-\beta)}{h(1-\varepsilon)+1+\beta\varepsilon}\sigma \\ & \mathrm{M}(1+h)\left(\frac{\partial q}{\partial x}\frac{\partial\theta(z=h)}{\partial x} + q\frac{\partial^2\theta(z=h)}{\partial x^2}\right) + \mathrm{M}q\frac{\partial h}{\partial x}\frac{\partial\theta(z=h)}{\partial x}. \end{aligned} \tag{A.2}$$

The coefficients of the nonlinear evolution equations are

$$A_1 = -2 + 3\beta + h(-7 + \beta(10\varepsilon - 3)) + 5h^2(\varepsilon - 1) + 5\beta^2\varepsilon, \tag{A.3}$$

$$\begin{aligned} A_2 =& 2(1+h)(\varepsilon-1)^2\varepsilon + q(1+\beta)\varepsilon\left[-1 + h(\varepsilon-1) + (4+3\beta)\varepsilon\right] \\ &+ q^2\left[3 + 3h^2(\varepsilon-1)^2 + (2+7\beta-\beta^2)\varepsilon - 3\beta^3\varepsilon^2 - 9h^2(\varepsilon-1)(1+\beta\varepsilon)\right. \\ &\left. + h\left(9 - (1 - 16\beta + \beta^2)\varepsilon + 9\beta^2\varepsilon^2\right)\right], \end{aligned} \tag{A.4}$$

$$\begin{aligned} A_3 =& -(1+h)(1+\beta)(\varepsilon-1)^2\varepsilon^2 - q(1+\beta)^2\varepsilon^2\left[-1 + h(\varepsilon-1) + (2+\beta)\varepsilon\right] \\ &+ q^2\left[-1 + h^4(\varepsilon-1)^3 - \varepsilon - 4\beta\varepsilon - \varepsilon^2 - 4\beta\varepsilon^2 - 6\beta^2\varepsilon^2 + \beta^4\varepsilon^3\right. \\ &\left. - 4h^3(\varepsilon-1)^2(1+\beta\varepsilon) - 4h(1+\beta\varepsilon)^3 + 6(\varepsilon-1)h^2(1+\beta\varepsilon)^2\right], \end{aligned} \tag{A.5}$$

$$A_4 = -2(1+\beta)\varepsilon + q\left[-2 + 3\beta + 5h^2(\varepsilon-1) + 5\beta^2\varepsilon + h(-7 + 3\beta - 10\beta\varepsilon)\right], \tag{A.6}$$

$$\begin{aligned} A_5 =& (1+\beta)\varepsilon(1 + h + 8\varepsilon - h\varepsilon + 9\beta\varepsilon) \\ &+ q\left[15 - 6\beta + 21h^3(\varepsilon-1)^2 + 8\varepsilon + 31\beta\varepsilon - 19\beta^2\varepsilon - 21\beta^3\varepsilon^2\right. \\ &- 3h^2(\varepsilon-1)(19 + \beta(21\varepsilon - 2)) \\ &\left. + h\left(51 - 7\varepsilon + 4\beta(25\varepsilon - 3) + \beta^2\varepsilon(63\varepsilon - 19)\right)\right], \end{aligned} \tag{A.7}$$

$$\begin{aligned} B_1 =& -2q(1+\beta)^2\varepsilon^2\left[-2 - 2h(\varepsilon-1) + (3+\beta)\varepsilon\right] \\ &- (1+h)(\varepsilon-1)^2\varepsilon\left(-1 + h(\varepsilon-1) + (3+2\beta)\varepsilon\right) \\ &+ q^2\left[-2 + 2h^4(\varepsilon-1)^3 - (3 + 10\beta + \beta^2)\varepsilon - (3 + 12\beta + 17\beta^2 + 2\beta^3)\varepsilon^2 + 2\beta^4\varepsilon^3\right. \\ &- 8h^3(\varepsilon-1)^2(1+\beta\varepsilon) + h^2(\varepsilon-1)\left(12 + (1 + 26\beta + \beta^2)\varepsilon + 12\beta^2\varepsilon^2\right) \\ &\left. - 2h\left(4 + (1 + 14\beta + \beta^2)\varepsilon + \beta(1 + 14\beta + \beta^2)\varepsilon^2 + 4\beta^3\varepsilon^3\right)\right], \end{aligned} \tag{A.8}$$

$$B_2 = -(1+\beta)\varepsilon + 2q\left[-1 + 2\beta + 3h^2(\varepsilon-1) + 3\beta^2\varepsilon + h(-4 + 2\beta - 6\beta\varepsilon)\right], \tag{A.9}$$

$$B_3 = -(1+\beta)\varepsilon + q\left[-1+2\beta+3h^2(\varepsilon-1)+3\beta^2\varepsilon+h(-4+2\beta-6\beta\varepsilon)\right], \tag{A.10}$$

$$\begin{aligned} B_4 =&(1+h)(\varepsilon-1)^2\varepsilon+2q(1+\beta)^2\varepsilon^2 \\ &+q^2\left[2+2h^3(\varepsilon-1)^2+\varepsilon+4\beta\varepsilon-\beta^2\varepsilon-2\beta^3\varepsilon^2-6h^2(\varepsilon-1)(1+\beta\varepsilon)\right. \\ &\left.+h\left(6-(1-10\beta+\beta^2)\varepsilon+6\beta^2\varepsilon^2\right)\right], \end{aligned} \tag{A.11}$$

$$\begin{aligned} B_5 =&(1+h)(\varepsilon-1)^2\varepsilon+6q(1+\beta)^2\varepsilon^2 \\ &+q^2\left[10-2\beta+12h^3(\varepsilon-1)^2+5\varepsilon+20\beta\varepsilon-9\beta^2\varepsilon-12\beta^3\varepsilon^2\right. \\ &-2h^2(\varepsilon-1)(17+\beta(18\varepsilon-1)) \\ &\left.+h\left(32-5\varepsilon+9\beta^2\varepsilon(4\varepsilon-1)+\beta(58\varepsilon-4)\right)\right], \end{aligned} \tag{A.12}$$

$$\frac{\partial\theta(z=h)}{\partial x} = \frac{-\kappa(\beta+1)}{(h(\kappa-1)+\beta+\kappa)^2}\frac{\partial h}{\partial x}, \tag{A.13}$$

$$\frac{\partial^2\theta(z=h)}{\partial x^2} = -\frac{\kappa(\beta+1)}{(h(\kappa-1)+\beta+\kappa)^2}\frac{\partial^2 h}{\partial x^2}+\frac{2\kappa(\kappa-1)(1+\beta)}{(h(\kappa-1)+\beta+\kappa)^3}\left(\frac{\partial h}{\partial x}\right)^2. \tag{A.14}$$

Appendix B

Dimensionless evolution equations for chapter 3

Here we present the dimensionless evolution equations for height (3.24) and charge (3.25) in complete form.

The height evolution equation is

$$\frac{\partial h}{\partial t} = -\frac{1}{6}\frac{\partial^2 h}{\partial x^2}h^3 - \frac{1}{2}\frac{\partial c_5}{\partial x}h^2 - \frac{\partial h}{\partial x}\left[\frac{1}{2}\left(\frac{\partial p}{\partial x} - 1\right)h^2 + c_5\, h\right], \tag{B.1}$$

and the charge evolution equation is

$$\begin{aligned}\frac{\partial q}{\partial t} = & q\left[-\frac{1}{2}\frac{\partial^2 p}{\partial x^2}h^2 - \frac{\partial c_5}{\partial x}h + Co\, q\frac{\partial h}{\partial x}\left(\frac{\partial c_1}{\partial x}h + \frac{\partial h}{\partial x}c_1\right)\right] \\ & - \frac{\partial q}{\partial x}\left[\frac{1}{2}\left(\frac{\partial p}{\partial x} - 1\right)h^2 + c_5\, h\right] - \sigma\, c_1.\end{aligned} \tag{B.2}$$

Pressure is given by

$$p(x,t) = -\frac{1}{Ca}\frac{\partial^2 h}{\partial x^2} + \frac{Co}{2}\left(\varepsilon c_1^2 - c_3^2\right) - \Pi, \tag{B.3}$$

where

$$c_1(x,t) = \frac{\partial \psi_1}{\partial z}, \tag{B.4}$$

$$c_3(x,t) = \frac{\partial \psi_2}{\partial z}. \tag{B.5}$$

The potentials are

$$\psi_1(x,z,t) = 1 + \frac{1+q(h-1)}{h(\varepsilon-1)-\varepsilon}\, z, \tag{B.6}$$

$$\psi_2(x,z,t) = \frac{\varepsilon + h\, q}{h(\varepsilon-1)-\varepsilon}(z-1). \tag{B.7}$$

The coefficient c_5 comes from the tangential stress balance and is given by

$$c_5(x,t) = -(\frac{\partial p}{\partial x} - 1)h - M\frac{\partial \theta(z=h)}{\partial x} - Co\, q\frac{\partial \psi(z=h)}{\partial x}. \tag{B.8}$$

The temperature fields in each layer are

$$\theta_1(x,z,t) = 1 + \frac{\kappa}{h(1-\kappa)-1}\, z, \tag{B.9}$$

$$\theta_2(x,z,t) = \frac{z-1}{h(1-\kappa)-1}. \tag{B.10}$$